



**Diego Fernando Celis Torres**

**Numerical study of the influence of tilt valve angle  
on blood flow in an aortic model**

**Dissertação de Mestrado**

Dissertation presented to the Programa de Pós-graduação em Engenharia Mecânica of PUC-Rio in partial fulfillment of the requirements for the degree of Mestre em Engenharia Mecânica.

Advisor: Profa. Angela Ourivio Nieckele  
Co-advisor: Dr. Bruno Alvares de Azevedo Gomes

Rio de Janeiro  
August 2017



**Diego Fernando Celis Torres**

**Numerical study of the influence of tilt valve angle  
on blood flow in an aortic model**

Dissertation presented to the Programa de Pós-graduação em Engenharia Mecânica of PUC-Rio in partial fulfillment of the requirements for the degree of Mestre em Engenharia Mecânica. Approved by the undersigned Examination Committee.

**Profa. Angela Ourivio Nieckele**

Advisor

Departamento de Engenharia Mecânica – PUC-Rio

**Dr. Bruno Alvares de Azevedo Gomes**

Co-Advisor

Departamento de Engenharia Mecânica – PUC-Rio

**Prof. Luiz Felipe Pinho Moreira**

Faculdade de Medicina, Incor – USP

**Profa. Mônica Feijó Naccache**

Departamento de Engenharia Mecânica – PUC-Rio

**Prof. Márcio da Silveira Carvalho**

Vice Dean of Graduate Studies

Centro Técnico Científico – PUC-Rio

Rio de Janeiro, August 30th, 2017

All rights reserved.

## Diego Fernando Celis Torres

The author is a graduate in Mechanical Engineering from Universidad Industrial de Santander (UIS), Bucaramanga, Colombia, in 2014, and is currently a postgraduate student in the Mechanical Engineering program at PUC-Rio. He has experience in the area of computational fluid dynamics, wind energy and mechatronics systems, subjects oriented to the academic and scientific fields.

### Bibliographic data

Celis Torres, Diego Fernando

Numerical study of the influence of tilt valve angle on blood flow in an aortic model / Diego Fernando Celis Torres ; advisor: Angela Ourivio Nieckele ; co-advisor: Bruno Alvares de Azevedo Gomes. – 2017.  
115 f. : il. color. ; 30 cm

Dissertação (mestrado) – Pontifícia Universidade Católica do Rio de Janeiro, Departamento de Engenharia Mecânica, 2017.

Inclui bibliografia

1. Engenharia Mecânica – Teses. 2. Substituição de válvula aórtica por cateter. 3. Aorta. 4. Dinâmica dos fluidos computacional. 5. Hemodinâmica. I. Nieckele, Angela Ourivio. II. Gomes, Bruno Alvares de Azevedo. III. Pontifícia Universidade Católica do Rio de Janeiro. Departamento de Engenharia Mecânica. IV. Título.

CDD: 621

Para Héctor, Elsa, Laura y Oscar.

## Acknowledgements

I thank my parents, Hector and Elsa, my little sister Laura and my new brother Oscar, for their advices, support and affection.

To my aunts Rosita and Mana who have planted my way with their eternal love and great wisdom.

I am truly thankful to my advisors, Angela Nieckele and Bruno Azevedo, for the encouragement, inspiring suggestions, advices and generous support throughout the development of my MSc research.

I would like to express my gratitude to the Cardiovascular Engineering Team, for the companionship and valuable scientific discussion; I hope we continue growing and making great contributions to the field.

I also gratefully acknowledge the financial support of CAPES and CNPq.

## Abstract

Celis Torres, Diego Fernando; Nieckele, Angela Ourivio; Gomes, Bruno Alvares de Azevedo. **Numerical study of the influence of tilt valve angle on blood flow in an aortic model**. Rio de Janeiro, 2017. 115p. Dissertação de Mestrado – Departamento de Engenharia Mecânica, Pontifícia Universidade Católica do Rio de Janeiro.

Transcatheter Aortic Valve Replacement (TAVR) has become a powerful alternative for patients with aortic stenosis and a high surgical risk to face a traditional open chest surgery. The knowledge of the pressure distribution as well as shear stress at the aortic surface may help identify critical regions, where aortic remodeling process may occur. The purpose of the present work is to evaluate numerically the influence of the positioning of the prosthetic valve orifice in the flow field. The study was carried out on the basis of a particular patient who had undergone a TAVR. A 3D model was generated from computed tomography angiography and image segmentation of the aorta. Experimental data previously obtained in the same geometry indicated that the jet flow through the inlet valve is turbulent flow. The flow field was numerically determined with the commercial software Fluent. The turbulence was modeled with the two-equation  $k-\omega$  SST model. To represent a pulsatile flow, different mass flow rates were imposed at the inlet valve. Similar flow pattern was observed for all flow rates investigated. It was shown that small variations of the tilt angle can modify the nature of the flow, displacing the position of the vortices and altering the location of high shear stress, as well as high pressure, at the aortic inner wall. It was also shown that an increase of the turbulent intensity at the entrance decreases the values of shear stress and pressure on the walls. These hemodynamic features may be relevant in the aortic remodeling process and the mechanical stresses may influence the durability of the valve prosthesis.

## Keywords

Transcatheter Aortic Valve Replacement; Aorta; Computational Fluid Dynamics; Hemodynamics.

## Resumo

Celis Torres, Diego Fernando; Nieckele, Angela Ourivio; Gomes, Bruno Alvares de Azevedo. **Estudo numérico da influência da inclinação do ângulo da válvula no escoamento sanguíneo em um modelo aórtico**. Rio de Janeiro, 2017. 115p. Dissertação de Mestrado – Departamento de Engenharia Mecânica, Pontifícia Universidade Católica do Rio de Janeiro.

A substituição de válvula aórtica por cateter (Transcatheter Aortic Valve Replacement, TAVR) tornou-se uma poderosa alternativa para pacientes com estenose aórtica e com alto risco de serem submetidos à cirurgia tradicional de peito aberto. O conhecimento da distribuição da pressão, bem como a tensão cisalhante na superfície da aorta podem ajudar a identificar regiões críticas, onde o processo de remodelamento da aorta pode ocorrer. O objetivo do presente trabalho é avaliar numericamente a influência do posicionamento do orifício da válvula protética no campo de escoamento. O estudo foi realizado com base em um paciente submetido a TAVR. Um modelo 3D foi gerado a partir de angiotomografia e de segmentação de imagens da aorta. Dados experimentais obtidos anteriormente na mesma geometria indicaram que o fluxo do jato através da válvula de entrada é de natureza turbulenta. O escoamento foi determinado numericamente com o software comercial FLUENT. A turbulência foi modelada com o modelo de duas equações  $k-\omega$  SST. Para representar um fluxo pulsátil, foram impostos diferentes fluxos de massa na entrada da válvula. Para todas as vazões investigadas, obteve-se um padrão de escoamento semelhante. Mostrou-se que uma pequena variação dos ângulos de inclinação pode modificar a natureza do fluxo, deslocando a posição dos vórtices e alterando a localização das regiões de alta tensão de cisalhamento, assim como de alta pressão, na superfície interna da aorta. Mostrou-se também que um aumento da intensidade da turbulência na entrada diminui os valores de tensão cisalhante e de pressão nas paredes da aorta. Essas características hemodinâmicas podem ser relevantes no processo de remodelação aórtica e os estresses mecânicos podem influenciar na durabilidade da prótese valvular.

## Palavras-chave

Substituição de válvula aórtica por cateter; Aorta; Dinâmica dos Fluidos Computacional; Hemodinâmica.

## Table of contents

1 INTRODUCTION	19
1.1. Objectives	21
1.2. Organization of the Manuscript	21
2 BACKGROUND	23
2.1. Basic Cardiovascular Anatomy	23
2.2. Usual Aortic Valve Diseases	26
2.3. Transcatheter Aortic Valve Replacement (TAVR)	27
2.4. CFD in Hemodynamics of the Aorta and its Validation with Simplified Hydrodynamic Models	28
3 METHODOLOGY	32
3.1. 3D Modeling of the Patient's Aorta	32
3.2. Mathematic Modeling	34
3.2.1. Conservation equations	36
3.2.2. Turbulence model	38
3.2.3. Boundary conditions	41
3.3. Numerical Method	43
3.3.1. Meshing	44
4 RESULTS	46
4.1. Dimensionless Variables	48
4.2. Experimental-Data	49
4.3. Experimental-Numerical Comparison	50
4.4. Influence of Tilt Valve Angle on Blood Flow	57
4.4.1. Axial Velocity	60
4.4.2. Enstrophy	63
4.4.3. Pressure	64
4.4.4. Shear Reynolds Stress	68
4.4.5. Shear Stress at Aortic Wall - WSS	69

4.4.6. Pressure on the Aortic Wall	73
4.4.7. Profiles along the Z-axis	75
4.4.8. Conclusions	84
4.5. Influence of Turbulent Intensity on Blood Flow	85
4.5.1. Axial Velocity	85
4.5.2. Pressure	87
4.5.3. Dimensionless Shear Reynolds Stress	88
4.5.4. Wall Shear Stress - WSS	89
4.5.5. Pressure on the Aortic Wall	92
4.5.6. Profiles along the Z-axis	95
4.5.7. Conclusions	97
5 FINAL REMARKS	99
REFERENCE	102
A1. Grid Test	107
A2 Comparison of Turbulence Models	111

## List of figures

Figure 2.1 - Heart anatomy ( <a href="http://www.texasheart.org/HIC/Anatomy/anatomy2.cfm">http://www.texasheart.org/HIC/Anatomy/anatomy2.cfm</a> )	24
Figure 2.2 - The heart valves ( <a href="http://www.texasheart.org/HIC/Anatomy/valves.cfm">http://www.texasheart.org/HIC/Anatomy/valves.cfm</a> )	24
Figure 2.3 - Parts of the aorta (Jakov, 2017)	25
Figure 2.4 - (a) Regurgitation. (b) Stenosis (Harvard Health Publications)	26
Figure 2.5 - Types of TAVR procedures (Adapted from <a href="https://www.sjchs.org/media/file/TAVR-version.jpg">https://www.sjchs.org/media/file/TAVR-version.jpg</a> )	28
Figure 3.1 – 3D model of the aorta	33
Figure 3.2 - Flow rates in a cardiac cycle. Adapted from (Borazjani; Ge; Sotiropoulos, 2010)	35
Figure 3.3 – Schematic variation of a random variable	36
Figure 3.4 – System of reference	41
Figure 3.5 – Reference to define boundary conditions	41
Figure 3.6 – Mesh used in the numerical solution. (a) Complete Geometry (b) Cross-section at right coronary level.	45
Figure 4.1 – Regions of interest for the analysis. (a) For internal fields. (b) For analysis on the wall	48
Figure 4.2 – Nomenclature and position of the planes	50
Figure 4.3 – Experimental axial velocity contours. Azevedo (2017). $Q = 5.3\text{lt}/\text{min}$	51
Figure 4.4 – Numerical axial velocity contours. $Q=5.3\text{lt}/\text{min}$	51
Figure 4.5 – Experimental axial velocity contours. Azevedo (2017). $Q = 3.3\text{ lt}/\text{min}$	53
Figure 4.6 - Numerical axial velocity contours. $Q=3.3\text{lt}/\text{min}$	53
Figure 4.7 – Experimental dimensionless shear Reynolds stress. Azevedo (2017). $Q=5.3\text{lt}/\text{min}$	54
Figure 4.8 – Numerical dimensionless shear Reynolds stress. $Q=5.3\text{lt}/\text{min}$	54

Figure 4.9 – Experimental dimensionless shear Reynolds stress. Azevedo (2017). $Q=3.3\text{lt}/\text{min}$	55
Figure 4.10 – Numerical dimensionless shear Reynolds stress. $Q=3.3\text{lt}/\text{min}$	55
Figure 4.11 – Experimental x-vorticity. Azevedo (2017). $Q=5.3\text{lt}/\text{min}$	55
Figure 4.12 – Numerical x-vorticity. $Q=5.3\text{lt}/\text{min}$	56
Figure 4.13 – Experimental x-vorticity. Azevedo (2017). $Q=3.3\text{lt}/\text{min}$	57
Figure 4.14 – Numerical x-vorticity. $Q=3.3\text{lt}/\text{min}$	57
Figure 4.15 – Variation of pathlines when tilting the aortic valve angle. $Q=25\text{lt}/\text{min}$	58
Figure 4.16– Iso-surface surface of $u_z = 1.3\text{ m/s}$ , colored by dimensionless pressure. Three tilt angle ( $-4^\circ$ , $0^\circ$ and $+5^\circ$ ). $Q=25\text{lt}/\text{min}$	59
Figure 4.17 - Axial velocity fields varying the tilt angle. $Q=25\text{lt}/\text{min}$	60
Figure 4.18 – Axial velocity contours at transverse planes in geometry, for different tilt angles. $Q=25\text{lt}/\text{min}$	61
Figure 4.19 – Individual transverse planes showing the axial velocity fields, for different tilt angles. $Q=25\text{lt}/\text{min}$ .	61
Figure 4.20 – Comparison of axial velocity fields varying the tilt angle for $Q = 2.6\text{ lt}/\text{min}$ ; $15\text{ lt}/\text{min}$ and $25\text{ lt}/\text{min}$ .	62
Figure 4.21 – Comparison of dimensionless axial velocity fields varying the tilt angle for $Q = 2.6\text{ lt}/\text{min}$ ; $15\text{ lt}/\text{min}$ and $25\text{ lt}/\text{min}$	63
Figure 4.22 – Dimensionless enstrophy varying the tilt angle. $Q = 2.6\text{ lt}/\text{min}$ ; $15\text{ lt}/\text{min}$ and $25\text{ lt}/\text{min}$ .	64
Figure 4.23 – Pressure fields in the central plane varying the tilt angle. $Q=25\text{lt}/\text{min}$	64
Figure 4.24 – Dimensionless pressure contours at transverse planes in geometry, for different tilt angles. $Q=25\text{lt}/\text{min}$	65
Figure 4.25 – Dimensionless pressure at different flow rates and tilt angles: $Q = 25\text{ lt}/\text{min}$ ; $15\text{ lt}/\text{min}$ and $2.6\text{ lt}/\text{min}$	66
Figure 4.26 – Obtaining pressure lines	66
Figure 4.27 – Pressure variation along line y at $z=6\text{ cm}$ . Influence of inlet tilt angle. $Q = 25\text{ lt}/\text{min}$ ; $15\text{ lt}/\text{min}$ and $2.6\text{ lt}/\text{min}$ .	67

Figure 4.28 – Dimensionless Reynolds Stress as the inclination of the jet changes.	68
Figure 4.29 – Influence of tilt valve angle on WSS. Q=25lt/min	69
Figure 4.30 – Change in the ranges of values	70
Figure 4.31 – Sample for quantitative analysis	71
Figure 4.32 – Identification of high WSS area at the aortic wall as a function of the tilt angle. Q=25lt/min.	71
Figure 4.33 – Percentage distribution of WSS on the anterolateral wall of the ascending aorta varying with the tilt angle	72
Figure 4.34 – Percentage of high WSS values on the right anterolateral wall of the ascending aorta varying with the tilt angle	72
Figure 4.35 - Influence of tilt valve angle on the pressure on the walls. Q=25lt/min.	73
Figure 4.36 - Pressure on the anterolateral wall varying with the tilt angle Q=25lt/min	74
Figure 4.37 - Percentage distribution of the pressure on the anterolateral wall of the ascending aorta varying with the tilt angle	74
Figure 4.38 - Percentage of high pressure values on the right anterolateral wall of the ascending aorta varying with the tilt angle	75
Figure 4.39 - Schematic diagram in which the profiles are plotted along the z axis	75
Figure 4.40 – Influence of tilt angle on the axial velocity along the z-axis. Q = 25 lt/min; 15 lt/min and 2.6 lt/min.	76
Figure 4.41 – x and y-velocities along z-axis. Q = 25 lt/min; 15 lt/min and 2.6 lt/min.	78
Figure 4.42 – Dimensionless Pressure along z-axis. Q = 25 lt/min; 15 lt/min and 2.6 lt/min	79
Figure 4.43 – Turbulent intensity in the Z-axis. Q = 25 lt/min; 15 lt/min and 2.6 lt/min	81
Figure 4.44 – Dimensionless shear Reynolds stress, $\tau_{tyz}^*$ in the Z-axis. Q = 25 lt/min; 15 lt/min and 2.6 lt/min.	82
Figure 4.45 – Profile of dimensionless deviatory normal Reynolds stress along the Z-axis. Q = 25 lt/min; 15 lt/min and 2.6 lt/min.	83

Figure 4.46 - Pathlines varying with the turbulent intensity. Q=25lt/min.	86
Figure 4.47 – Influence of inlet turbulent intensity at axial velocity fields. Q=25lt/min	87
Figure 4.48 – Influence of inlet turbulent intensity at axial velocity fields. Q=5.3 lt/min	87
Figure 4.49 - Influence of inlet turbulent intensity on the pressure fields. Q=25lt/min	88
Figure 4.50 – Comparison of dimensionless pressure fields varying with turbulent intensity for two flow rates, Q=25lt/min and Q=5.3 lt/min.	88
Figure 4.51 - Influence of inlet turbulent intensity on the dimensionless shear Reynolds stress. Q=25lt/min and Q=5.3 lt/min	89
Figure 4.52 – Influence of inlet turbulence intensity at WSS. Q=25lt/min and Q=5.3lt/min	90
Figure 4.53 – Identification of high WSS area at the aortic wall as a function of inlet turbulent intensity. Q=25lt/min.	90
Figure 4.54 - Percent distribution of WSS on the anterior wall of the ascending aorta varying with the turbulent intensity	91
Figure 4.55 - Percentage of high WSS values on the anterior wall of the ascending aorta varying with the turbulent intensity	91
Figure 4.56 - Percentage of intermediate WSS values on the anterior wall of the ascending aorta varying with the turbulent intensity	92
Figure 4.57 – Modified pressure (p) on the walls varying with the turbulent intensity. Q=25lt/min and Q=5.3lt/min	93
Figure 4.58 – Pressure (p) on the walls varying with the turbulent intensity . Q=25lt/min and Q=5.3lt/min	93
Figure 4.59 – Identification of high modified pressure area at the aortic wall as a function of inlet turbulent intensity. Q=25lt/min	94
Figure 4.60 - Percent distribution of pressure on the anterior wall of the ascending aorta varying with the turbulent intensity	94
Figure 4.61 - Percentage of high modified pressure values on the anterior wall of the ascending aorta varying with the turbulent intensity	95

Figure 4.62 – Influence of the inlet turbulent intensity on the axial velocity along the z-axis. $Q=25\text{lt/min}$ and $Q=5.3\text{lt/min}$	96
Figure 4.63 – Influence of the inlet turbulent intensity on dimensionless pressure along the z-axis. $Q=25\text{lt/min}$ and $Q=5.3\text{lt/min}$	96
Figure 4.64 – Influence of the inlet turbulent intensity on turbulent intensity along the z-axis. $Q=25\text{lt/min}$ and $Q=5.3\text{lt/min}$	97
Figure 4.65 – Influence of the inlet turbulent intensity on the dimensionless shear Reynolds stress along the z-axis. $Q=25\text{ lt/min}$ and $Q=5.3\text{ lt/min}$	97
Figure A1.1 – Grid test. Axial Velocity in the z-axis. $Q = 2.6\text{ lt/min}$ and $25\text{ lt/min}$	108
Figure A1.2 – Grid test. Y-velocity in the z-axis. $Q = 2.6\text{ lt/min}$ and $25\text{ lt/min}$	108
Figure A1.3 – Grid test. Pressure in the z-axis. $Q = 2.6\text{ lt/min}$ and $25\text{ lt/min}$	109
Figure A1.4 – Grid test. Turbulent kinetic energy in the z-axis.	109
Figure A1.5 – Grid test $w'v'$ in the z-axis. $Q = 2.6\text{ lt/min}$ and $25\text{ lt/min}$	110
Figure A1.6 – Grid test. $v'v'$ in the z-axis. $Q = 2.6\text{ lt/min}$ and $25\text{ lt/min}$	110
Figure A1.7 – Grid test. $\overline{w'w'}$ in the z-axis. $Q = 2.6\text{ lt/min}$ and $25\text{ lt/min}$	110
Figure A2.1 - Comparison of turbulence models (Axial Velocity)	112
Figure A2.2 - Comparison of turbulence models (Pressure)	112
Figure A2.3 - Comparison of turbulence models (Dimensionless Reynolds Stress).	113
Figure A2.4 - Comparison of turbulence models (WSS)	114

## List of Tables

Table 4.1 – Reynolds variation	47
Table 4.2 – Outflow distribution	47
Table A1.1 – Variation $\Delta\hat{p}$ and $y^+$ (max) for three mesh sizes and two flow rates	108
Table A2.1 – Variation of $y^+$ (max) for the five turbulence models	115

## List of Symbols and Abbreviations

<i>AR</i>	Aortic Regurgitation
<i>AS</i>	Aortic Stenosis
<i>CFD</i>	Computational Fluid Dynamics
<i>CTA</i>	Computed tomography angiography
$\rho$	Density
<i>D</i>	Diameter
<i>DICOM</i>	Digital Imaging and Communication in Medicine
$\xi^2$	Dimensionless enstrophy
$\omega^+$	Dimensionless specific dissipation
$y^+$	Dimensionless wall distance
<i>DNS</i>	Direct Numerical Simulation
$y_w$	Distance to the nearest wall
$\mu$	Dynamic viscosity
<i>Q</i>	Flow rate
$u_*$	Friction velocity
$w_{in}$	Inlet Velocity
$\nu$	Kinematic viscosity
<i>LES</i>	Large Eddy Simulation
<i>LPM</i>	Liters per minute
$w_m$	Mean velocity of the fluid
$\hat{p}$	Modified pressure
<i>PIV</i>	Particle Image Velocimetry
$p$	Pressure
<i>RANS</i>	Reynolds-averaged Navier–Stokes
<i>Re</i>	Reynolds Number
<i>SST</i>	Shear Stress Transport
$\omega$	Specific turbulent dissipation rate
$S_{ij}$	Strain rate tensor
<i>TAVI</i>	Transcatheter Aortic Valve Implantation
<i>TAVR</i>	Transcatheter Aortic Valve Replacement

$\varepsilon$	Turbulence dissipation rate
$I$	Turbulence intensity
$\kappa$	Turbulent kinetic energy
$Re_t$	Turbulent Reynolds number
$\tau_{t_{ij}}^*$	Turbulent Reynolds tensor
$\mu_t$	Turbulent viscosity
$\tau_{ij}$	Viscous tensor
$\varpi$	Vorticity
$WSS$	Wall Shear Stress
$\tau_{wall}$	Wall Shear Stress

*Somewhere, something incredible is waiting to be known.*

*Carl Sagan*

*La curiosidad mató al gato una vez, las otras seis lo llevó hacia caminos  
fantásticos.*

*Ozzo Rojo*

*Não sei se a vida é curta ou longa demais para nós, mas sei que nada do  
que vivemos tem sentido, se não tocarmos o coração das pessoas.*

*Cora Coralina*

# 1 INTRODUCTION

Located between the left ventricle and the aorta we can find the aortic valve, one of the four cardiac valves. It is composed of a support ring that fixes three cusps. Its function is to allow the passage of blood from the left ventricle to the aorta in the cardiac systole and block backflow of blood during diastole, when the ventricle relaxes. With the passage of time and the effect of some diseases, this valve deteriorates, requiring, in some cases, a surgical intervention. For many years, the surgical aortic valve replacement was the standard treatment for these cases (Schwarz et al., 1982; Vaquette, 2005), reducing symptoms and improving survival in patients with low operative mortality (Baumgartner, 2005; O'brien et al., 2009; Rahimtoola, 1983, 2008). However face open heart surgery is a very high risk that some patients cannot take (Bach et al., 2009; Dewey et al., 2008) either because of his advanced age, left ventricular dysfunction, or the presence of multiple coexisting conditions (Bouma et al., 1999; Iung, 2005; Schueler et al., 2010). For this class of patients, in 2002 (Cribier, 2002) a powerful alternative less invasive was developed, called Transcatheter Aortic Valve Replacement (TAVR) (Leon et al., 2010).

In the TAVR procedure, a prosthesis is released in the region of the aortic annulus, replacing the damaged valve without removing it. It is done with the use of catheters and under the aid of fluoroscopic images and transesophageal echocardiography. With an open surgical procedure, valve placement is precise. However, more variability in the prosthesis position is expected in TAVR, due to the inherent nature of the procedure (Groves et al., 2014; Gunning et al., 2014). Further, the presence of eccentric calcifications in the aortic annulus, may avoid the full expansion of the percutaneous prosthesis, influencing in the inclination that it will acquire after its release process (Gunning; Vaughan; McNamara, 2014).

The final location of the valve can be defined as the spatial position of its effective orifice relative to the annulus, and the inclination of the effective orifice as the angle formed between the centerline of the aortic annulus and the centerline

of the effective orifice. The geometric configuration of the prosthesis is an approximate representation of the anatomy of the native valve. However, it has certain variations in its physical composition as well as in its positioning in relation to the native patient's valve, which can generate changes in the initial hemodynamic conditions in the aortic root, such as the turbulent intensity, flow direction and/or pressure drop increase. When these changes occur in the geometry (position and inclination of the aortic valve), it is possible to hypothesize that blood flow patterns may vary significantly and it can generate changes in the different hemodynamic properties of the aorta (Trauzeddel et al., 2016).

Frequently, changes in blood flow in the ascending aorta segment are related to the aortic remodeling associated with various pathological conditions, such as bicuspid aortic valve, aortic stenosis, dilatation, aneurysmal formations and tortuosity (Faggiano et al., 2013; Ha et al., 2016). However, currently, little is known about the consequences of tilting the effective orifice and the variations of the conditions of turbulent intensity at the inlet of blood flow when a prosthesis of this type is introduced into a patient.

The helical patterns of blood flow, before and after a patient undergoes the surgical procedure known as TAVR, vary considerably by the effect of the geometry of the prosthesis implemented, its inclination and its final positioning. These variations have not been completely understood and it is of great interest to analyze the influence that this type of prosthesis can have on the aortic remodeling process in order to improve its design and its assembly

Computational Fluid Dynamics (CFD) has gained a lot of interest as a complementary tool for improving understanding of pathogenesis and disease progression in cardiovascular disease (Sun; Chaichana, 2016).

Identification of regions where the wall shear stress has large values is very important because this is associated with aneurysmal dilatation of the ascending aorta (Bürk et al., 2012). It is also known that regions with pronounced curvatures have large recirculations that can generate clots in the blood circulation. In addition, the shear stress can influence the durability of the prosthesis.

Recently, the Cardiovascular Engineering Team has begun to develop a detail study of the aortic flow due to TAVR. Azevedo (2017) develop an study of a specific patient, seeking more personalized conclusions. With a better hydrodynamic knowledge of complex cases, and by measuring different parameters

that are useful and complementary for the medical area, it is possible to determine the best use of TAVR. This line of study of particular patients can contribute in the impact of the quality of life and life expectancy of patients. Following the postoperative progress, and with a fully understanding of the impacts of the positioning of the TAVR, would make it viable for a larger population of patients.

### **1.1. Objectives**

Study of the influence and variability of the effective orifice tilt angle in the blood hemodynamics in the regions of the aortic root and in the ascending aorta portion, i.e., determination on how the tilt angles, the inlet velocity and the turbulent intensity affect the blood flow patterns and hemodynamics.

To perform the study a three-dimensional aortic model was obtained from a patient submitted to TAVR. Hemodynamic flow was characterized and numerically analyzed. Validation of the formulation was carried on through comparison with experimental results obtained by the same research group (Azevedo, 2017).

More specifically, the objectives are:

- Simulate a simplified section of the aorta of a patient submitted to a transcatheter aortic valve implantation to identify recirculation regions and determinate the shear and pressure distribution at the aortic wall
- Compare the numerical simulation results with experimental data of the flow in aortic 3D model of a patient submitted to a transcatheter aortic valve implantation.
- Study the effect of small variation of tilt angles of the inlet flow.
- Analyze the effect of modifying the turbulent intensity at the inlet flow.
- Evaluate the influence of the Reynolds number on the flow.

### **1.2. Organization of the Manuscript**

This text was divided in five chapters. In the next chapter, it is presented a literature review regarding the areas of study, medical and engineering, required for the development of the research.

In Chapter 3, were described the hypotheses, the governing equations, the constitutive models of the problem and the numerical method used.

The Chapter 4 presents the results obtained for different variations of angle and inlet turbulent intensity, considering different flow rates.

Chapter 5 presents general conclusions and suggestions for future works.

## 2 BACKGROUND

The present work is multidisciplinary project, combining the areas of computational fluid mechanics and the medical area. Therefore, in the present chapter, basic cardiovascular anatomy is presented, followed by a discussion of aortic valve diseases, to finally discuss the application of Computational Fluid Dynamics (CFD) to determine the flow field through the aorta.

### 2.1. Basic Cardiovascular Anatomy

The function of the heart is to pump blood to all corners of the body. The blood collects oxygen as it passes through the lungs and circulates to the heart where it is driven to all parts of the body. After his trip through the organism, the blood is left with low oxygen concentration and is sent back to the heart so that it pumps to the lungs in order to collect more oxygen, completing the cycle.

To push the blood through the vessels of the whole body, the heart contracts and relaxes rhythmically. The contraction phase is called systole, which corresponds to the expulsion of blood out of the cavity. This systolic phase is followed by a phase of muscle relaxation called diastole, in which two stages can be distinguished: one of relaxation and another of suction to drag the blood to the interior.

As shown in Figure 2.1, the heart contains four chambers: the right and left atrium, right and left ventricle. The atria are smaller than the ventricles and have thinner, less muscular walls than the ventricles. The atria act as receiving chambers for blood, so they are connected to the veins that carry blood to the heart. The ventricles are larger, stronger pumping chambers that send blood out of the heart. The ventricles are connected to the arteries that carry blood away from the heart. (Standring; Gray, 2009)

The four valves than regulate the blood flow through the heart are shown in Figure 2.2. The tricuspid valve regulates blood flow between the right atrium and

right ventricle. The pulmonary valve controls blood flow from the right ventricle into the pulmonary arteries, which carry blood to the lungs to pick up oxygen. The mitral valve lets oxygen-rich blood from the lungs pass from the left atrium into the left ventricle. The last one is the aortic valve, and it is the focus of the present work. When this valve is not functioning in a satisfactory way, it can be replaced. The function of this valve is to allow the oxygen-rich blood to pass from the left ventricle into the aorta (Betts et al., 2016).

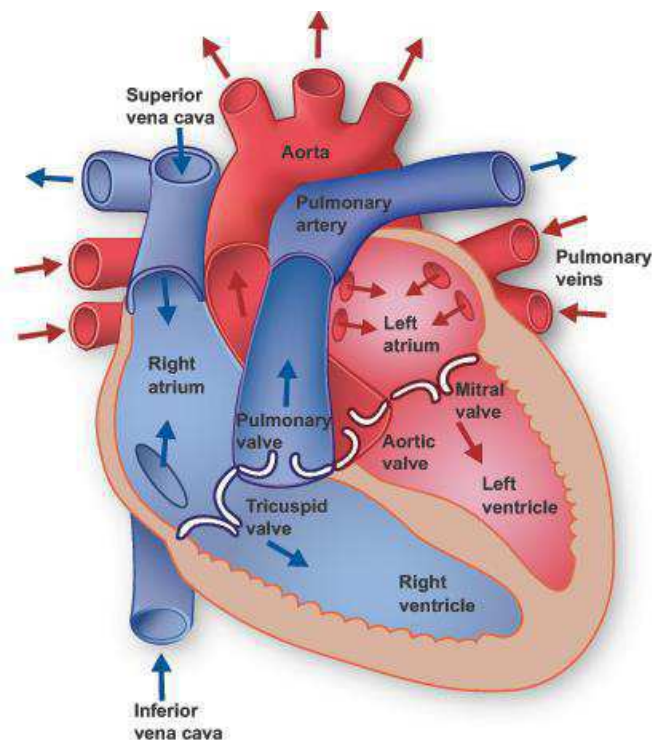


**Figure 2.1** - Heart anatomy (<http://www.texasheart.org/HIC/Anatomy/anatomy2.cfm>)

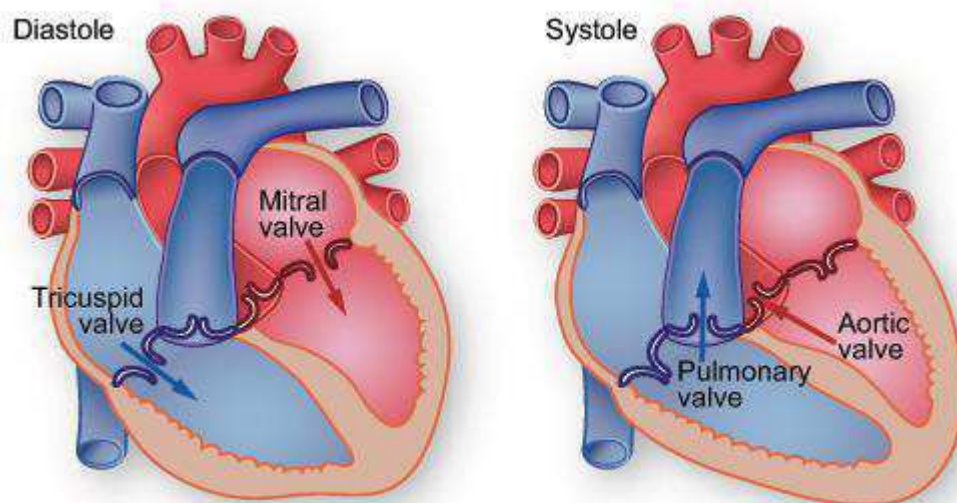


**Figure 2.2** - The heart valves (<http://www.texasheart.org/HIC/Anatomy/valves.cfm>)

The aorta, shown in Figure 2.3, is the largest artery in the body. It arises from the left ventricle, forms an arch, and then extends down to the abdomen where it branches off into two smaller arteries. Several arteries extend from the aorta to deliver blood to the various regions of the body. The aorta carries and distributes oxygen rich blood to all arteries. Most major arteries branch off from the aorta, with the exception of the main pulmonary artery. The aorta can present several geometric variations among different individuals. Even for the same individual, the aorta geometry can vary with the passage of time and due to appearance of diseases.

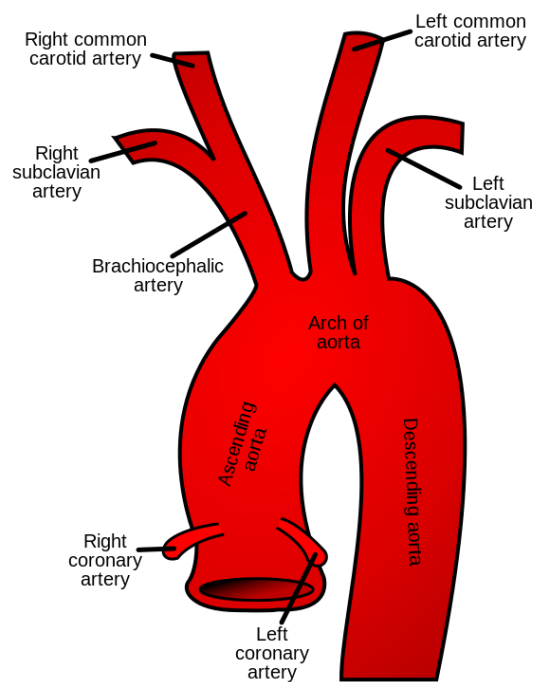


**Figure 2.3** - Parts of the aorta (Jakov, 2017)

The principal branches of the aorta shown in Fig.2.3 are:

- **Ascending Aorta:** initial part of the aorta that begins from the aortic valve and extends from the left ventricle to the aortic arch.
- **Coronary Arteries:** arteries branching from the ascending aorta to supply oxygenated blood to the myocardium. The two main coronary arteries are the right and left coronary arteries.
- **Aortic Arch:** curved section at the top of the aorta that bends backward connecting the ascending and descending portions of the aorta. Several arteries branch off from this arch to supply blood to the upper regions of the body.
- **Descending Aorta:** major portion of the aorta that extends from the aortic arch to the trunk of the body. It forms the thoracic aorta and abdominal aorta.

## 2.2. Usual Aortic Valve Diseases

The main diseases of the aortic valve in which it is necessary to perform an aortic valve replacement are regurgitation and stenosis.

Aortic regurgitation (AR) (Figure 2.4a) is also called aortic insufficiency or aortic incompetence. In this case, blood flows backward from a widened or weakened aortic valve into the left ventricle (Nishimura et al., 2017). The most serious form of aortic regurgitation is caused by an infection that leaves holes in the valve leaflets. Symptoms of aortic regurgitation may not appear for years. When symptoms do appear, it is because the left ventricle must work harder to make up for the backflow of blood. The ventricle eventually gets larger, causing a backup of fluid. Aortic regurgitation is most common in men between the ages of 30 and 60 (Bonow et al., 2006).

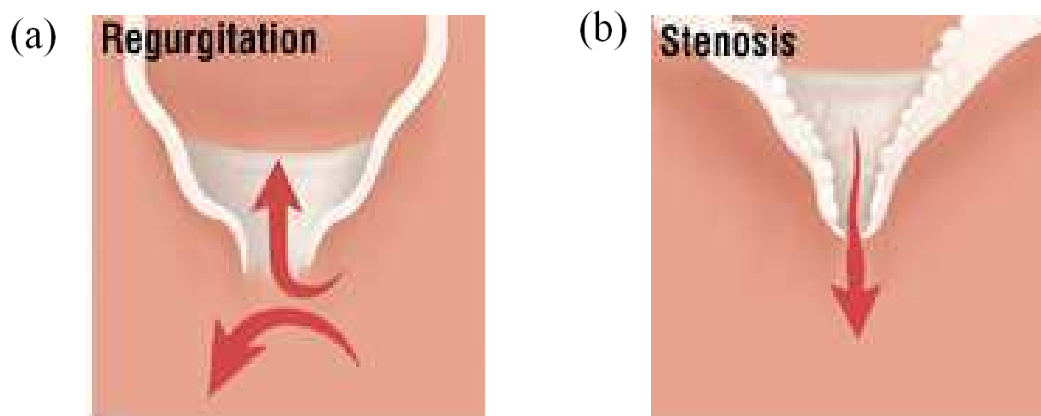


**Figure 2.4** - (a) Regurgitation. (b) Stenosis (Harvard Health Publications)

Aortic stenosis (AS) (Figure 2.4b) is the narrowing of the aortic valve. The aortic valve normally opens with each contraction of the heart to allow blood to pass from the heart to the aorta and rest of the body. Narrowing of this valve obstructs blood flow from the heart and to compensate, the heart needs to work harder in order to pump enough blood to the body. If left untreated, progression of this condition may weaken the heart over time and result in a number of life-threatening complications, including heart failure, abnormal heart rhythms and cardiac arrest. Appropriate treatment and monitoring is essential to prevent these complications from occurring and to ensure a good quality of life for those affected (Harris; Croce; Phan, 2015). Congenital defects and rheumatic fever are the main

causes of aortic stenosis in people under 50.

In some cases, people are born with a bicuspid aortic valve, meaning the valve has two leaflets instead of three. This may also cause aortic stenosis.

In elderly patients, calcium deposits and the growth of fibrous tissue on the aortic valve can stiffen (sclerosis) and distort the leaflets or cause them to fuse together. This is called calcification, and it can make the different leaflets almost look like a single one (Carabello; Paulus, 2009).

### **2.3.**

#### **Transcatheter Aortic Valve Replacement (TAVR)**

Transcatheter Aortic Valve Replacement (TAVR) or Transcatheter Aortic Valve Implantation (TAVI) is a procedure developed in 2002 (Cribier, 2002), which provides patients with a lower risk alternative than traditional open-chest valve replacements. A TAVR procedure provides beneficial treatment options to people who needed a valve implant, but could not go through an open-chest surgery. Further, it also provides in most cases, the additional bonus of a faster recovery. A patient's experience with a TAVR procedure may be comparable to an aortic balloon valvuloplasty in terms of down time and recovery, and will likely require a shorter hospital stay (average 3.5 days).

This minimally invasive procedure repairs the valve without removing the old, damaged valve. Instead, it wedges a replacement valve into the aortic annulus (Forsberg et al., 2012). This procedure has expanded the treatment to patients with symptomatic severe AS, who presented high risk to surgery. The TAVR procedure is performed using one of two main approaches shown in Figure 2.5, depending on the patient's peripheral vessel status and the center's choice of aortic valve bioprosthesis. The heart team can choose which one provides the best and safest way to access the valve (Webb; Cribier, 2011). With the first approach, the valve enters through the femoral artery. It is called the transfemoral approach, which does not require a surgical incision in the chest. The second option, known as the transapical approach, is performed using a minimally invasive surgical approach with a small incision in the chest. The valve enters through a large artery in the chest or through the tip of the left ventricle (the apex). Prostheses usually consist of three leaflets of animal pericardium coupled to a self-expanding metal frame.

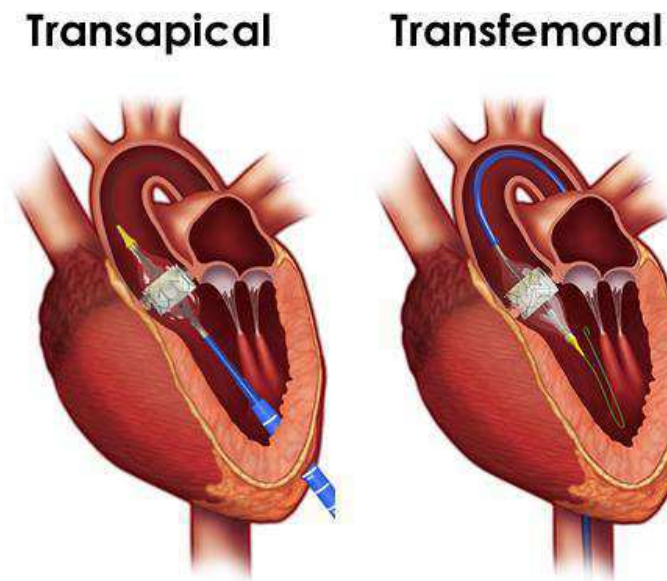


**Figure 2.5** - Types of TAVR procedures

(Adapted from <https://www.sjchs.org/media/file/TAVR-version.jpg>)

#### **2.4. CFD in Hemodynamics of the Aorta and its Validation with Simplified Hydrodynamic Models**

The application of fluid mechanics knowledge to help understand the blood flow in different parts of a human organism is not new. For example, Yoganathan et al. (1988) and Liu; Winoto; Shah, (1997) studied and pointed out the relevance of bounded jet or confined jet in biofluid mechanic applications, such as in stenotic aortic and pulmonary valve lesions, as well as atherosclerotic lesions.

In recent years, there has been several works employing CFD techniques to predict the behavior of circulatory blood flow in the human. The work developed by Malvindi et al. (2016) analyzed the aortic dissection in the ascending portion. The atherosclerosis analysis by Cecchi et al. (2011) that deepens in the role of hemodynamic shear stress in cardiovascular disease. These studies exemplified the potential role of CFD for individual risk analysis and tailored surgical planning.

In a particular case, Benim et al., (2011) analyzed by CFD the Blood flow in a human aortic arch and its major branches, for physiologic and extracorporeal circulation. For the physiologic circulation under the assumption of negligible wall distensibility, it has been observed that the time-averaged results of the pulsatile computation do not remarkably differ from those of a steady-state one.

Sun and Xu (2014) used CFD simulation based on 3D luminal reconstructions

to analyze the local flow fields and flow profiling due to changes of coronary artery geometry, thus, identifying risk factors for development and progression of coronary artery disease. This paper aims to provide an overview of the CFD applications in coronary artery disease, including biomechanics of atherosclerotic plaques, plaque progression and rupture.

In a study related to the present work, Ha et al. (2016) hypothesized that the direction and angle of aortic inflow can influence helical flow patterns and related hemodynamic features in the thoracic aorta. It was investigated the hemodynamic features in the thoracic aorta and various aortic inflow angles using patient-specific vascular phantoms that were generated using a 3D printer and time-resolved, 3D, phase-contrast magnetic resonance imaging (PC-MRI). The results showed that the rotational direction and strength of helical blood flow in the thoracic aorta largely vary according to the inflow direction of the aorta, and a higher helical velocity results in higher wall shear stress distributions. In addition, right-handed rotational flow conditions with higher rotational velocities imply a larger total kinetic energy than left-handed rotational flow conditions with lower rotational velocities.

In the type of specific analysis it was used the geometry of the aorta, which is quite irregular and complex. The flow of blood travels from the aortic root (where the aortic valve is located) to the ascending aorta, passing through the aortic arch and reaching the initial region of the descending aorta. Different types of flow configurations can be found along the blood trajectory inside the aorta. For example, the flow enters the aorta in the form of a free jet, then it flows along a kind of U-shaped tube, and it can become fully developed (i.e., without axial variations). The knowledge of how the flow evolves in these simplified situations can help understand the more complex real flow configuration.

Several studies of circular jets can be found in the literature, and the work of Rajaratnam (1976) should be mentioned, since he develop a mathematical model to study a circular jet inside a circular ducts, similar to the entrance flow in the aorta. He compared his results with experimental observations made by Hembold et al. (1954), Mikhail (1960), Becker et al. (1962), Dealy (1964), Curtet and Ricou (1964), Barchilon and Curtet (1964), Exley and Brighton (1970), Razinsky and Brighton (1971), and others. Several CFD models have been validated by comparison with this solution. Lee and Dimenna (1995) studied the ability of two CFD codes including FLUENT, to calculate the significant physical characteristics

of an axisymmetric free turbulent jet. This analysis was made comparing data and classical jet theory. The CFD codes performed well and were considered acceptable for various applications. Among some of its most interesting conclusions is that axial velocity profiles along a direction perpendicular to the jet axis are similar within the fully turbulent region; and total momentum flux of the fluid in the jet is approximately constant perpendicular to the jet axis under isothermal flow conditions.

In another work (Garcia, 2007), a FLUENT model was used for the prediction of flow fields associated with high speed jets and the impingement of under expanded jets on deflectors. Accuracy of the computational model was assessed through comparison with available experimental data. For each case, there were two main sources of error. These included the extraction of values from graphs provided in published reports and the extrapolation of values in regions where no experimental values were available. Agreement to experimental data was found to range within  $\pm 5\%$  for most regions of the flow field. However, in regions where extrapolation of the data was necessary, large discrepancies were observed with errors ranging from  $\pm 10\%$ . According to Garcia (2007), the computational results obtained in his investigation are suitable for guidance in the prediction of free jet flows, impinging flows, and other related devices. The character of the predictions seems to represent believable flow structures in fluid mechanics and fluid dynamics.

Also, Kandakure et al. (2008), studied the jet expansion and hydrodynamics in presence of confinement. In that work, the effect of enclosure size was investigated over a wide range and compared with the previous literature. It was observed that with an increase in the draft tube diameter, the entrainment rate of the surrounding fluid into the draft tube increases while the average turbulent kinetic energy in the jet flow in draft tube decreases. Thus the size of the draft tube plays an important role in determining the level of entrainment and the extent of mixing between the jet fluid and the surrounding fluid. Although with a different approach, in that research it was tested the turbulence model  $k-\omega$  standard, a model similar to the one used in the present work, proving to be a reliable model of turbulence for solving confined jets problems and to make comparisons with results previously obtained in the literature.

Another related flow that can help understand the flow through an aorta is the

internal flow in a curved tube. This has been studied experimentally by Rowe (1970), Lyne (1970), Greenspan (1973), Chandran and Yearwood (1981), Enayet et al. (1982), and others. In simplified conditions, the results show that the fluid flow in a curved tube with large curvature ratio seems to be unlike that in a curved tube with small curvature ratio. Large curvature ratio makes the internal flow more complicated; thus, the flow patterns, the separation region, and the oscillatory flow are different. The curvature ratio has a great impact on pressure distribution, especially the pressure at the tube inner side. Centrifugal force not only affects the pressure distribution in the curved section of tube, but also has an impact on the pressure distribution in the upstream and downstream tubes. Therefore, the pressure gradient has small fluctuations near the bend inlet and outlet. For the curved tube, the boundary layer separation zone is expanded by large curvature ratio, which makes the internal flow even more disordered. Wang et al, (2015) studied the same problem numerically, showing good agreement with available experimental results, attaining similar conclusions.

### **3 METHODOLOGY**

This chapter discusses all the methods used to characterize the blood flow that travels through the aorta. As already mentioned, the present study was realized considering the aorta of a particular patient. So, to obtain the flow field through the aorta, the methodology employed is subdivided into three steps, which are detailed in the subsequent sections. First, it is exposed the method used to obtain the three-dimensional geometry model used in this research. Then, it is presented the conservation equations that govern the flow. Finally, the numerical methods used for solving these equations is described.

#### **3.1. 3D Modeling of the Patient's Aorta**

This is a descriptive study of a blood flow simulation in a three-dimensional aortic model. The vascular model was constructed from a pre-TAVR aortic computed tomography angiography (CTA) planning scan from a patient. This study is registered with the National Council of Ethics in Research (Ministry of Health), and was approved by the Research Ethics Committee. The free, prior and informed consent was obtained with the patient, who was a 77-year-old male, presenting a mild systolic left ventricular dysfunction, and severe degenerative aortic stenosis with New York Heart Association functional class III by the time of study entry. The surgical mortality was 8%, estimated by EuroSCORE II. Percutaneous retrograde implant was used, via femoral access, using the Edwards SAPIEN #23 prosthesis (Edwards Lifesciences, USA). The percutaneous procedure occurred without interferences. Patient is discharged with a mean ventricular-aortic gradient of 16 mmHg and a maximum of 20 mmHg, minimal periprosthetic regurgitation, making use of clopidogrel, acetylsalicylic acid, furosemide, amlodipine, bisoprolol and warfarin.

The CTA was performed on a 64-slice scanner Somatom Sensation 64 (Siemens, Germany). A series of CTA slices were selected, covering from the aortic

annulus to the thoracic aorta. The DICOM images were transferred to the software Mimics (Materialise, Belgium) and FIJI, in order to allow the segmentation of the desired aortic region for posterior mesh generation. The result of this procedure is a three-dimensional model as shown in Figure (3.1), where it can be seen the entire ascending aorta (left); the aortic arch (above) with the start of the brachiocephalic, left common carotid and left subclavian arteries; and finally a portion of descending aorta (right).

The wall of all arteries, including the aorta, is formed by three layers. The outer layer is called adventitia is responsible for providing support and structure to the aorta. The middle layer (media) is formed by muscle and elastic fibers, allowing the aorta to expand and contract with the heartbeat. Finally, the innermost layer, called intima, corresponds to the surface along which the blood flows.

The domain of interest in the present analysis (Figure 3.1) is formed by the surface of the aorta, which is considered solid, i.e, where there is no flow through it. The blood enters the aorta through the aortic valve (left side). Part of the blood leaves the aorta through the three arteries at the upper part and the main flow leaves the aorta through the right side. The outer boundary of the computational domain is the inner layer intima of the aorta, which will be referred here simply as aortic wall.



**Figure 3.1** – 3D model of the aorta

### 3.2. Mathematic Modeling

To solve the flow field through an aorta, a series of hypotheses was defined to simplify and facilitate obtaining the solution. To validate the model, comparison was performed with experimental results obtained by Azevedo (2017). Therefore, similar hypothesis were applied as the ones considered in the experimental setup.

A single cycle of cardiac activity (Figure 3.2) can be divided into two basic phases: diastole and systole. Diastolic pressure occurs near the beginning of the cardiac cycle. It is the minimum pressure in the arteries when the pumping chambers of the heart (ventricles) fill with blood. Near the end of the cardiac cycle, systolic pressure, or peak pressure, occurs when the ventricles contract. As the heart beats, it pumps blood through a system of blood vessels, which carry blood to every part of the body. Blood pressure is the force that blood exerts on the walls of blood vessels. All or any of the events related to the flow or blood pressure that occurs from the beginning of one heartbeat to the beginning of the next is called a cardiac cycle. It can be seen in Figure 3.2 that during the systole, the flow rate increase, reaching a maximum value, and then a significant drop can be observed, after which, the flow (during diastole) is approximately constant.

The focus of the present work is to determine the flow field in the ventricular systole. During this period, the aortic walls are distended, providing their maximum diameter, with small variation due the vascular complacency. Thus, as a first simplification, the aorta's surface was considered rigid. Although this is not a completely correct hypothesis, considering these as rigid, more conservative results are obtained, because the elasticity of the walls reduces the total efforts that fall on it. Further, the aortic valve, placed at the inlet region, was approximated by an orifice with diameter  $D$  equal to 1.4 cm ( $\approx 1,5 \text{ cm}^2$ ), centered in the aortic annulus.

The cardiac cycle is naturally transient (Figure 3.2), however, in order to reduce considerably the calculation time and for a better interpretation of the results, the flow was modeled as a succession of steady states, each corresponding to a different time instants of the pulsatile cycle. The flow rate  $Q$  range considered varied from 0.8 to 25 lt/min, taking fixed values where the flow is continuous.

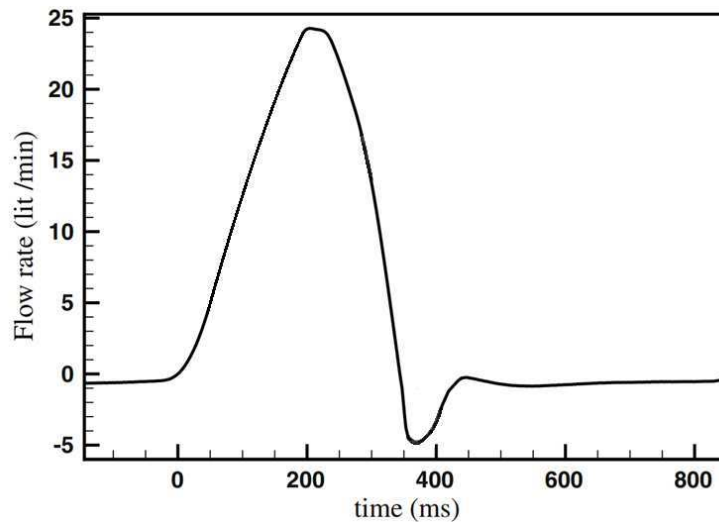


**Figure 3.2** - Flow rates in a cardiac cycle. Adapted from (Borazjani; Ge; Sotiropoulos, 2010)

Another simplification was to neglect gravity effects, since the pressure variations are dominant over the force of gravity

According to Sun and Chaichana (2016), the blood can be considered as a Newtonian fluid, i.e., the viscous stress being directly proportional to the rate of deformation of the fluid element. Further, under normal conditions at 37°C, the blood is quite similar to water and can be considered as an incompressible fluid (Feijó, 2007; Feijoo; Zouain, 1988).

Depending of the ratio of inertia to viscous force, the flow can be considered as laminar or turbulent. The Reynolds number  $Re$  is a measurement of this ratio.

$$Re = \frac{\rho w_m D}{\mu} = \frac{4 \rho Q}{\pi D \mu} \quad (3.1)$$

By the range of velocities of pulsatile cycle, the Reynolds number is not very high. However, the flow at the entrance of the aorta, flowing through the valve orifice, behaves like a free jet, and must be considered turbulent.

To model a turbulent flow, there are several possible turbulence approaches, with different level of accuracy and computational effort: Direct Numerical Simulation (DNS), Large Eddy Simulation (LES) and Reynolds Average Navier-Stoke (RANS) models (Pope, 2000). DNS does not require a model, since all turbulence scales are directly solved, but the computational effort is too high because the mesh size must be proportional to Kolmogorov scale, requiring an extremely fine mesh and time step. Therefore, in the present days, it is usually only

applied to very simple geometries and relatively low Reynolds number. LES simulation also requires a very fine mesh and small time step, although the requirements are not as strict as for DNS, because, scales smaller than the mesh size are modeled. RANS approach is a good tradeoff between accuracy and computing effort. In this method, all scales are modeled, and a wide varied of models can be found, varying from one-equation models to n-equation models. Therefore, it must be validated with experimental data for each type of application.

The RANS approach it developed considering the any generic variable  $\phi$  (like pressure or velocity) varies in a random form around a mean value  $\bar{\phi}$ , as shown in Figure 3.3, and described by Eq. (3.1). In this approach, it is considered sufficient to know the time average behavior of any variable.

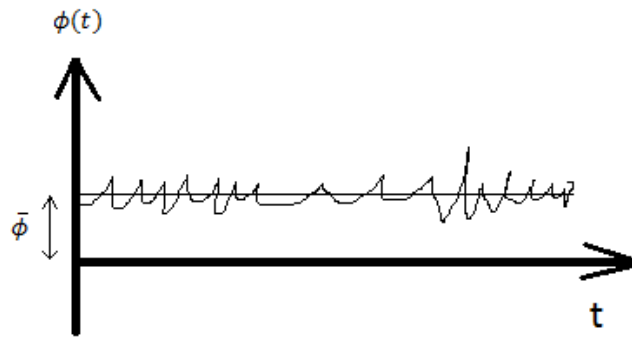


**Figure 3.3** – Schematic variation of a random variable

$$\phi = \bar{\phi} + \phi' \quad ; \quad \bar{\phi} = \frac{1}{\Delta t} \int_{\Delta t} \phi dt \quad (3.2)$$

Most turbulent models employed in hemodynamics are based on Boussinesq approximation, like  $\kappa - \varepsilon$ ,  $\kappa - \omega$  and variants of these (Kagadis et al., 2008; Wan ab Naim et al., 2014; Zhang; Gao; Chang, 2016). The turbulence model selected for this work was the  $\kappa - \omega$  SST (Menter, 1993, 1994). This model is recommend for low Reynolds number situations, and it was selected after performing several tests and comparing against experimental data of Azevedo (2017).

### 3.2.1. Conservation equations

To solve the problem we start with two basic principles of fluid mechanics, conservation of mass and conservation of momentum. To simplify the presentation the bar indicating average values of relevant variables, has been dropped.

Using the previously presented incompressibility hypothesis, the conservation of mass equation, also called continuity equation can be written in indicial notation as (Pope, 2000)

$$\frac{\partial u_i}{\partial x_i} = 0 \quad (3.3)$$

where  $(x_i)$  represents each of the coordinate axes and  $(u_i)$  the components of the velocity vector.

Adding the steady state approximation, and neglecting gravity force, the time-average Navier Stokes equation, or momentum conservation equation, (Pope, 2000) is given by:

$$\frac{\partial \rho u_j u_i}{\partial x_j} = -\frac{\partial p}{\partial x_i} + \frac{\partial \tau_{ij}}{\partial x_j} - \frac{\partial \rho \overline{u'_j u'_i}}{\partial x_j} \quad (3.4)$$

being  $\rho$  is the density,  $p$  is the pressure,  $\tau_{ij}$  is the viscous stress tensor, and  $-\rho \overline{u'_j u'_i}$  is the Reynolds stress tensor.

The viscous tensor is always symmetric and for an incompressible Newtonian fluid is given by:

$$\tau_{ij} = \mu 2 S_{ij} \quad (3.5)$$

where  $\mu$  is the molecular viscosity, and  $S_{ij}$  is the strain rate tensor:

$$S_{ij} = \frac{1}{2} \left[ \frac{\partial u_i}{\partial x_j} + \frac{\partial u_j}{\partial x_i} \right] \quad (3.6)$$

According to the Boussinesq approximation, the Reynolds stress tensor is modeled applying an analogy to the viscous tension, in which the proportionality coefficient is replaced by the turbulent viscosity  $\mu_t$ , which depends on the flow.

$$-\rho \overline{u'_j u'_i} = \mu_t 2 S_{ij} - \frac{2}{3} \rho \kappa \delta_{ij} \quad (3.7)$$

By substituting the above definitions the resulting momentum equation becomes

$$\frac{\partial \rho u_j u_i}{\partial x_j} = -\frac{\partial \hat{p}}{\partial x_i} + \frac{\partial}{\partial x_j} \left[ (\mu + \mu_t) \left( \frac{\partial u_i}{\partial x_j} + \frac{\partial u_j}{\partial x_i} \right) \right] \quad (3.8)$$

where  $\hat{p}$  is a modified pressure, which include the turbulent dynamic pressure

$$\hat{p} = p + \frac{2}{3} \rho \kappa \quad (3.9)$$

### 3.2.2. Turbulence model

The turbulent model select here was the  $\kappa - \omega$  SST turbulent model, where the turbulent viscosity is determined as a function of turbulent kinetic energy  $\kappa$  and its specific rate of dissipation  $\omega$ . Thus, the  $\kappa - \omega$  SST turbulence model (Menter, 1993) is a two-equation eddy-viscosity model. This model has become very popular, because it combines two of the best approaches in turbulence models. The use of a  $\kappa - \omega$  formulation in the inner parts of the boundary layer makes the model directly usable all the way down to the wall through the viscous sub-layer, hence the  $\kappa - \omega$  SST model can be used as a Low-Re turbulence model without any extra damping functions. The SST formulation also switches to a  $\kappa - \varepsilon$  behavior in regions far from the wall or free-stream and thereby avoids the common  $\kappa - \omega$  problem, which is its sensitivity to the inlet free-stream turbulence properties. Authors who use the  $\kappa - \omega$  SST model often merit it for its good behavior in adverse pressure gradients and separating flow (El-Samanoudy; El-Baz, 2016; Hellsten, 1998). The definition of the model, presented below is the version provided by the manual of ANSYS Fluent 17.0.

The  $\kappa - \omega$  SST turbulent eddy viscosity is computed from:

$$\mu_t = \frac{\rho \kappa}{\omega} \xi \quad (3.10)$$

where  $\xi$  is a blending factor between  $\kappa - \varepsilon$  and  $\kappa - \omega$

$$\xi = \frac{1}{\max(1/\alpha^*, S F_2 / (a_1 \omega))} \quad (3.11)$$

Here,  $S$  is the magnitude of the strain rate

$$S = \sqrt{2 S_{ij} S_{ij}} \quad (3.12)$$

and  $\alpha^*$  and  $F_2$  are

$$\alpha^* = \alpha_\infty^* \left( \frac{\alpha_o^* + Re_t/Re_\kappa}{1 + Re_t/Re_\kappa} \right) \quad (3.13)$$

$$F_2 = \tanh(\Phi_2^2) \quad ; \quad \Phi_2 = \max \left[ 2 \frac{\sqrt{\kappa}}{0.09 \omega y}, \frac{500 \mu}{\rho y^2 \omega} \right] \quad (3.14)$$

where  $y$  is the distance from the wall, and the turbulent Reynolds number  $Re_t$  is

$$Re_t = \frac{\rho \kappa}{\mu \omega} \quad (3.15)$$

The empirical constants in the above equations are:  $a_1=0.31$ ;  $\alpha_\infty^*=1$ ;  $\alpha_o^*=\beta_i/3$ ;  $Re_\kappa=6$ , and

$$\beta_i = F_1 \beta_{i,1} + (1 - F_1) \beta_{i,2} \quad (3.16)$$

$$F_1 = \tanh(\Phi_1^4) \quad ; \quad \Phi_1 = \min \left\{ \max \left[ \frac{\sqrt{\kappa}}{0.09 \omega y}, \frac{500 \mu}{\rho y^2 \omega}, \frac{4 \rho \kappa}{\sigma_{\omega,2} D_\omega^+ y^2} \right] \right\} \quad (3.17)$$

$$D_\omega^+ = \max \left[ \frac{2 \rho}{\omega \sigma_{\omega,2}} \frac{\partial \kappa}{\partial x_j} \frac{\partial \omega}{\partial x_j}, 10^{-10} \right] \quad (3.18)$$

with  $\beta_{i,1}=0.075$  and  $\beta_{i,2}=0.0828$ ;  $\sigma_{\omega,2}=1.168$ .

To obtain  $\kappa$  and  $\omega$ , their conservation equations need to be solved (Wilcox, 1993, Menter, 1994):

$$\frac{\partial(\rho u_j \kappa)}{\partial x_j} = \tilde{P}_\kappa - \rho \beta_i^* \omega \kappa + \frac{\partial}{\partial x_j} \left[ \left( \mu + \frac{\mu_t}{\sigma_\kappa} \right) \frac{\partial \kappa}{\partial x_j} \right] \quad (3.19)$$

$$\begin{aligned} \frac{\partial(\rho u_j \omega)}{\partial x_j} = & \frac{\rho \alpha}{\mu_t} P_\kappa - \beta_i \rho \omega^2 + \frac{\partial}{\partial x_j} \left[ \left( \mu + \frac{\mu_t}{\sigma_\omega} \right) \frac{\partial \omega}{\partial x_j} \right] \\ & + 2(1 - F_1) \frac{\rho \sigma_{\omega,2}}{\omega} \frac{\partial \kappa}{\partial x_j} \frac{\partial \omega}{\partial x_j} \end{aligned} \quad (3.20)$$

where  $\tilde{P}_\kappa$  is the limited production of turbulent kinetic energy,

$$\tilde{P}_\kappa = \min(P_\kappa; 10 \rho \beta_i^* \omega \kappa) \quad (3.21)$$

and the  $P_\kappa$  is the production of turbulent kinetic energy, defined based on the double dot product of the turbulent shear stress and the velocity gradient, which depends on  $S$ , the magnitude of the strain rate

$$P_\kappa = -\rho \overline{u_j u_i} \frac{\partial u_i}{\partial x_j} = \mu_t S^2 \quad (3.22)$$

The adjustment parameter is

$$\beta_i^* = \beta_\infty^* \left( \frac{4/15 + (Re_t/Re_\beta)^4}{1 + (Re_t/Re_\beta)^4} \right) \quad (3.23)$$

Here, the empirical constants are:  $\beta_\infty^*=0.09$ ;  $Re_\beta=8$ .

The turbulent Prandtl number for  $\kappa$  and  $\omega$  are:

$$\sigma_\kappa = [F_1/\sigma_{\kappa,1} + (1 - F_1)/\sigma_{\kappa,2}]^{-1} \quad (3.24)$$

$$\sigma_\omega = [F_1/\sigma_{\omega,1} + (1 - F_1)/\sigma_{\omega,2}]^{-1} \quad (3.25)$$

where  $\sigma_{\kappa,1}=1.176$ ;  $\sigma_{\kappa,2}=1.0$  and  $\sigma_{\omega,1}=2.0$ . Finally, the  $\alpha$  parameter of the  $\alpha$  the  $\omega$  production is

$$\alpha = \frac{\alpha_\infty}{\alpha^*} \left( \frac{\alpha_o + Re_t/Re_\omega}{1 + Re_t/Re_\omega} \right) \quad (3.26)$$

and

$$\alpha_\infty = F_1 \alpha_{\infty,1} + (1 - F_1) \alpha_{\infty,2} \quad (3.27)$$

$$\alpha_{\infty,1} = \frac{\beta_{i,1}}{\beta_\infty^*} - \frac{k^2}{\sigma_{\omega,1} \sqrt{\beta_\infty^*}} \quad (3.28)$$

$$\alpha_{\infty,2} = \frac{\beta_{i,2}}{\beta_\infty^*} - \frac{k^2}{\sigma_{\omega,2} \sqrt{\beta_\infty^*}} \quad (3.29)$$

where  $k=0.41$  and  $Re_\omega=2.95$ .

### 3.2.3. Boundary conditions

In order to solve the differential equations presented, appropriate boundary conditions must be defined. Figure 3.4 shows two views of the geometry detailing the axes of the reference system used and Figure 3.5 can be taken as reference, to define the necessary boundary conditions.

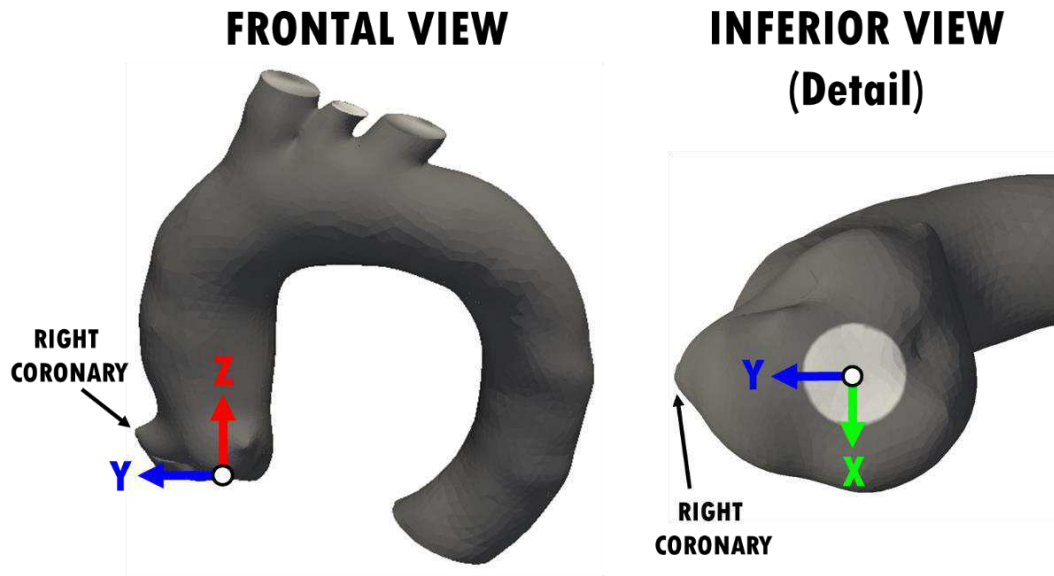


Figure 3.4 – System of reference

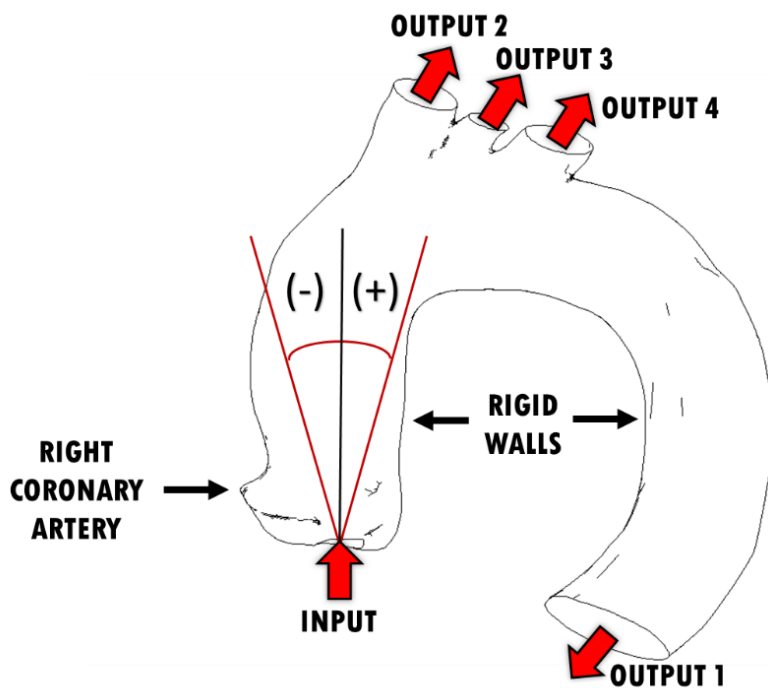


Figure 3.5 – Reference to define boundary conditions

The fluid enters the domain through the aortic valve, with diameter ( $D$ ) of 1.4 cm ( $\approx 1,5 \text{ cm}^2$ ), at the base of the ascending aorta. At the entrance, the volumetric flow rate  $Q$  is defined, and a uniform profile is employed for the velocity. The inlet plane is coincident with the plane  $x$ - $y$ , and perpendicular to the axial  $z$  coordinate. Thus, the velocity component normal to the inlet plane ( $z$  direction), equal to the average flow velocity, is

$$w_{in} = w_m = \frac{4 Q}{\pi D^2} \quad (3.30)$$

The tilt valve angle  $\theta$  is defined in relation to the  $z$  axis, where negative  $\theta$  is in the direction of right coronary artery, and positive to the posterolateral aortic wall. The magnitude of the velocity vector is

$$|\vec{V}| = \frac{w_{in}}{\cos \theta} \quad (3.31)$$

And the velocity components in the  $x$  and  $y$  directions,  $u_{in}$  and  $v_{in}$  are

$$u_{in} = 0 \quad ; \quad v_{in} = |\vec{V}| \sin \theta \quad (3.32)$$

At the inlet the turbulent quantities  $\kappa_{in}$  and  $\omega_{in}$  are also considered uniform. The turbulent kinetic energy is defined based on the inlet velocity and the turbulent intensity  $I$  (Mathieu *et al.*, 2000), and the specific dissipation is based on a length scale  $\ell$ , and the empirical constant  $C_\mu=0.09$ .

$$\kappa_{in} = \frac{3}{2} (w_{in} I)^2 \quad (3.33)$$

$$\omega_{in} = \frac{\sqrt{\kappa_{in}}}{C_\mu^{1/4} \ell} \quad ; \quad \ell = 0.07D \quad (3.34)$$

There are four outputs; the first one is defined in the descending aorta; the second one is in the brachiocephalic artery, the third one is in the left common carotid artery and the fourth one is in the left subclavian artery. At all the output regions a null diffusive flow condition was applied

$$\partial/\partial x_n = 0 \quad (3.35)$$

where  $n$  is the direction normal to the outflow plane.

At the aorta's surface, a non-slip condition was defined as a boundary condition:

$$u = v = w = 0 \quad (3.36)$$

The boundary condition of  $\kappa$  at the solid surface is also zero. However, the boundary condition for the specific dissipation in the walls ( $\omega_w$ ) is given according to Menter (1994), as a function its dimensionless value defined as:

$$\omega^+ = \frac{\omega_w \mu}{\rho (u^*)^2} \quad (3.37)$$

where  $u^*$  is the friction velocity, which can be approximated in the region of the turbulent core as

$$u^* = C_\mu^{1/4} \kappa^{1/2} \quad (3.38)$$

with  $C_\mu=0.09$ .

The dimensionless specific dissipation  $\omega^+$  is evaluated by taking into account the thickness of the molecular sublayer, according to

$$\omega^+ = \min \left( 2500, \frac{6}{\beta_\infty^* (y^+)^2} \right) \quad (3.39)$$

$y^+$  is the dimensionless wall distance

$$y^+ = \frac{\rho u^* y}{\mu} \quad (3.40)$$

As the fluid was defined as incompressible, the pressure level is not relevant, so a solution is obtained as a function of a reference pressure defined at the inlet,  $p_{in}$ , at the center of the aortic valve, which in turn is the geometric origin of the inlet plane.

### 3.3. Numerical Method

The conservation of mass, conservation of momentum and turbulence equations that characterize the problem are solved using the finite volume method

in CFD provided by the ANSYS Fluent software v17.0.

The method implement on Fluent is the Finite Volume Method (Patankar, 1980). It consists in dividing the computational domain in control volumes, within each control volume there are one point called "node". Each differential conservation equation (written in the conservative form shown) is integrated along each volume, obtaining the global balance of the variables of interest, like

$$\sum_f J_f dA_f = S_p dV_p \quad (3.41)$$

where  $J_f$  is the flux through each face  $f$ , with area  $A_f$  of a control volume, with node  $p$ , and  $S_p$  is a source term evaluated at the central node which has volume equal to  $dV_p$ . The flux has a convective and diffusive contribution. To estimate the flux, the Power-Law scheme (Patankar, 1980) was selected for all differential equation, due to its accuracy for convective diffusive flows and its stability characteristics (Versteeg, H.K.; Malalasekera, W., 2007).

To solve the pressure-velocity coupling the algorithm SIMPLE (Semi-Implicit Method for Pressure Linked Equations) (Patankar, 1980) was applied. It solves all momentum and turbulent quantities equations in a sequential form, and to enforce mass conservation, the pressure field is obtained.

The system of algebraic conservation equation of each variable was solved with the Gauss-Seidel Line-by-Line, also called TDMA line-by-line (Patankar, 1980). To accelerate convergence the additive multigrid method (Hutchinson & Raithby, 1986) was also considered.

Since the conservation equations are non-linear, sub-relaxation was employed. It takes part of value from previous iteration to dampen solution and cut out steep oscillations. The following sub-relation parameters were defined: 0.7 for momentum, 0.8 for Turbulent Kinetic Energy ( $\kappa$ ) and 0.8 for Specific Dissipation Rate ( $\omega$ ). In some cases, to improve convergence, sub-relaxation was progressively reduced up to 50% of its initial values. The system was considered converged when the residual of all differential equations was inferior to  $10^{-6}$ .

### 3.3.1. Meshing

The geometry of the aorta is very complex and needs a suitable mesh to have

a correct solution in all its points; it must consider all the geometric details and generate a reliable solution. However it must also must take into account computational time, thus, a few details of the actual patients aorta was eliminated, generating a more smooth geometry.

To generate an efficient mesh, providing an accurate solution, a grid test must performed, in order to determine a mesh independent solution, within a tolerance, which also takes in account the computing time.

To define the mesh, a grid test was performed, where three meshes were generated with different levels of detail. The meshing was created with the tetrahedron method, and it was refined in the region of the boundary layer. Figure 3.6 illustrates the mesh, where Fig 3.6a presents a view of the mesh along the aorta's surface, and Fig.3.6b shown a detail of the mesh in a cross section near the inlet. It can be clearly seen the mesh refinement near the aorta's surface.

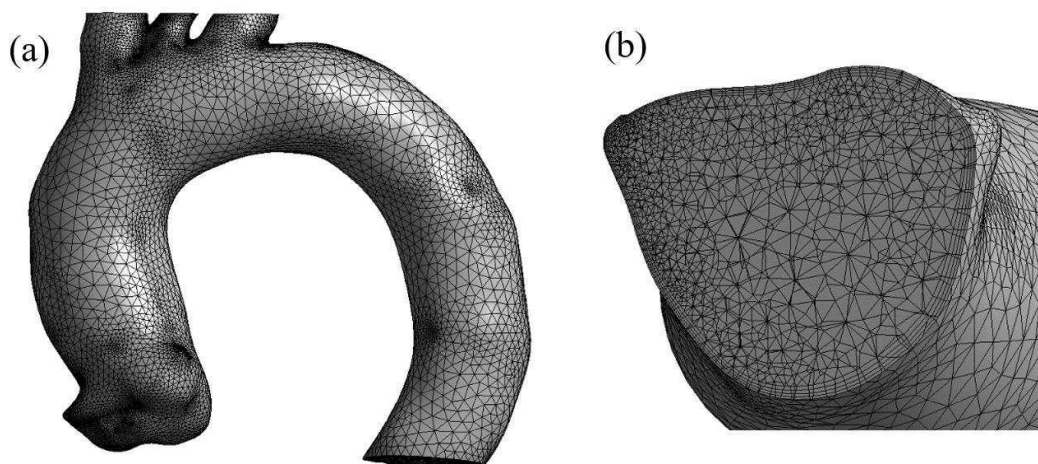


**Figure 3.6** - Mesh used in the numerical solution. (a) Complete Geometry (b) Cross-section at right coronary level.

The grid test is present in Appendix A1. To evaluate the mesh independent solution, the delta pressure and velocity along the center line of the jet near the inlet was determined. The mesh independent solution was defined in order to guarantee the quality of the solution in the inlet valve region. Based on the grid test results, a domain with 400.000 nodes was applied to all the cases studied in the present work. The Gauss-Seidel algorithm was used to solve the resulting algebraic system. In order to accelerate the convergence to solve such a system, the multigrid algorithm was used (Hutchinson and Raithby, 1986). When the residuals of conservation equations reached values lower than  $10^{-6}$ , the system reached the convergence.

## 4 RESULTS

This chapter reports the numerical results obtained from the three-dimensional aortic model described in the previous chapter. The study is emphasized in the ascending aorta segment, where the most interesting phenomena is present.

It should be recalled here that, the computational domain was defined based on the images obtained in a CT scan. From these images, a 3D digital geometry model was created, which was employed in the present work. It was also employed to build a 3D silicone phantom and measurements of the flow field were performed by Azevedo (2017) employing Particle Image Velocimetry (PIV) technique. It is an optical method used to obtain instantaneous velocity measurements and related properties in fluids. In that experimental work, the fluid was seeded with tracer particles which, for sufficiently small particles, were assumed to faithfully follow the flow dynamics. The fluid with entrained particles was illuminated so that particles were visible. The motion of the seeding particles was used to calculate speed and direction, in another words the velocity field of the flow being studied.

At the present work, the first set of analyses performed consisted in validating the solution by comparison with the experimental data of Azevedo (2017). Then, the influence of small tilt angles of the inlet flow is investigated. Lastly, analyze the effect of modifying the turbulent intensity at the inlet flow.

It should be mentioned here, that several preliminary steps were performed before the analysis of this work results. Not only a grid test, presented in Appendix A1, was performed, but also comparisons with four variations of the two-equation turbulence model were carried on and are presented in Appendix A2.

To allow comparison with Azevedo (2017) measurements, the properties of the same fluid (aqueous glycerin solution) employed in the experiments was defined. The dynamic viscosity was set as  $\mu = 7.2$  cP and density as  $\rho = 1054$  kg/m<sup>3</sup>.

The valve inlet diameter (equal to the 3D silicone phantom) was equal to 1.4 cm. The range of flow rate  $Q$  investigated varied from 2.6 lt/min to 25 lt/min, which are representative values during the systole period. Table 4.1 presents the

corresponding Reynolds number of the cases analyzed. Six different inlet valve angles were considered:  $-4^\circ$ ,  $-2^\circ$ ,  $0^\circ$ ,  $+1^\circ$ ,  $3^\circ$  and  $5^\circ$ , these were chosen according to the experimental work of Azevedo (2017).

The inlet turbulent intensity was established as 0.1, based on the values measured by Azevedo (2017). However, its influence in the solution was also examined, and additional simulations were performed by prescribing inlet turbulent intensity equal to 0.3, 0.5 and 0.7.

For all cases, the same outflow flow rate distribution was imposed, based on average values in the human body, according to Alastruey et al. (2016) and Nardi et al. (2014). Table 4.2 presents the outflow boundary condition at the descending aorta (output 1), the brachiocephalic artery (output 2), left carotid artery (output 3) and left subclavian artery (output 4).

**Table 4.1 – Reynolds variation**

<b><math>Q</math> (lt/min)</b>	<b><math>w_{in}</math> (m/s)</b>	<b>Re</b>
2.6	0.28	630
3.3	0.36	800
5.3	0.57	1285
15	1.62	3640
25	2.71	6060

**Table 4.2 – Outflow distribution**

<b>OUTPUT</b>	<b>PERCENTAGE OF FLOW RATE</b>
1	69.1%
2	19.3%
3	5.2%
4	6.4%

For the visualization of the internal fields, a central plane of 6cm high and oriented with respect to the right coronary artery (Figure 4.1a), was selected. According to the particular position of the chosen center plane, the left wall of the plane corresponds to the anterior wall of the aorta and the right wall corresponds to the posterior wall.

To analyze the effects on the walls, the complete geometry was examined, although emphases was given to the wall where the inlet jet impinges (right anterolateral wall of the ascending aorta) (Figure 4.1b).

Before, presenting the results, at the next section, comparison with the experiment data of Azevedo (2017), which was employed in the validation of the simulations of this work is discussed.

To better generalize the results it is convenient to normalize the governing parameters.

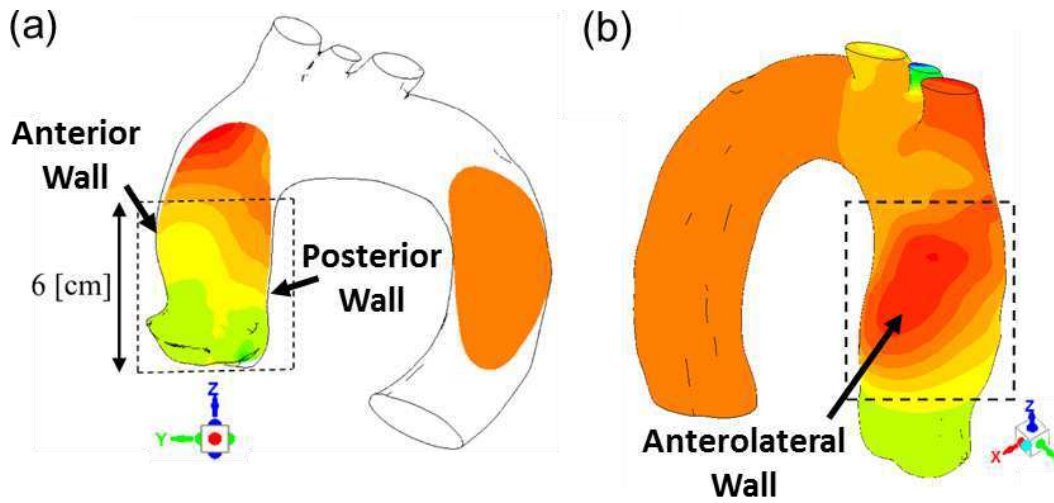


**Figure 4.1** – Regions of interest for the analysis. (a) For internal fields. (b) For analysis on the wall

#### 4.1. Dimensionless Variables

The flow was normalized by the inlet axial velocity,  $w_{in}$ , and inlet diameter  $D$

$$X_i = \frac{x_i}{D} \quad ; \quad U_i = \frac{u_i}{w_{in}} \quad ; \quad P = \frac{p - p_{in}}{\rho w_{in}^2 / 2} \quad (4.42)$$

Additional variables examined are:

- The wall shear stress,  $\tau_{wall}$ , which is proportional to the gradient of the velocity component tangent to the wall in relation to the wall normal direction

$$T_{wall} = \frac{\tau_{wall}}{\rho w_{in}^2 / 2} \quad ; \quad \tau_{wall} = \mu \left( \frac{\partial u_s}{\partial n} \right)_{wall} \quad (4.43)$$

- Dimensionless Turbulent Reynolds tensor,  $-\rho \overline{u'_i u'_j}$ .

$$\tau_{t_{ij}}^* = -\frac{\overline{u'_i u'_j}}{w_{in}^2} \quad (4.44)$$

The dimensionless  $y - z$  turbulent shear stress (or shear Reynolds stress), was determined employing

$$\tau_{yz}^* = -\frac{\overline{v'w'}}{w_{in}^2} = \frac{1}{\text{Re}} \left( \frac{\partial V}{\partial Z} + \frac{\partial W}{\partial Y} \right) \quad (4.45)$$

where Re is the Reynolds number, the flow parameter that governs the flow, given by Eq.(3.1).

The dimensionless deviatoric normal turbulent Reynolds stress are

$$\overline{W'W'} = -\frac{\overline{w'^2}}{\rho w_{in}^2} = -\frac{2}{\text{Re}} \frac{\partial W}{\partial Z} \quad (4.46)$$

$$\overline{U'U'} = -\frac{\overline{u'^2}}{\rho w_{in}^2} = -\frac{2}{\text{Re}} \frac{\partial U}{\partial X} \quad ; \quad \overline{V'V'} = -\frac{\overline{v'^2}}{\rho w_{in}^2} = -\frac{2}{\text{Re}} \frac{\partial V}{\partial Y} \quad (4.47)$$

- Turbulence intensity  $I$ , defined as

$$I = \frac{\sqrt{2/3} \kappa}{w_{in}} \quad ; \quad \kappa = \frac{1}{2} (\overline{u'^2} + \overline{v'^2} + \overline{w'^2}) \quad (4.48)$$

- Vorticity components:

$$\varpi_x = \frac{1}{2} \left( \frac{\partial w}{\partial y} - \frac{\partial v}{\partial z} \right) \quad (4.49)$$

$$\varpi_y = \frac{1}{2} \left( \frac{\partial u}{\partial z} - \frac{\partial w}{\partial x} \right) \quad ; \quad \varpi_z = \frac{1}{2} \left( \frac{\partial v}{\partial x} - \frac{\partial u}{\partial y} \right) \quad (4.50)$$

- Dimensionless enstrophy:  $\xi^2$ .

$$\xi^2 = \left( \frac{D}{w_{in}} \right)^2 (\varpi_x^2 + \varpi_y^2 + \varpi_z^2) \quad (4.51)$$

## 4.2. Experimental-Data

In this section, a few detail regarding the experimental data of Azevedo (2017), employed to validate this work simulations, is presented.

In the experimental assembly, five planes were defined as illustrated in Figure 4.1a. The central plane was employed as the main reference, with two planes at each

side. The distance between each plane is equal to 4mm. The region of interest was from the inlet valve to 6 cm above it.

Azevedo (2017) measured, with the PIV technique, the instantaneous velocity field in the planes  $y - z$  indicated in Figure 4.1a, at several time instants. From these data, the time average values  $v$  and  $w$  were obtained, with Eq. (3.2). Then, the time variation of the velocity fluctuations in the  $y$  and  $z$  were determined, by subtraction of the mean variable from the instantaneous values. Finally, after obtaining the time variation of the product of  $v'w'$ , the shear Reynolds stress could be obtained,  $\overline{v'w'}$ . Similar procedure was employed to obtain the axial normal Reynolds stress  $\overline{w'^2}$ . These variables were normalized by the inlet axial velocity,  $w_{in}$ .

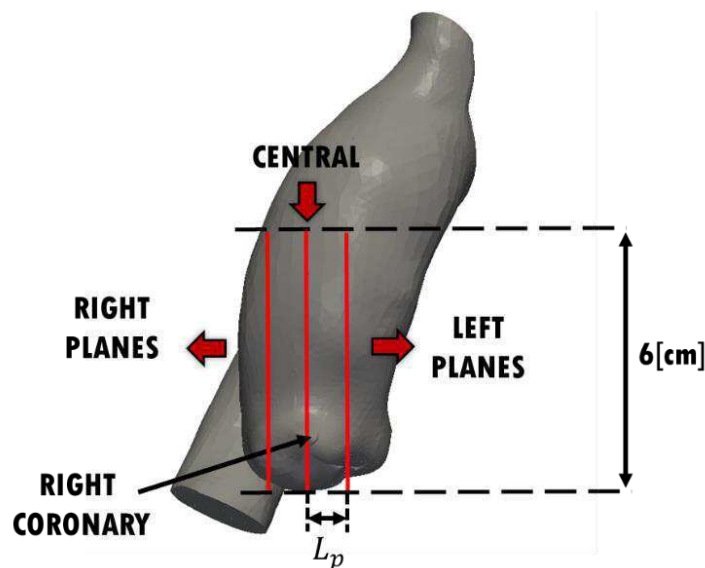


Figure 4.2 – Nomenclature and position of the planes

Before proceeding, one observation must be made, regarding the positioning of the planes, where the measurements were performed. The positioning of the reference central plane, was performed in an approximated way, i.e, the central plane, was experimentally positioned by visually passing by the center of the inlet valve, and taking as reference the right coronary (see Fig.4.2).

### 4.3. Experimental-Numerical Comparison

For comparison of numerical results with the experimental data, several parallel planes were analyzed. Numerically, the central plane, was precisely defined at the center of the inlet valve, passing by the right coronary, i.e., no inclination angle of the inlet valve was considered for these comparisons.

Although, Azevedo (2017) presented data at five planes, for the numerical cases, since there was a greater availability of planes, more planes were considered, to have a better global idea of the behavior of the flow. Therefore, in addition to the central plane, 6 left and 6 right planes, separated by a distance of 2mm were examined. The number assigned to each plane corresponds to the distance  $L_p$  in millimeters that it has with respect to the central plane.

Two sets of data are employed here for comparison purposes, corresponding to intermediate volume flow rate values: 5.3 lt/min and 3.3 lt/min.

The first parameter analyzed was the axial velocity, for inlet flow rate of  $Q = 5.3$  lt/min, in Fig.4.3 and 4.4, corresponding to experimental and numerical results, respectively.

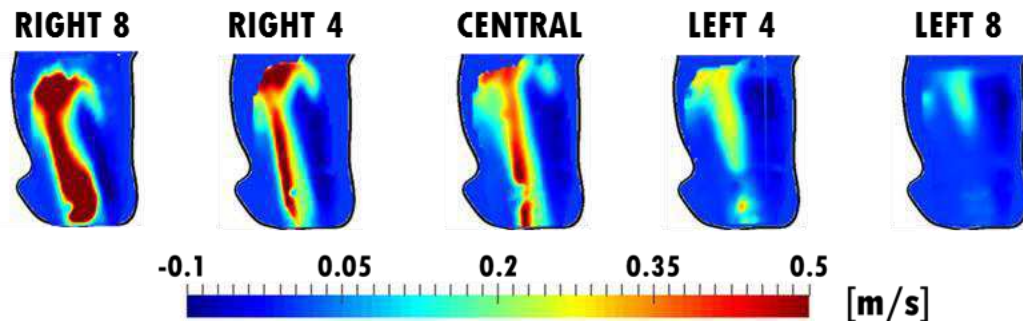


Figure 4.3 – Experimental axial velocity contours. Azevedo (2017).  $Q = 5.3$ lt/min

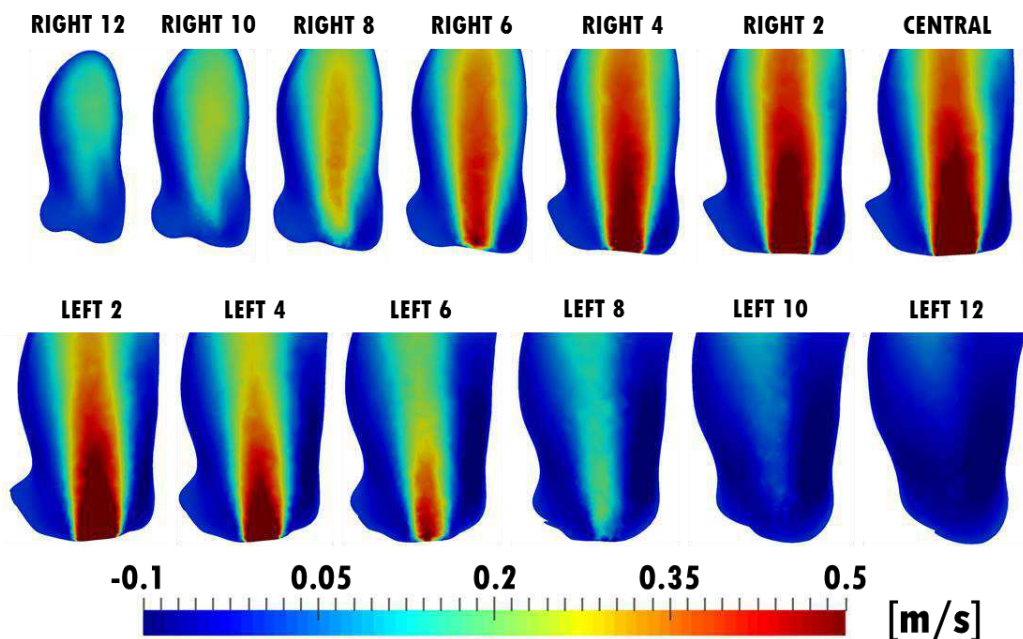


Figure 4.4 – Numerical axial velocity contours.  $Q=5.3$ lt/min

Isocontours of the mean axial velocity  $w$  measured experimentally are presented in Figure 4.3, where an increase in its values can be seen in the right planes and a decrease in the right planes. These results, might indicated that, the experimental plane, considered as “central”, was not actually located perfectly aligned with the inlet central jet, and it fact, the plane labeled as “right 8”, is probably more aligned with the inlet jet, and perhaps is the actual central plane. Nevertheless, an important observation can be made from these data, i.e. there is a notorious inclination of the inlet jet towards the anterior wall. It should be noted that at the top of all the experimental planes there is a blue zone in which there is some uncertainty in the measurement due to the limits of the laser illumination plane used in the PIV.

Figure 4.4 shows the isocontours of the axial velocity obtained numerically. To better compare the results, the same range of velocities was employed. A first observation of the numerical data, shows that the highest values of the axial velocity occurred at the central plane, having a decrease in both directions, left and right. This behavior is expected, since the inlet jet, centered in the central plane, should have its intensity reduced as one moves away from this plane, due to the spread of the jet. A slight inclination of the inlet jet can also be seen, although much less intense than the one observed experimentally.

Comparing both sets of results, it was found a displacement of the experimental planes in relation to the numerical ones. In specific terms, there is an equivalence between the “right 8” experimental plane and numerical “right 2” and “central” planes. Further, the experimental “right 4” plane seems to corresponded to the numerical “left 2” plane. There is also an equivalence between the experimental “central” plane with the “left 4” and “left 6” numerical planes. Further, the experimental “left 4” plane resembles the numerical “left 8” plane. Finally, the experimental “left 8” plane has a similarity with the numerical “left 10” and “left12” planes.

Although, it can be said, that there is an equivalence in the results, there are certain variations and displacements, which may be due to a slight variation in the reference system (already mentioned). It can also be due to an inclination of the measurement planes (positioning related to the right coronary), uncertainties in the measurement and, hydraulic pump vibrations. It is also due to the difficulty of defining precise angulation and a valid flow characterization. It should also be

considered that in the experimental arrangement a nozzle was used in the valve inlet area and in the numerical arrangement an orifice was used.

Analyzing the isocontours for the flow rate of  $Q = 3.3$  lt/min (Figures 4.5 and 4.6), the same observations regarding the equivalence of the results can be made, i.e., there are similarities between numerical and experimental results, if the correspondence between planes is shifted.

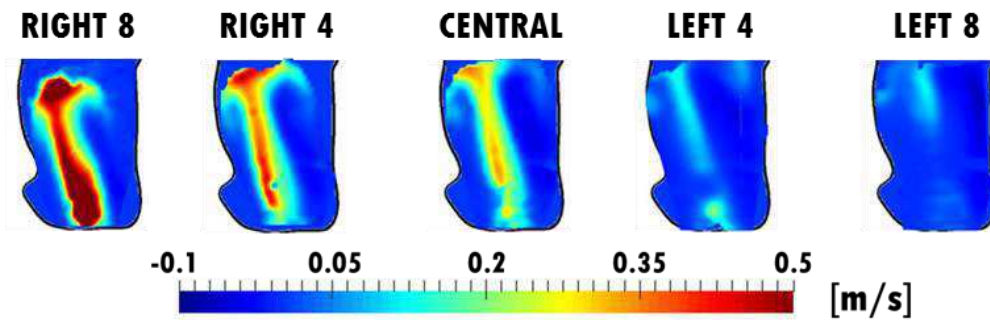


Figure 4.5 – Experimental axial velocity contours. Azevedo (2017).  $Q = 3.3$  lt/min

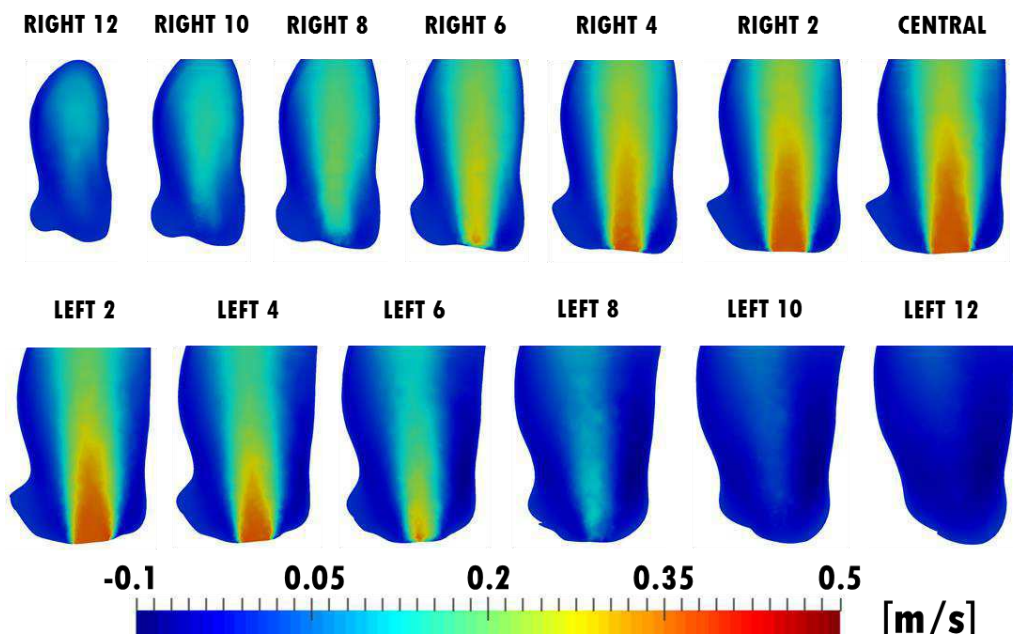


Figure 4.6 – Numerical axial velocity contours.  $Q=3.3$ lt/min

The second variable compared here in Figures 4.7 through 4.10 is the dimensionless shear Reynolds stress,  $\tau_t^*$ , which is a useful parameter to appreciate the influence of the turbulence in the flow.

Figure 4.7 shows the results of the experimental case for  $Q=5.3$  lt/min, where the highest values can be seen in experimental plane “right 8”, decreasing as one moves in direction to plane left 8”. Note that the Reynolds stress is positive at the

left size of the inlet jet and negative at the right side, indicating that the main direction of the shear Reynolds stress is away from the center of the jet, which again can be seen to be clearly inclined. Figure 4.8 shows the results of the numerical case, which were a little more centered and symmetrical, and presented a high concentration of values between the “right 4” and “left 4” planes. The equivalence of the planes was practically the same as discussed in relation to the axial velocity, having again a displacement of between 4 and 6mm.

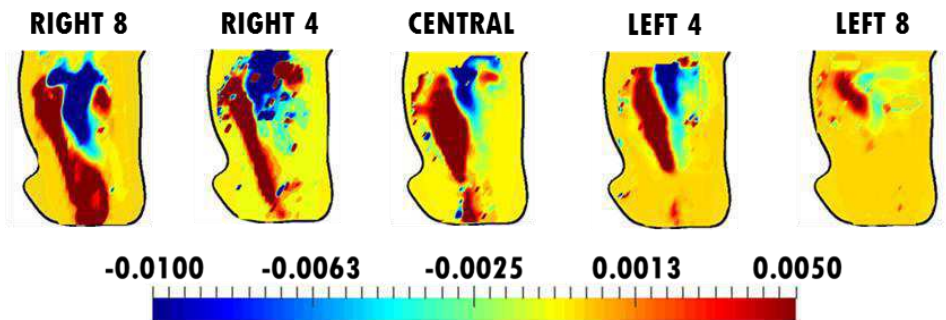


Figure 4.7 – Experimental dimensionless shear Reynolds stress. Azevedo (2017).  
 $Q=5.3\text{lt/min}$

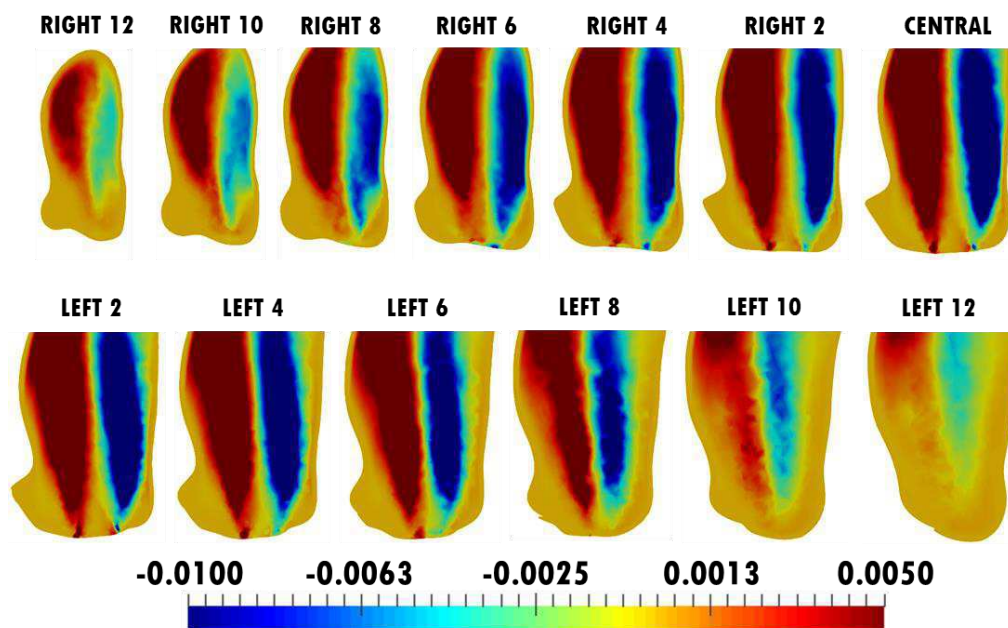


Figure 4.8 – Numerical dimensionless shear Reynolds stress.  $Q=5.3\text{lt/min}$

The same type of comparison of the dimensionless shear Reynolds stress is presented in Figures 4.9 and 4.10, corresponding to the experimental and numerical results for flow rate,  $Q=3.3\text{ lt/min}$ . The same comments discussed for the higher flow rate are also observed here.

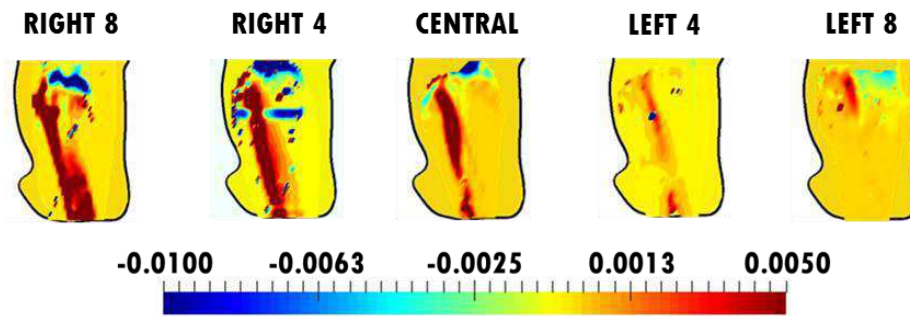


Figure 4.9 – Experimental dimensionless shear Reynolds stress. Azevedo (2017).  
 $Q=3.3\text{lt/min}$

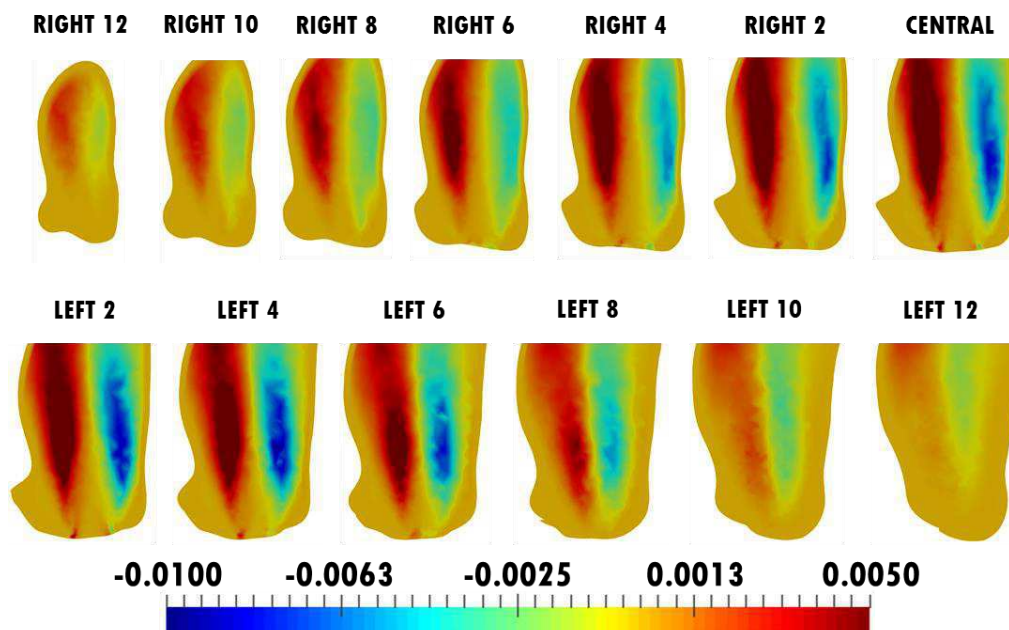


Figure 4.10 – Numerical dimensionless shear Reynolds stress.  $Q=3.3\text{lt/min}$

The last parameter analyzed was vorticity, which describes the local spinning motion of each point of the field, demonstrating their tendency to rotate. Once experimentally, only the velocity components in the y and z direction are available, only the vorticity in x direction was analyzed. The numerical and experimental results for the dimensional x-component vorticity is presented in Figs. 4.11 through 4.14, corresponding to the two flow rates.

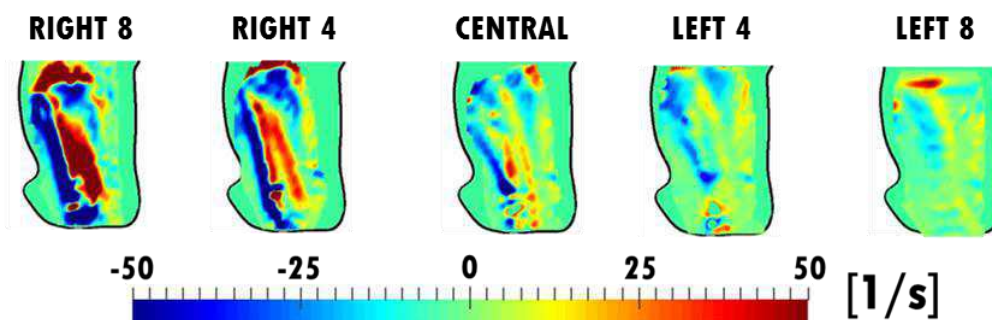


Figure 4.11 – Experimental x-vorticity. Azevedo (2017).  $Q=5.3\text{lt/min}$

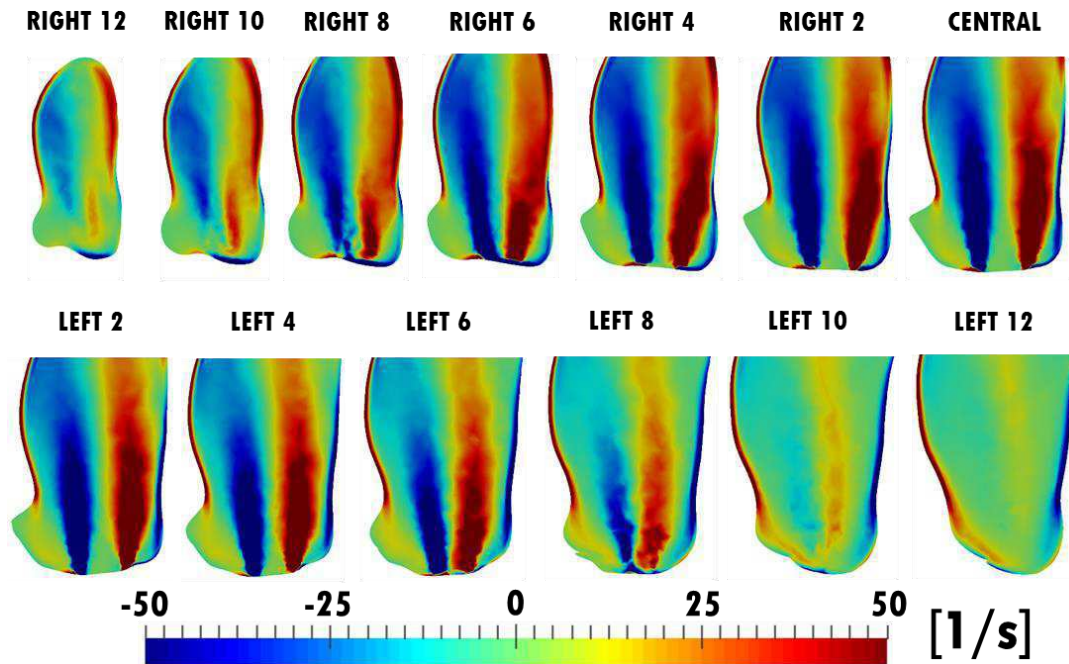


Figure 4.12 – Numerical  $x$ -vorticity.  $Q=5.3\text{lt/min}$

The experimental results for the flow rate of  $Q = 5.3 \text{ lt/min}$  are presented in Figure 4.11. A high concentration of values can be noticed on both sides of the jet and a slight inclination of the values towards the anterior wall. The Figure 4.12 shows the numerical results which illustrate very well the performance of the vorticity phenomenon inside the aorta, both in the central body and in the walls and also towards the left and right lateral regions, where the effect of the vorticity gradually decreases when moving away from the central zones of the jet. These results presented an equivalence of the planes equal to that was found in all the previous parameters, having again a plane displacement between 4 and 6mm.

The same type of comparison of the  $x$ -vorticity is performed comparing Figures 4.13 and 4.14, corresponding to the experimental and numerical results for flow rate,  $Q=3.3 \text{ lt/min}$ . In this case, the vorticity presents values lower than those demonstrated by the higher flow rate, however the same comments discussed for that case are also observed here.

From these results, it was considered that a reasonable representation of the flow was obtained, and that the influence of the tilt inlet valve angle could be explored.

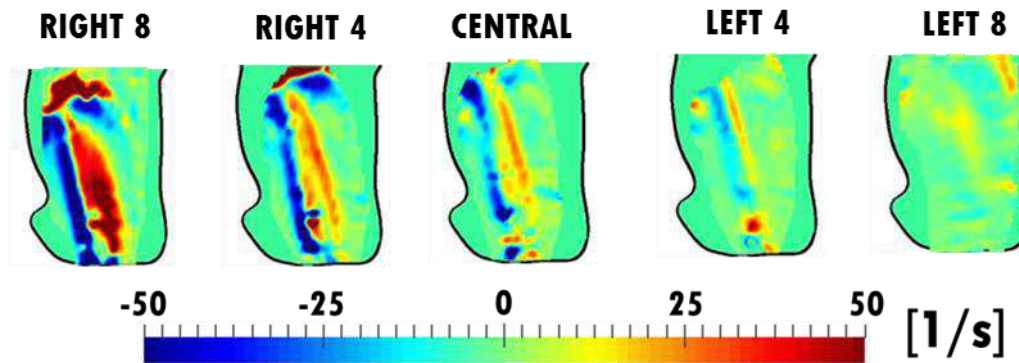


Figure 4.13 – Experimental x-vorticity. Azevedo (2017).  $Q=3.3\text{lt/min}$

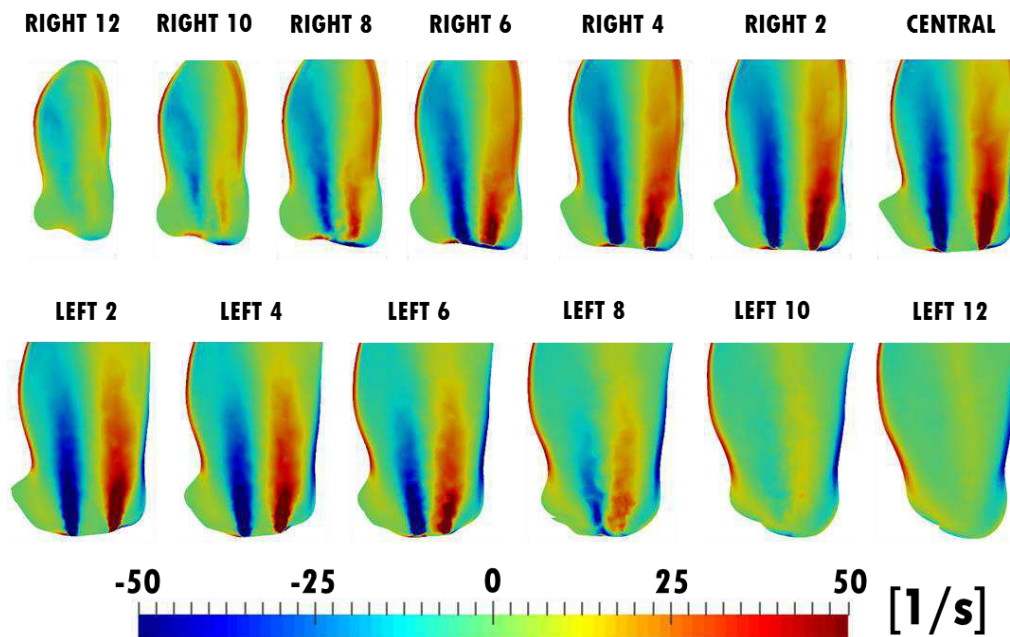


Figure 4.14 – Numerical x-vorticity.  $Q=3.3\text{lt/min}$

#### 4.4. Influence of Tilt Valve Angle on Blood Flow

When an aortic valve prostheses are introduced by a TAVR procedure, it might be placed with a certain angle. At the present work, the influence of the tilt angle on the flow field is examined, since these variations may have an important influence on the various hemodynamic properties of the aortic flow. Simulations were performed using 6 different angles ( $-4^\circ$ ,  $-2^\circ$ ,  $0^\circ$ ,  $+1^\circ$ ,  $+3^\circ$ ,  $+5^\circ$ ) for different velocities of the pulsatile cycle. The results shown in this section correspond to the most representative velocities of the systole period, the maximum of 25 lt/min, an intermediate of 15 lt/min and a low of 2.6 lt/min. It was evaluated the influence of the tilt angle on the axial velocity, pressure, wall shear stress (WSS) and Reynolds stress.

To have an overall idea of the flow inside the aorta, and easily understand the flow behavior Figure 4.15, illustrates pathlines inside the aorta for the highest flow rate,  $Q=25\text{lt/min}$ . The pathlines are colored by the axial velocity intensity, on a scale represented in the lower part of the figure. In this particular analysis, the solution with three inlet valve angles are presented: the central position of the aortic valve and two extreme angles ( $-4^\circ$ ,  $0^\circ$  and  $+5^\circ$ ). For the three tilt angles, the inlet jet impinges left side of the aorta and induces a recirculation that extends itself up the distal ascending aortic segment. However, it can be seen that small variations in the input angle redirects the jet from one wall of the aorta to another, causing a change in the internal hemodynamics, by displacing the main recirculation region and the location of the initial impact of the jet.

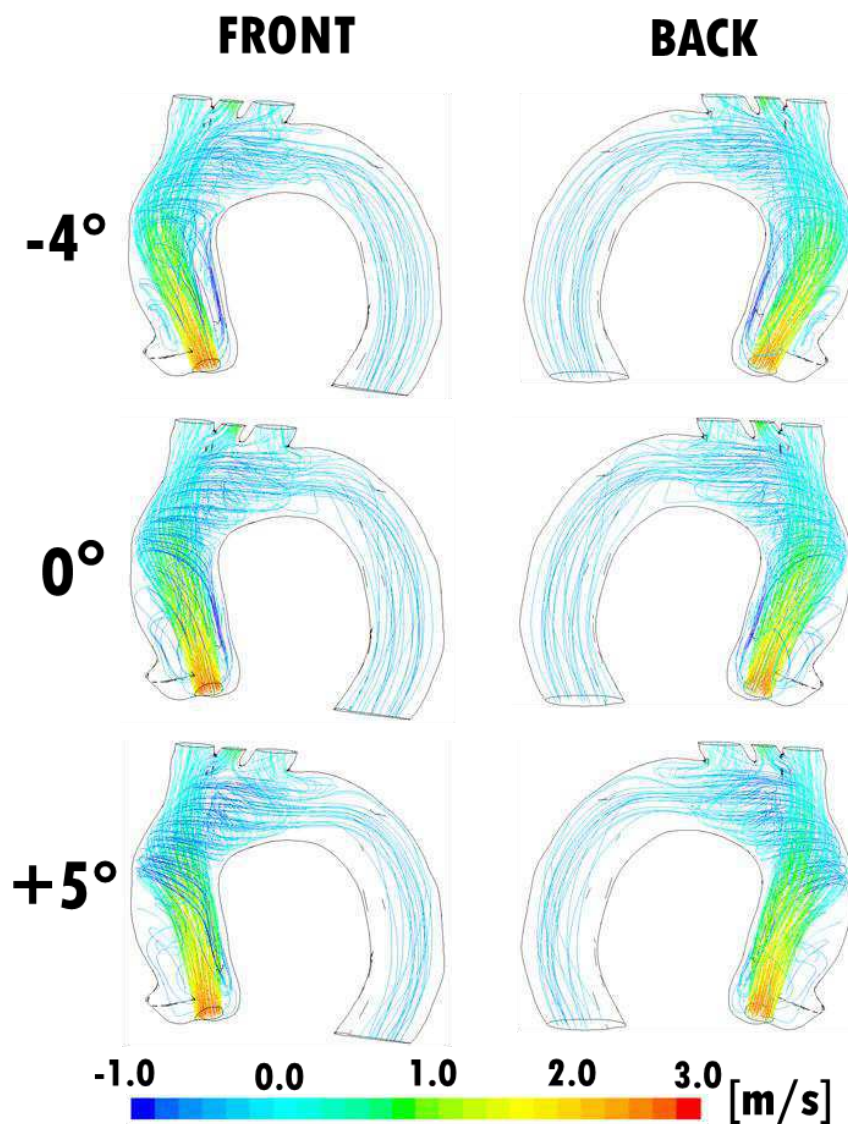


Figure 4.15 – Variation of pathlines when tilting the aortic valve angle.  $Q=25\text{lt/min}$

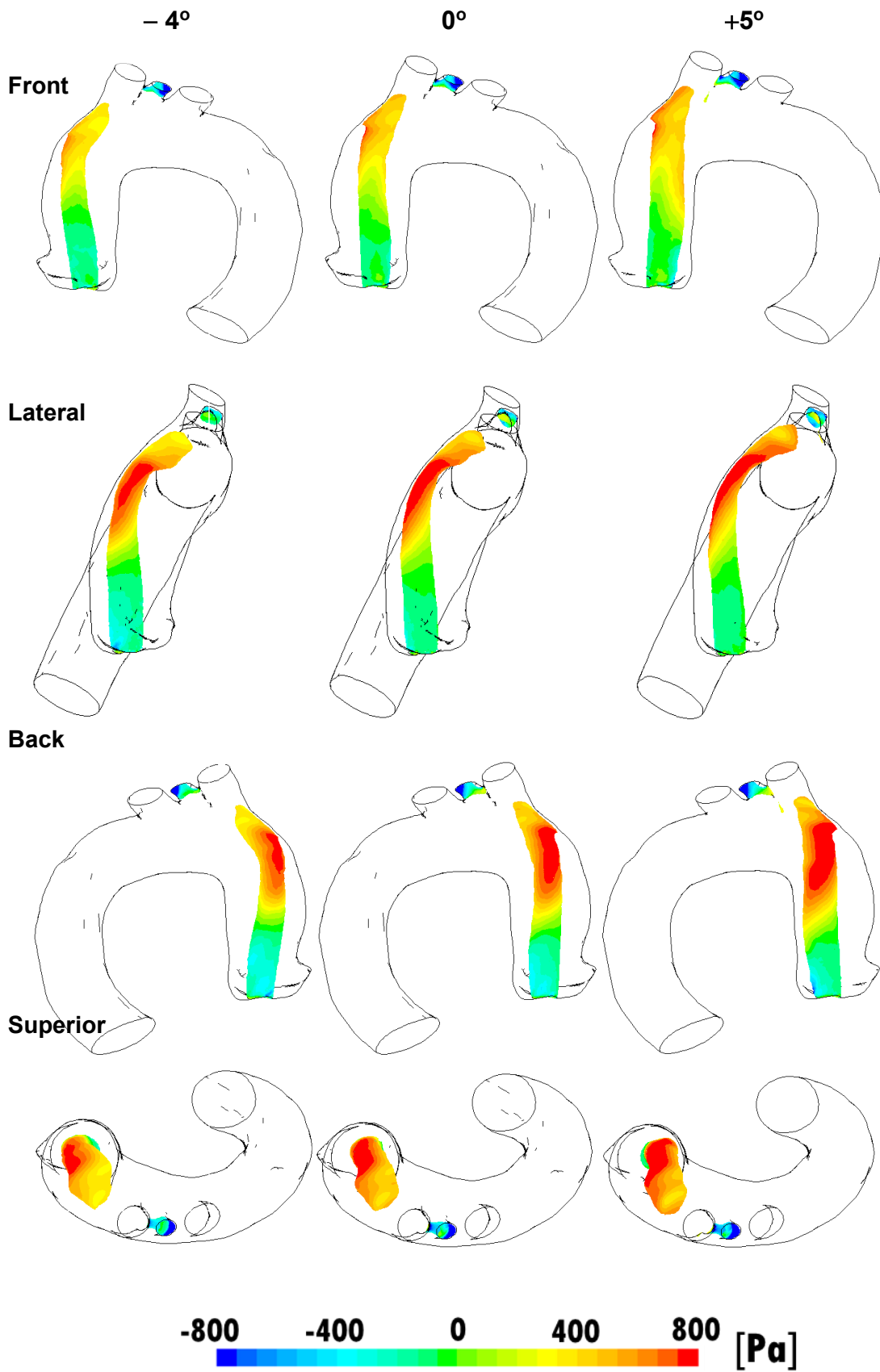
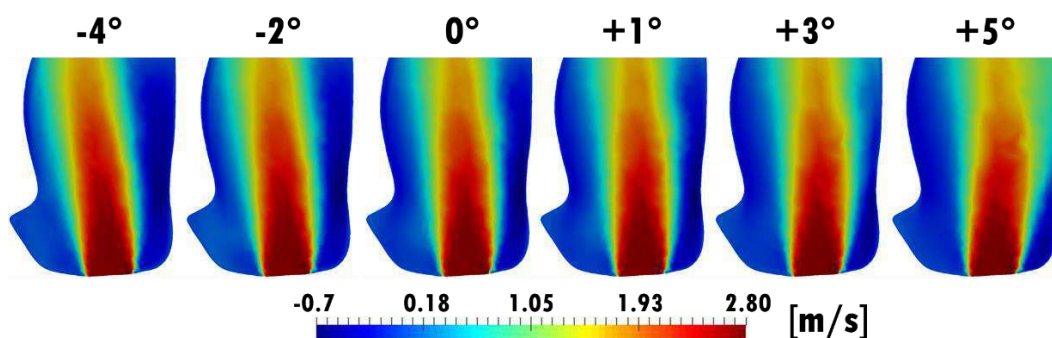


Figure 4.16 – Iso-surface surface of  $u_z = 1.3$  m/s, colored by dimensionless pressure. Three tilt angle ( $-4^\circ$ ,  $0^\circ$  and  $+5^\circ$ ).  $Q = 25$ lt/min

For the same three angles ( $-4^\circ$ ,  $0^\circ$  and  $+5^\circ$ ) and maximum flow rate  $Q=25\text{lt/min}$ , Figure 4.16 presents an isosurface corresponding to constant axial velocity component,  $u_z = 1.3 \text{ m/s}$ . The surface is colored by the dimensionless pressure. To better visualize the flow, four different view are presented (front, lateral, back and superior). It can be seen that for the three tilt angles, the inlet jet impinges at the left side of aortic wall, where the pressure reaches its maximum value. Due to the aortic wall curvature, the jet is bent in direction of the upper coronaries. For the negative angle (opposite direction than the aortic curvature), a stronger curvature of the jet can be observed. For the positive tilt angle, the inlet jet is more aligned with the aortic shape, and the jet is more vertical.

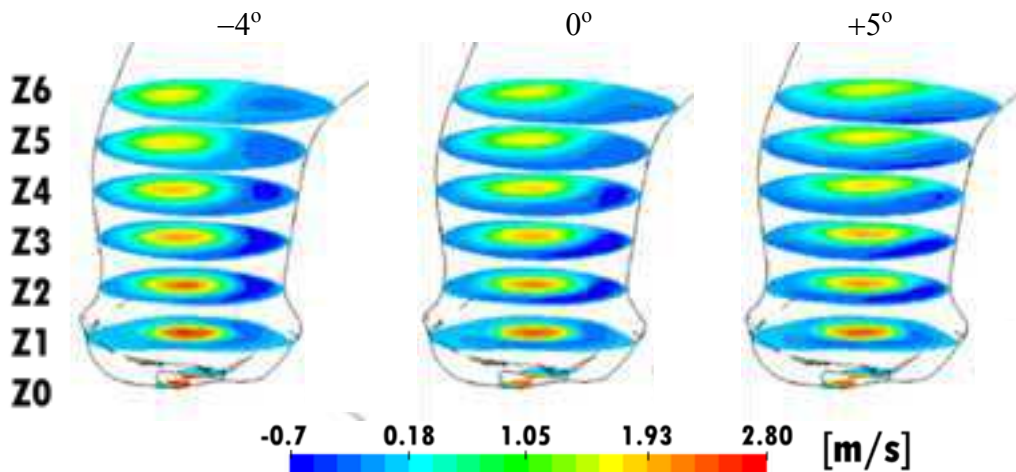
#### 4.4.1. Axial Velocity

Figure 4.17 presents these variations more specifically; by comparing the iso-contour of the axial velocity component at the central plane (as described in Fig. 4.1a, oriented with respect to the center of the jet and the right coronary and comprising 6cm of ascending aorta). The highest flow rate  $Q=25\text{lt/min}$  was selected to illustrate the flow field. Here are shown all six angles studied ( $-4^\circ$ ,  $-2^\circ$ ,  $0^\circ$ ,  $+1^\circ$ ,  $+3^\circ$ ,  $5^\circ$ ). It can be seen a progressive modification of the axial velocity field. As the jet tilts to the left (negative angles) reaches the anterior aortic wall without a substantial modification of the jet diameter. Furthermore, it is identifiable a region with negative velocity to the right of the jet, indicating the presence of a recirculation. On the other hand, as the jet tilts to the right (positive angles), it moves away from the anterior wall and approaches the posterior aortic wall, the jet undergoes a spreading and a smaller region of negative velocities occurs at the posterior side of the aorta.



**Figure 4.17** - Axial velocity fields varying the tilt angle.  $Q=25\text{lt/min}$

To obtain a complete spatial visualization, the axial velocity for the inlet flow rate of  $Q=25$  lt/min was analyzed in different transverse planes, distributed every 1 cm from the entrance and again covering 6cm of ascending aorta. Figure 4.18 shows the distribution of the planes in the geometry and Figure 4.19 shows them individually.



**Figure 4.18** – Axial velocity contours at transverse planes in geometry, for different tilt angles.  $Q=25$ lt/min

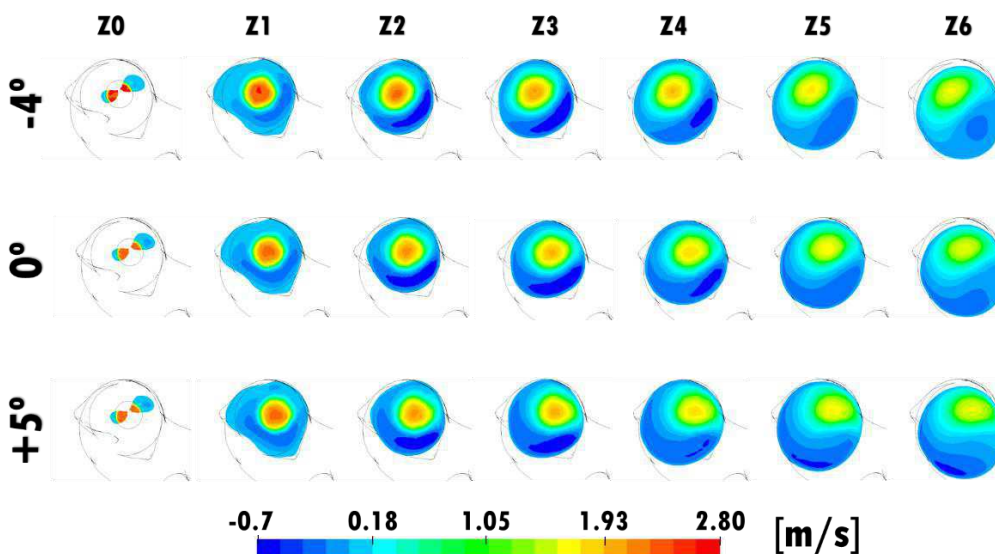


**Figure 4.19** – Individual transverse planes showing the axial velocity fields, for different tilt angles.  $Q=25$ lt/min.

In Figures 4.18 and 4.19, the results for only the extreme and central inlet angles are presented ( $-4^\circ$ ,  $0^\circ$ ,  $+5^\circ$ ). Thanks to these combined visualizations it can be noted that in all cases the jet tends to hit the right lateral aortic wall. However, due to the inclinations of the valve the impact zone is modified, the inclination

towards the anterior regions for negative angles and towards posterior regions in positive angles are intensified, which modifies the zones of mechanical stress in the walls of the ascending aorta. These figures also allow to identify the regions of recirculations (negative velocity), which are most present in the region between 2 and 4 centimeters of ascending aorta.

Figure 4.20 shows a comparison of the axial velocity fields for the three analyzed flow rates, using the same ranges of values. It can be clearly seen the effect on the tilt angle for the three flow rates, directing the flow to left and right aortic wall depending if the angle is negative or positive, but varying according to its magnitude.

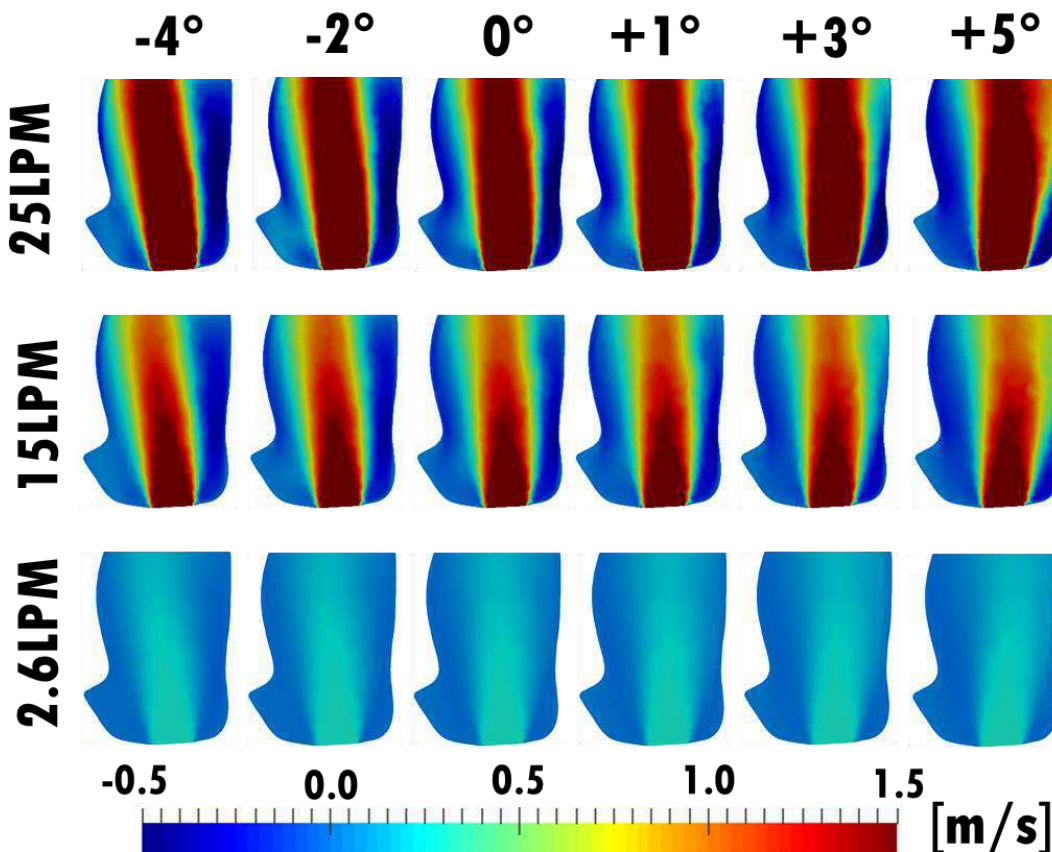


**Figure 4.20** – Comparison of axial velocity fields varying the tilt angle for  $Q = 2.6$  lt/min; 15 lt/min and 25 lt/min.

To better evaluate the effect of the inlet flow rate, the same result is plotted employing the dimensionless axial velocity for the three flow rate, but only for the two extreme tilt angles and central case in Figure 4.21. This allows to elucidate that the phenomenon is present at all velocities of the pulsatile cycle, and the same conclusions described for the highest flow rate is valid for all flow rates.

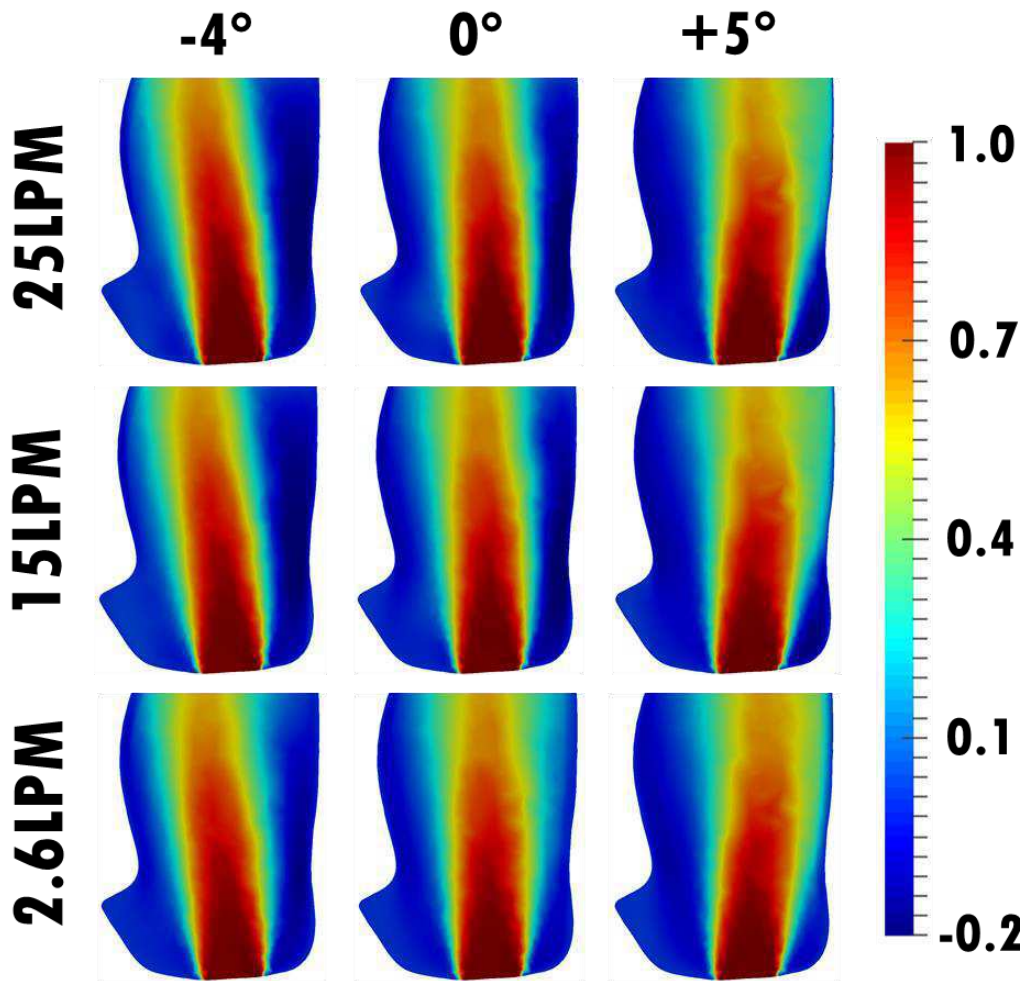


Figure 4.21 – Comparison of dimensionless axial velocity fields varying the tilt angle for  $Q = 2.6$  lt/min; 15 lt/min and 25 lt/min

#### 4.4.2. Enstrophy

To have an idea of the vorticity of the flow, it is presented in Figure 4.22, the iso-contour of the dimensionless enstrophy. As shown in Eq. 4.10, the enstrophy is equal to the square of the modulus of the vorticity. The field corresponding to the central jet is compared with the solution obtained for the two extreme angles ( $-4^\circ$  and  $+5^\circ$ ) for the three flow rates ( $Q = 2.6$  lt/min; 15 lt/min and 25 lt/min). Once again the influence of the jet inclination is clearly seen. Further, the flow rate does not change the dimensionless enstrophy distribution, which presents a kind of symmetry around the inlet jet, with high values at the shear layer around the jet, decreasing as the flow evolves, and near the artic wall.

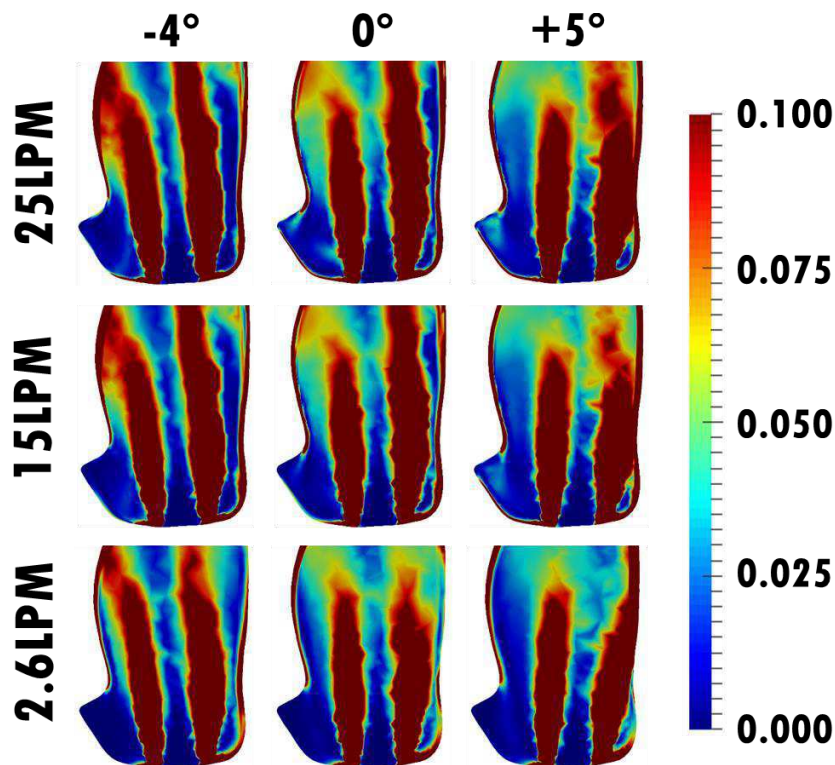


Figure 4.22 – Dimensionless enstrophy varying the tilt angle.

$Q = 2.6 \text{ lt/min}; 15 \text{ lt/min and } 25 \text{ lt/min.}$

#### 4.4.3. Pressure

To analyze the pressure, the highest flow rate  $Q=25\text{lt/min}$  was also selected to visualize the inlet angle influence on the pressure field at the central plane (Figure 4.23). The pressure values are relative with respect to the inlet region. The highest-pressure value is near the impinging jet region. Note a change in high-pressure areas, which are located at the anterior wall at negative tilt angles and move to the posterior wall at positive tilt angles. As the inlet jet impinges the aorta surface, the pressure increases substantially. This high pressure induces the downward flow observed in the previous figures.

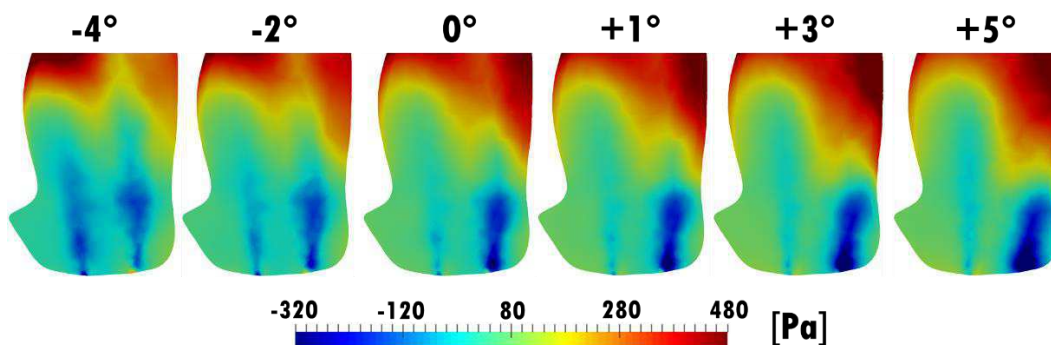
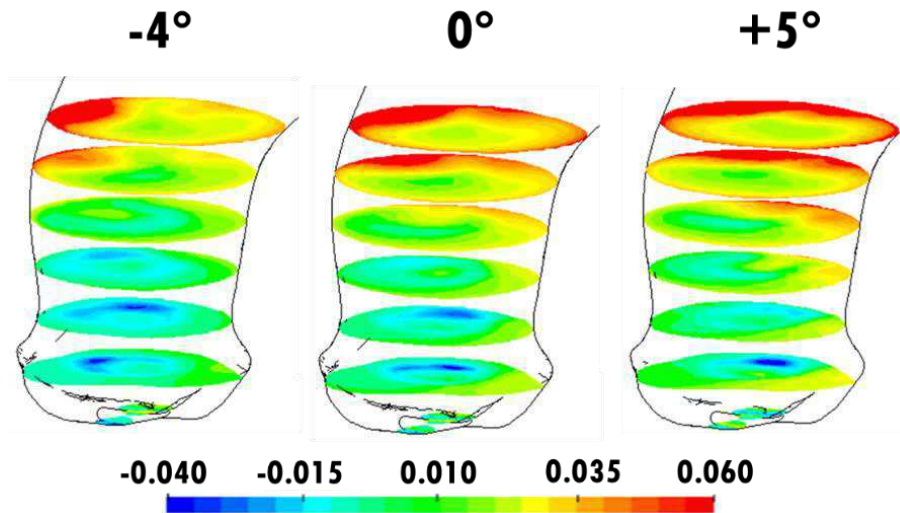


Figure 4.23 – Pressure fields in the central plane varying the tilt angle.  $Q=25\text{lt/min}$

Figure 4.24 illustrates the dimensionless pressure distribution for  $Q = 25$  lt/min and for the extreme and central inlet angles ( $-4^\circ$ ,  $0^\circ$ ,  $+5^\circ$ ) at different transverse planes, distributed every 1cm from the entrance and again covering 6cm of ascending aorta. Note the high pressure value at the artie wall where the jet impinges it, and lower pressure inside the inlet jet.



**Figure 4.24** – Dimensionless pressure contours at transverse planes in geometry, for different tilt angles.  $Q=25$ lt/min

To compare the effect of the pressure at the various velocities of the pulsatile cycle, the dimensionless pressure is shown in Figure 4.25. It is possible to notice similarities between the dimensionless pressure fields, allowing the analysis performed at the highest flow rate to be extrapolated to lower velocities.

To better analyze the pressure distribution in the upper region, from the anterior to posterior aorta region, where the most important variations occur, the pressure distribution along a particular line for the different tilt angle was examined. The line was generated, given by the intersection of the central plane with a transverse plane to 6 cm from the input, as shown in Figure 4.26. The pressure values present in this line were analyzed for 5 input angles, and are shown in Fig. 4.27. The solution corresponding to angle  $+1^\circ$  was withdrawn to obtain a better visualization of the other results and because it did not present significant variations with respect to the central angle.

The pressure distribution along the described line is plotted at Figure 4.27 for three inlet flow rates,  $Q = 25$  lt/min; 15 lt/min and 2.6 lt/min.

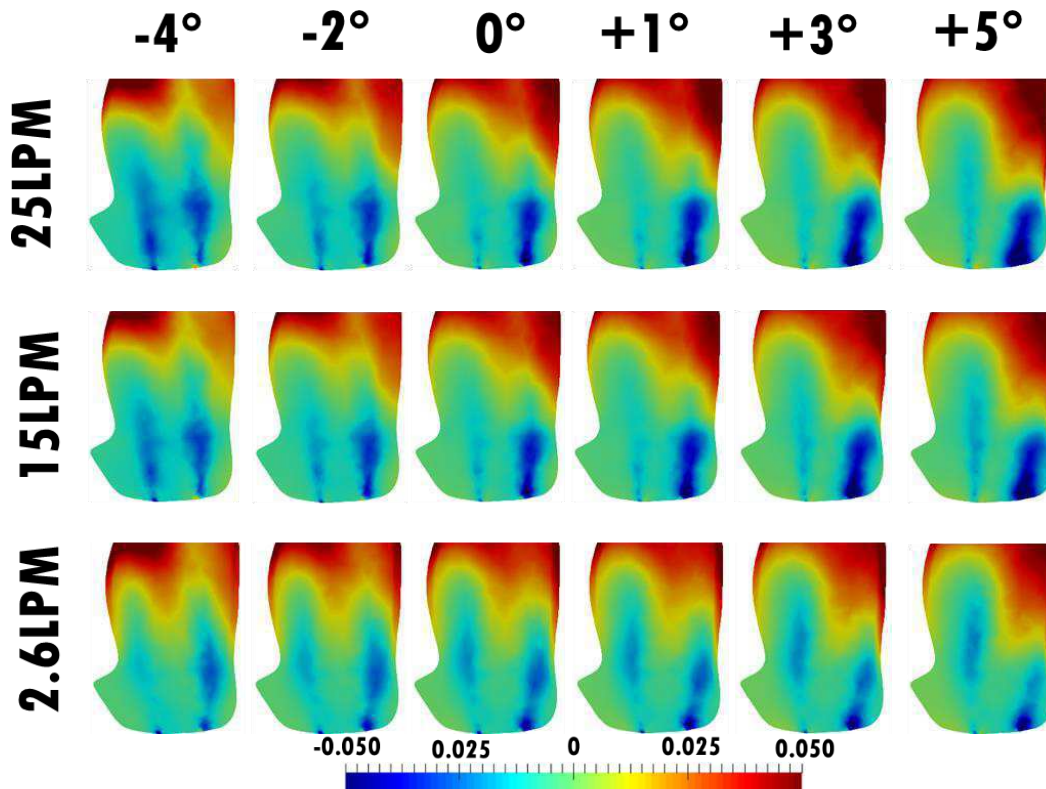


Figure 4.25 – Dimensionless pressure at different flow rates and tilt angles:

$Q = 25 \text{ lt/min}; 15 \text{ lt/min and } 2.6 \text{ lt/min}$

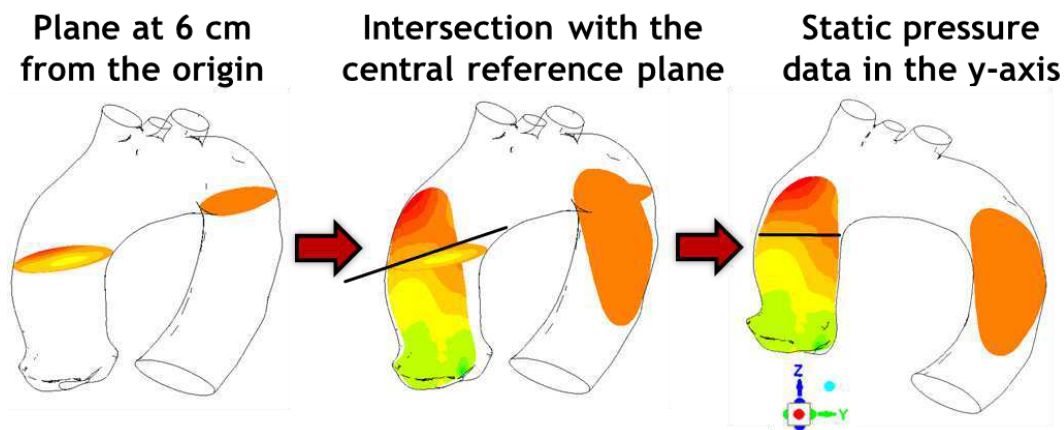
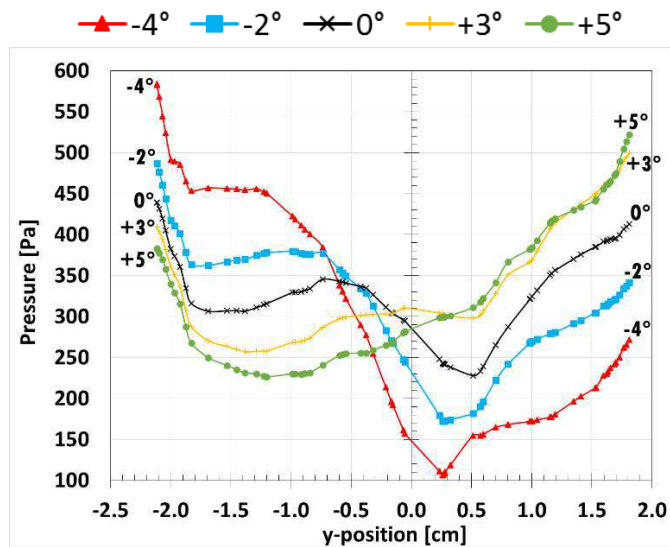
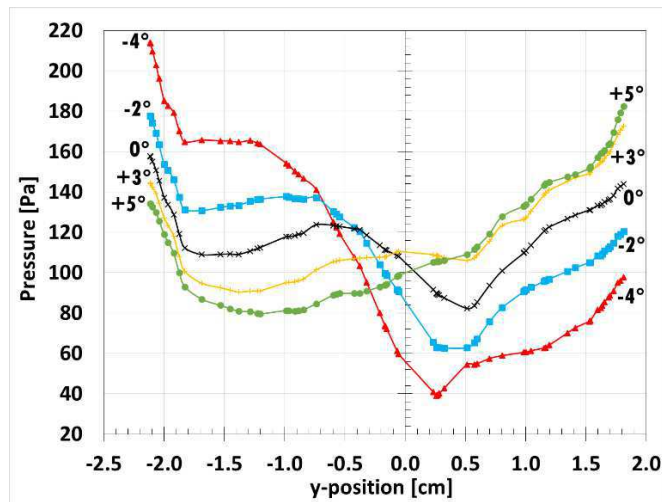


Figure 4.26 – Obtaining pressure lines

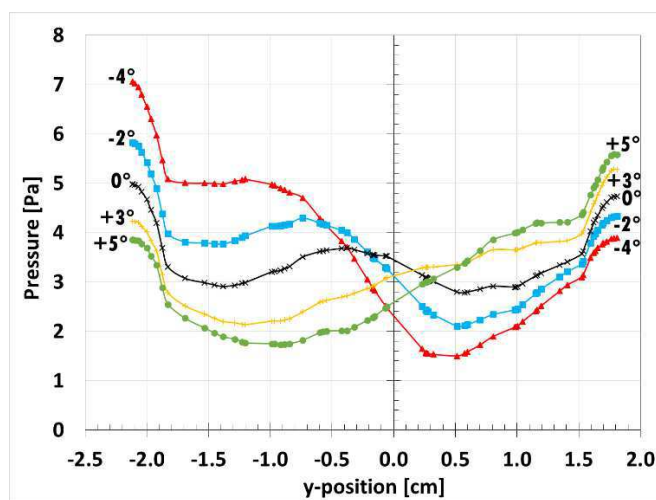
Analyzing Fig. 4.27, it can be seen that, when the jet enters with negative angles, the pressure reaches high values in the left region, and it is reduced towards the right, achieving at a maximum delta pressure of approximately 470Pa in the case of the most negative angle ( $-4^\circ$ ). The reverse effect occurs with positive angles, with lower values in the anterior wall of the aorta and higher values in the posterior wall, with a maximum delta pressure of approximately 300Pa in the case of the most positive angle ( $+5^\circ$ ). As the jet centralizes, the pressure tends to have more stable values.



(a)  $Q=25\text{lt/min}$



(b)  $Q=15\text{lt/min}$



(c)  $Q=2.6\text{lt/min}$

Figure 4.27 – Pressure variation along line y at z=6 cm. Influence of inlet tilt angle.

$Q = 25 \text{ lt/min}$ ;  $15 \text{ lt/min}$  and  $2.6 \text{ lt/min}$ .

#### 4.4.4. Shear Reynolds Stress

The presence of fluctuation in turbulent flow enhances mixture, increases diffusion and consequently the pressure drop. The Reynolds stress represents the influence of the velocity fluctuation in the mean flow. Figure 4.28 presents the effect of the inlet angle in the dimensionless shear Reynolds stress for three flow rates at the central plane.

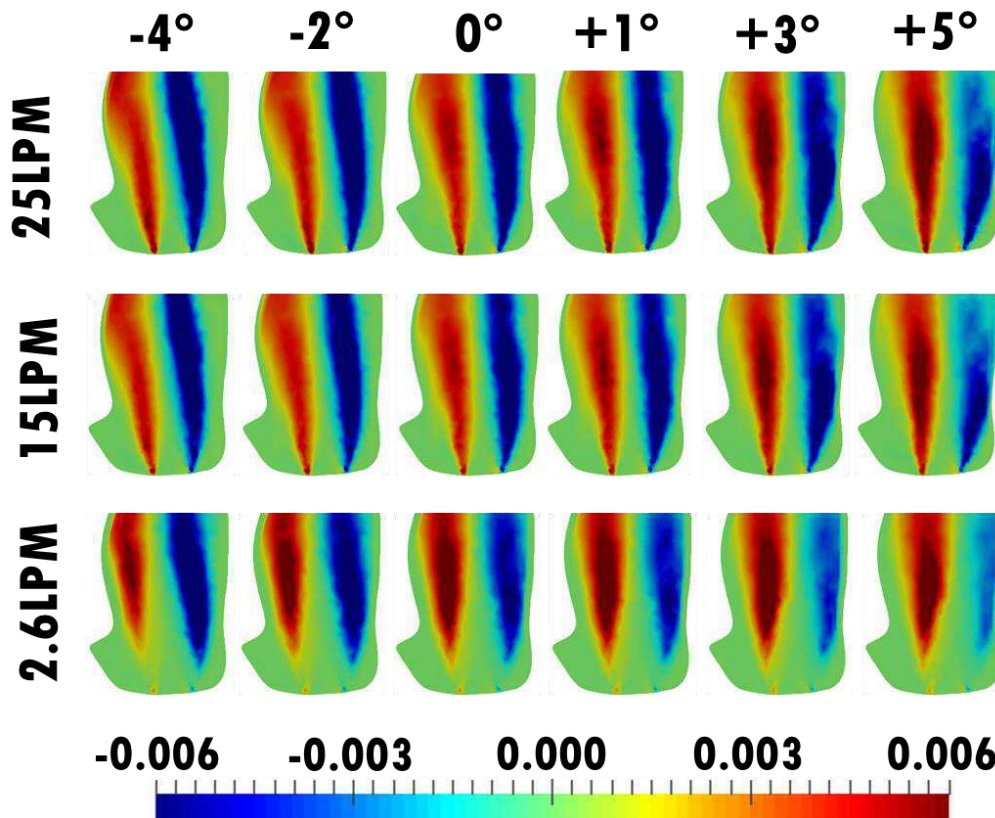


Figure 4.28 – Dimensionless Reynolds Stress as the inclination of the jet changes.

Figure 4.28 shows that the dimensionless turbulent shear stress is zero at the center of the jet, positive in the direction of positive axis  $y$  and negative in the opposite direction. Further, it tends to zero at the walls where there is a laminar sub-layer and the turbulence influence vanishes.

As expected, at the  $0^\circ$  angle a certain symmetry can be identified in area and magnitude on both sides of the jet. As the jet has a negative inclination, the symmetry of area is conserved, but larger values are presented to the right of the jet and on the anterior aortic wall. As the angles of inclination become positive, both the area and magnitude symmetry are lost, which highlights the dispersion of the jet; high values move away from the anterior wall and are concentrated in the

posterior wall and mostly in the center of the aorta where the area and magnitude are greater.

These results imply that when a large inclination of the prosthetic valve occurs in both senses generates a greater concentration of the Reynolds tensor in the central regions, although more centralized in positive angles. In addition, in negative angles, there is a high concentration in the anterior wall and in positive angles, although smaller, there is a concentration in the posterior wall.

The influence of the tilt angle is somewhat independent of the flow rate. Naturally, that higher dimensional values occur, as the flow rate increases, but the tendency of the jet are similar.

#### 4.4.5. Shear Stress at Aortic Wall - WSS

In order to analyze the variations of shear stress at the aortic wall, called here “wall shear stress” (WSS), three-dimensional images of the whole geometry were obtained for the high velocity case. The aorta is visualized in such a way as to focus on the region where the greatest effects occur, which in this particular case occurs in the right anterolateral wall of the ascending aorta.

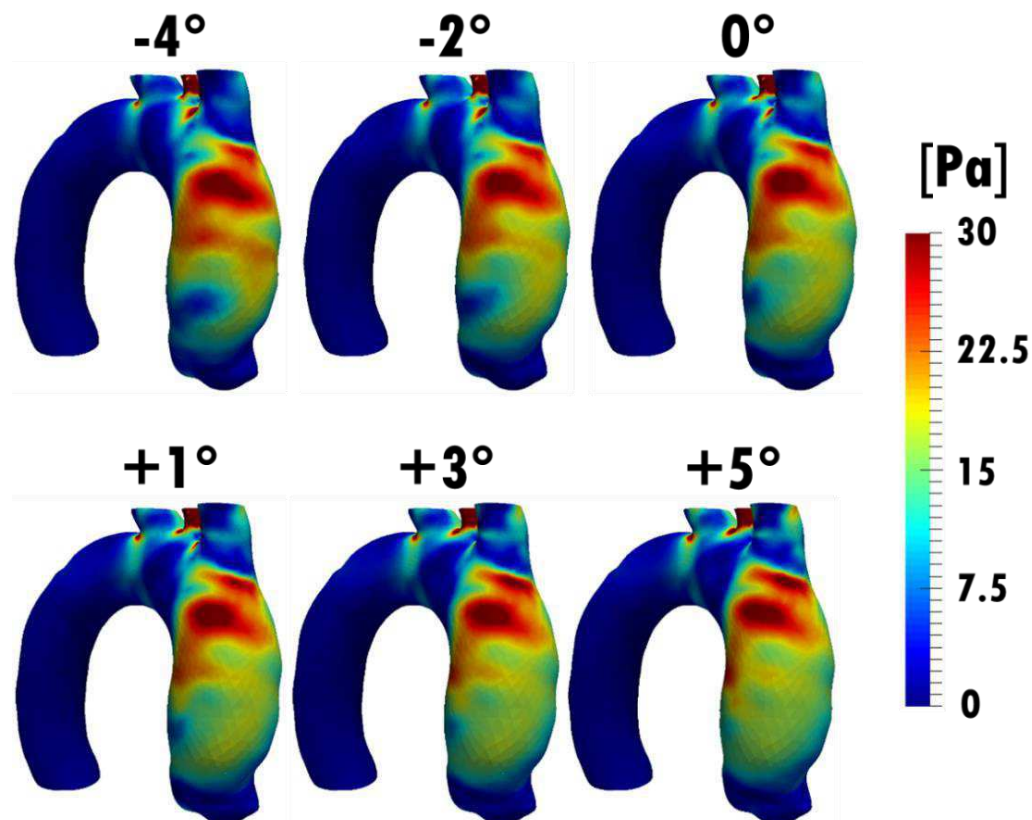


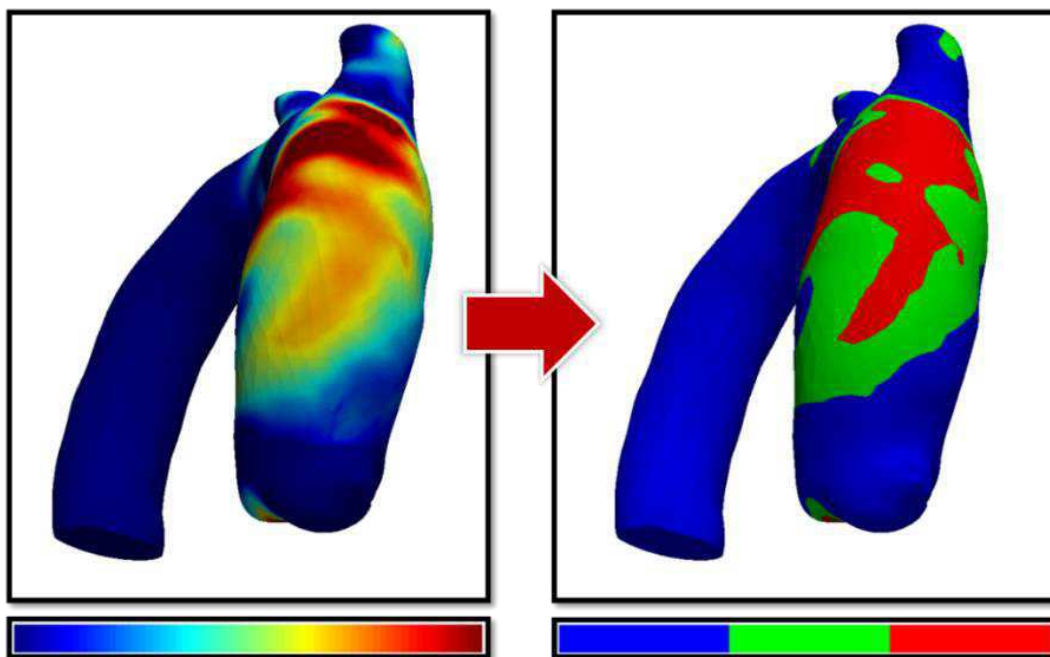
Figure 4.29 – Influence of tilt valve angle on WSS.  $Q=25\text{lt/min}$

Figure 4.29 shows the results, where it can be perceived that when the angle is modified from negative values to positive values there is a displacement and a reduction of the highest values of WSS. This implies a displacement and decrease of mechanical stress on the ascending aortic wall by modifying the inclination of the prosthetic valve.

To better identify the high shear stress region, a procedure described in the next sub-section was carried out with focus in the critical region of the aorta.

#### 4.4.5.1. Quantitative analysis of WSS

To better identify the region of the aorta with critical (high) wall shear stress, a smaller section of the aorta was selected. Further, only three sub-range of values WSS were defined, as can be seen in Figure 4.30, where blue corresponds to low values, green corresponds to intermediate values and red to high values.



**Figure 4.30** – Change in the ranges of values

The critical sub-region of the aorta where the major effects occur, was defined as the right anterolateral wall of the ascending aorta. The selected zone is specified in Figure 4.31.

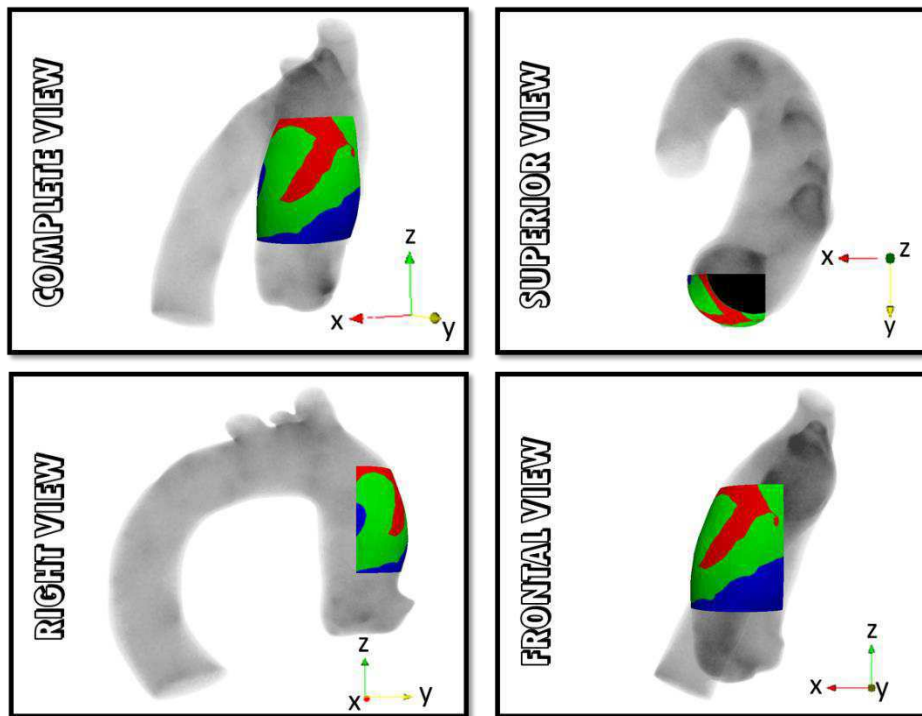


Figure 4.31 – Sample for quantitative analysis

This procedure was implemented to extract the results from the data obtained with all six-inlet angles of inclination. The results are illustrated in Figure 4.32, where the variations are more clearly seen, making evident the substantial decrease of the red area, which represents the high values of WSS.

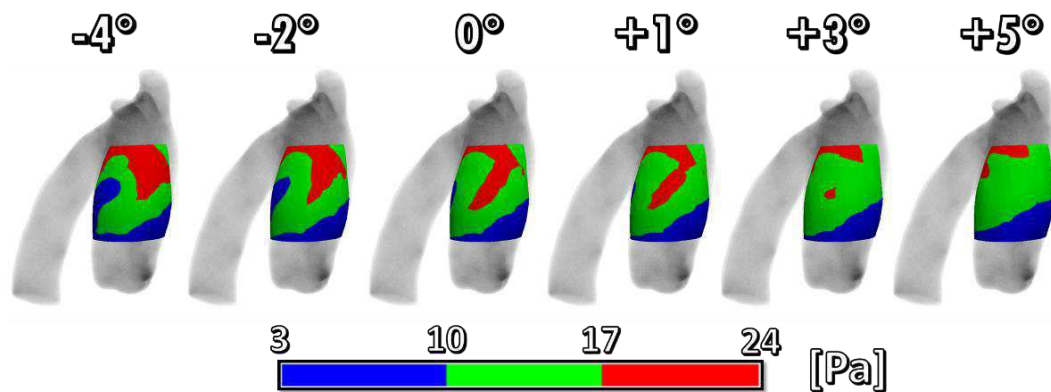


Figure 4.32 – Identification of high WSS area at the aortic wall as a function of the tilt angle.  $Q=25\text{lt/min}$ .

Figure 4.33 shows the percentages of area covered by each region, where the low WSS zone tends to remain a constant value of approximately 47% and the high WSS zone is progressively reduced by varying the tilt angle. In Figure 4.34, it is possible to observe this area variation of the highest values of WSS, even having a maximum reduction of 15% when passing from an angle  $-4^\circ$  to  $+3^\circ$ .

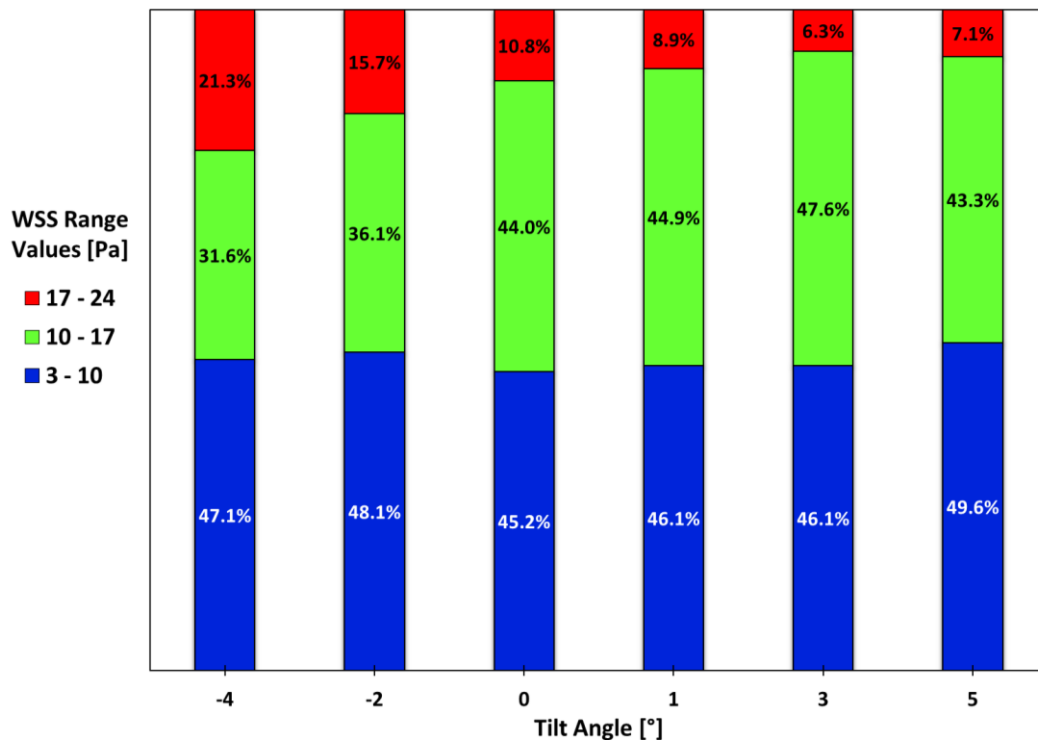


Figure 4.33 – Percentage distribution of WSS on the anterolateral wall of the ascending aorta varying with the tilt angle

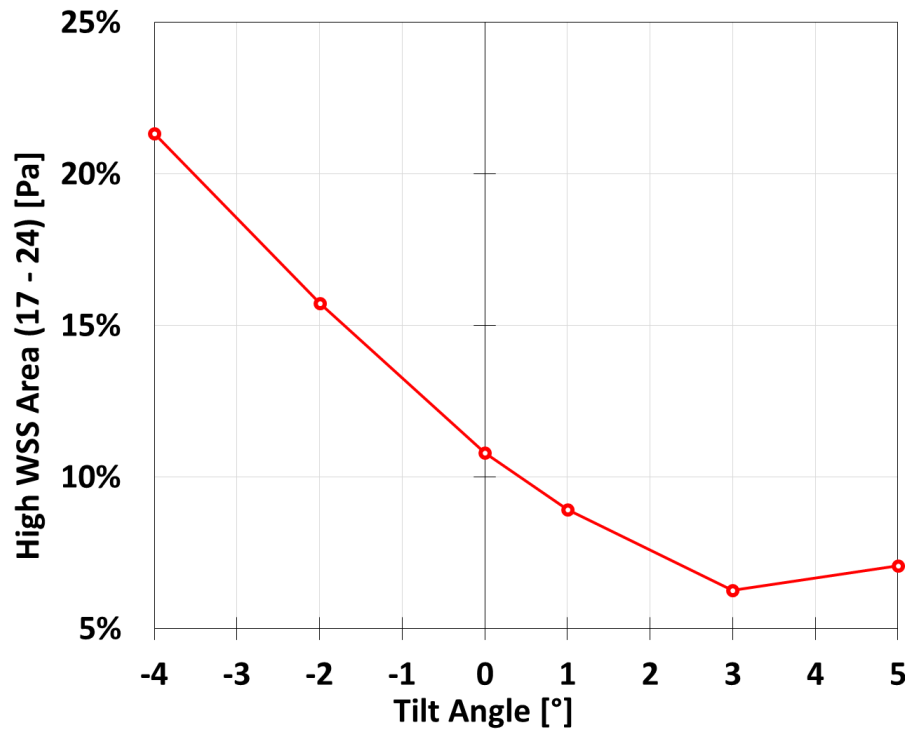
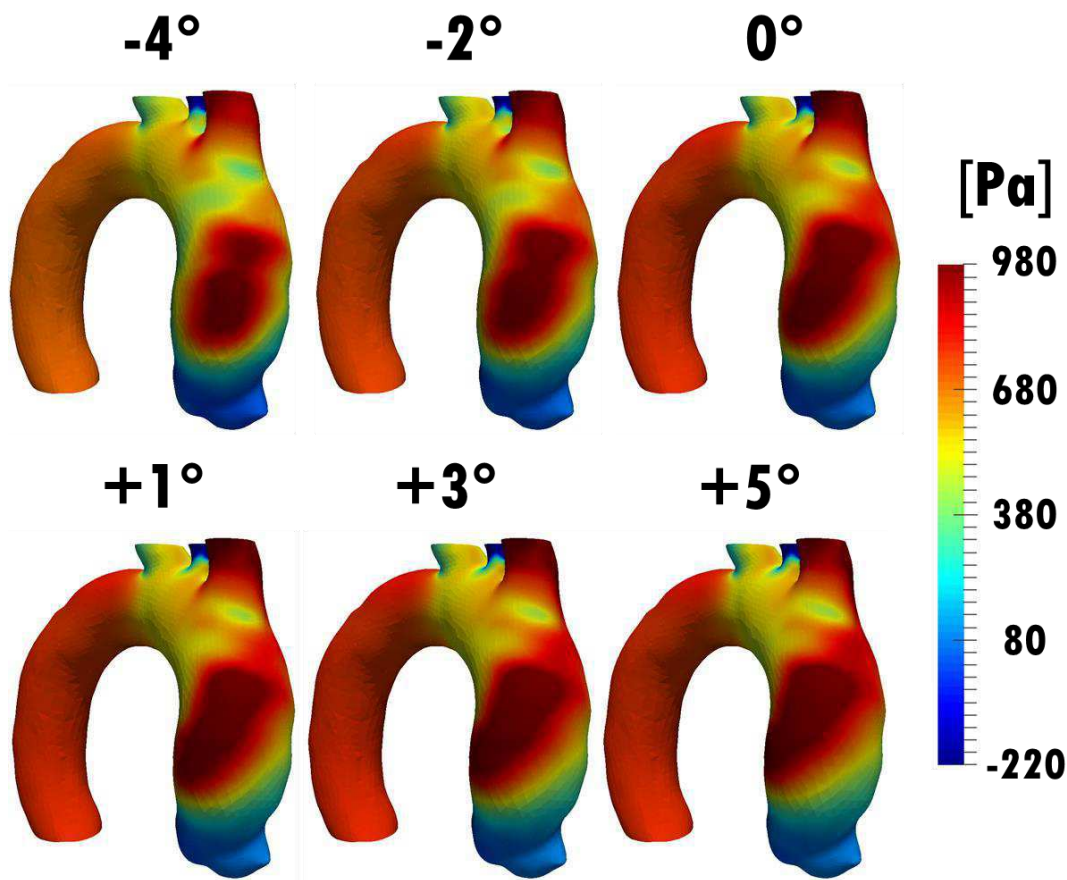


Figure 4.34 – Percentage of high WSS values on the right anterolateral wall of the ascending aorta varying with the tilt angle

#### 4.4.6. Pressure on the Aortic Wall

The effect of the pressure on the aortic wall is examined employing a similar approach as carried on with the WSS analysis. Initially, the complete geometry is analyzed, followed to a more focus analysis in a critical aorta region.

Figure 4.35 shows that the region where high pressure is found, corresponds to the region where the inlet jet impinges the aortic wall. It can be seen that higher pressures occur at the anterior zone for negative angles. As the angles increase and become positive, the high pressure region is displaced to the posterior zone.

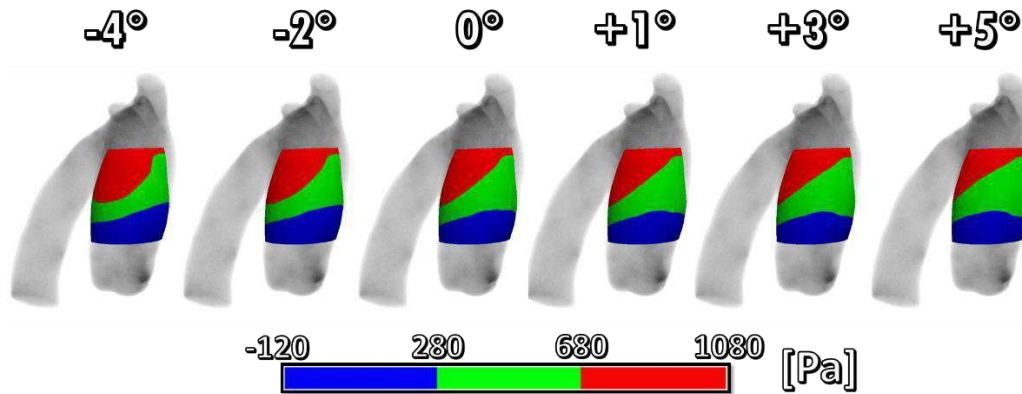


**Figure 4.35** - Influence of tilt valve angle on the pressure on the walls.  $Q=25\text{lt/min}$ .

Examining Fig. 4.35 with Fig. 4.29, one can observe that after impinging at the aortic wall, the blood flows along the upper part of the aorta, which is more perpendicular to the jet, causing an increase in the wall shear stress, and along the lower part (parallel to the jet) causing the reverse flow already mentioned.

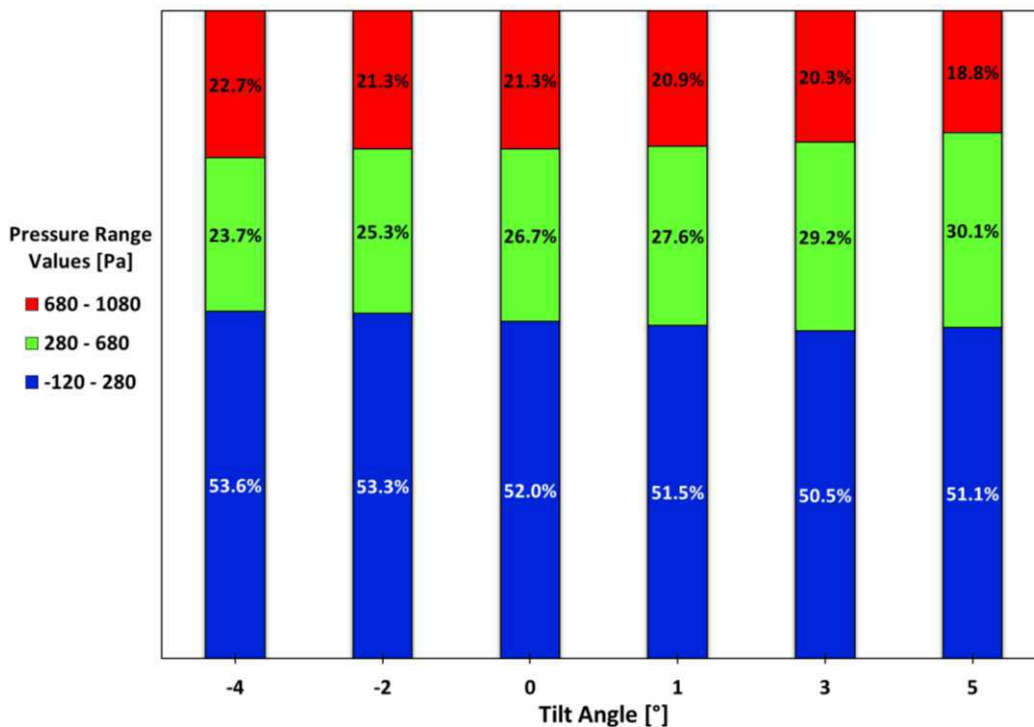
#### 4.4.6.1. Quantification of pressure on the walls

Figure 4.36 presents the pressure distribution divided in three pressure sub-ranges at the previously defined critical aortic wall region.



**Figure 4.36** - Pressure on the anterolateral wall varying with the tilt angle  $Q=25\text{lt/min}$

A small variation in the areas can be seen, which is best reflected in Figure 4.37 where a gradual increase of up to 6.4% of the region of intermediate pressures can be identified, as the jet takes positive angles. In turn, there is a decrease in the percentage of areas of high and low pressure, implying a more uniform distribution of pressure on the wall.



**Figure 4.37** - Percentage distribution of the pressure on the anterolateral wall of the ascending aorta varying with the tilt angle

Figure 4.38 shows the decrease in the percentage area of high pressure values, which has a value of 22.7% in the  $-4^\circ$  angle and has a progressive reduction until reaching a value of 18.8% in the angle of  $+5^\circ$ . The size of region of high pressure is less affected by the tilt angle and for the WSS.

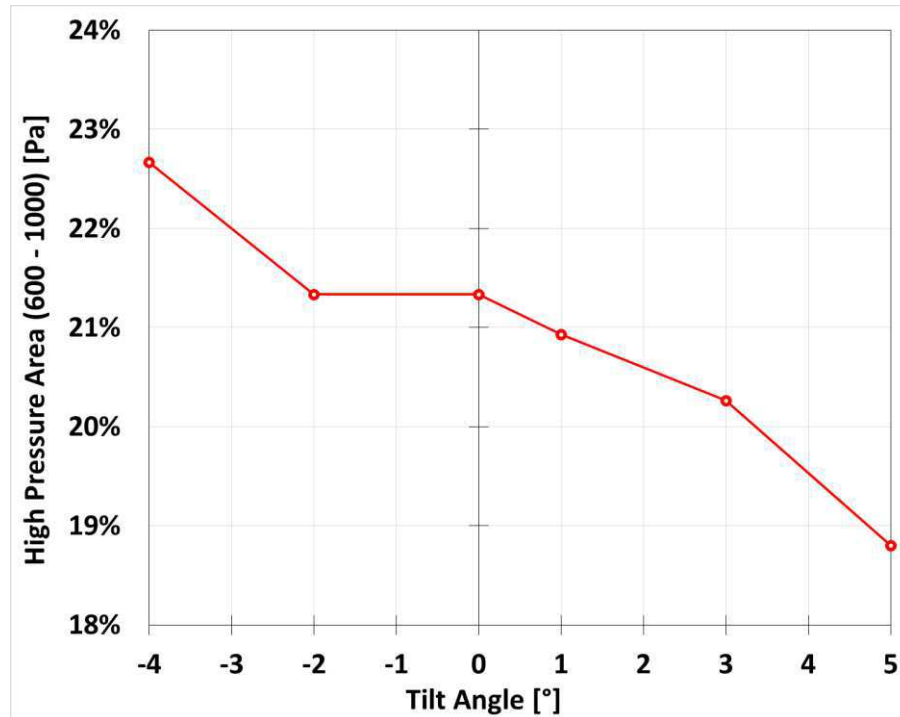


Figure 4.38 - Percentage of high pressure values on the right anterolateral wall of the ascending aorta varying with the tilt angle

#### 4.4.7. Profiles along the Z-axis

To aide in the evaluation of the effect of the tilt inlet valve angle in the flow field, the profile of several flow variables along the central z axis from the inlet until it reaches the aortic wall, is presented in this section. The Figure 4.39 illustrates the line in which these profiles were drawn.

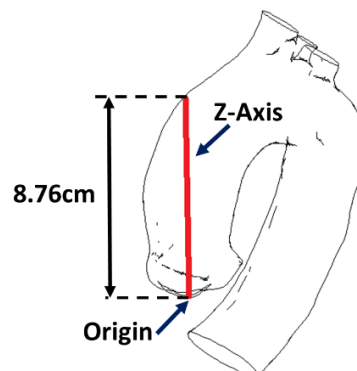
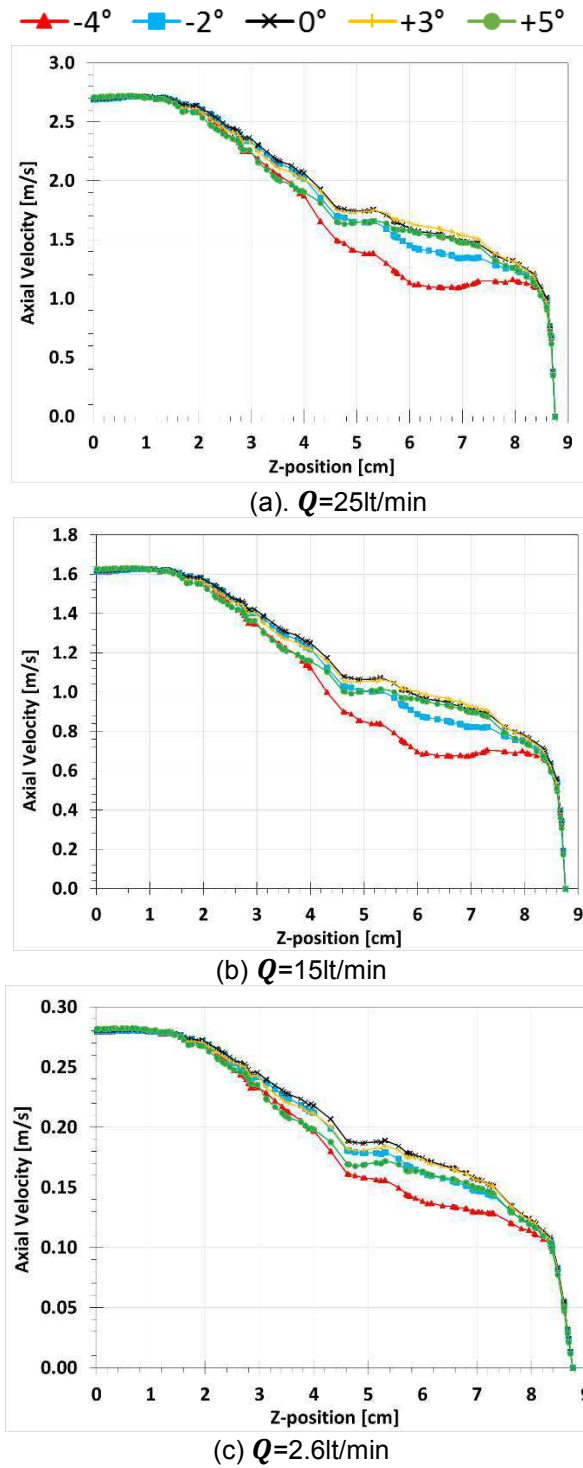


Figure 4.39 - Schematic diagram in which the profiles are plotted along the z axis

#### 4.4.7.1. Velocities components

The first parameter analyzed is the axial velocity, which is presented in the Figure 4.40 for three inlet flow rates ( $Q = 25$  lt/min; 15 lt/min and 2.6 lt/min).



**Figure 4.40** – Influence of tilt angle on the axial velocity along the z-axis.  $Q = 25$  lt/min; 15 lt/min and 2.6 lt/min.

Examining Fig. 4.40, it can be seen that the obtained variations show that near the entrance, up to two centimeters from the inlet, the axial velocity is approximately constant for all flow rates. After this point, there is a decrease of the axial velocity along the central axis due to the jet spread. Finally, due to the presence of the aortic wall, the velocity tends to zero, in a strong way. The velocity profile for the centered jet and the ones with positive inlet angle are very similar, and a slightly more accentuated reduction is observed for the negative inlet angle, particularly for  $-4^\circ$ . The qualitative behavior of the velocity distribution is the same for all flow rates. However, for the smaller flow rate, a more smooth variation can be observed after 5 cm from the inlet, as well as a wider boundary layer near the aortic wall.

Figure 4.41 presents the variation of the  $x$ - and  $y$ -velocity components along the  $z$ -axis. These components are responsible for directing the flow to the aortic wall, and spreading the jet. The positive  $y$  direction is to left and negative to the right, while the positive  $x$  is directed toward the paper and negative outward.

One interesting result shown in Fig.4.41 is the changing of sign of the  $x$ -velocity component and crossing of all  $y$ - profiles, for all angles and flow rates at the position equal to 5.2 cm, which corresponds to the point where the jet impinges the right aortic wall, forming a recirculation. The inlet tilt angle has little effect on the  $x$ -velocity. But, it is clear the effect of the inlet angle in  $y$ -velocity component, with its value directly related to the direction of the flow, as expected (Eq. 3.32). It can also be observed that when the inlet angle is positive, due to the aorta's curvature, there is a clear reduction on  $y$ -velocity value, since the flow must follow the aortic geometry, leading to a reverse flow upstream (at  $\approx 4$  cm).

For all inlet angles, with the exception of inlet angle equal to  $+5^\circ$ , near the upper part of the aortic wall, the  $y$ -velocity is negative; indicating that the jet has impinged the surface and it was reflected to the central region. Further analyzing Fig. 4.41, it can be noticed that, due to the aorta's top curve, the central axis encounter its surface, and a steep velocity reduction (up to zero at the surface) occurs. Once again, the qualitative profile of the  $y$ -velocity component is independent of the flow rate, with very similar profiles for the three cases investigated.

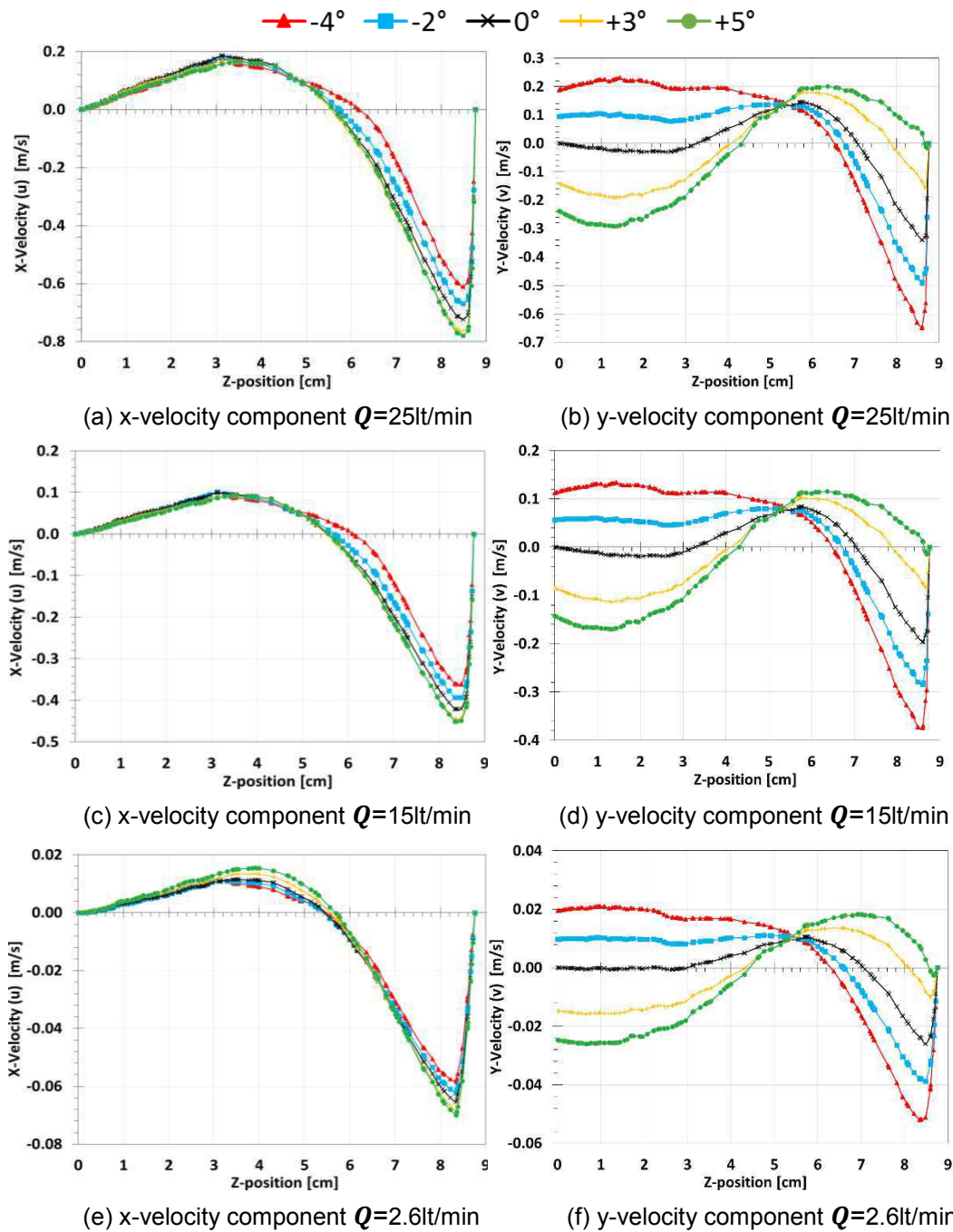
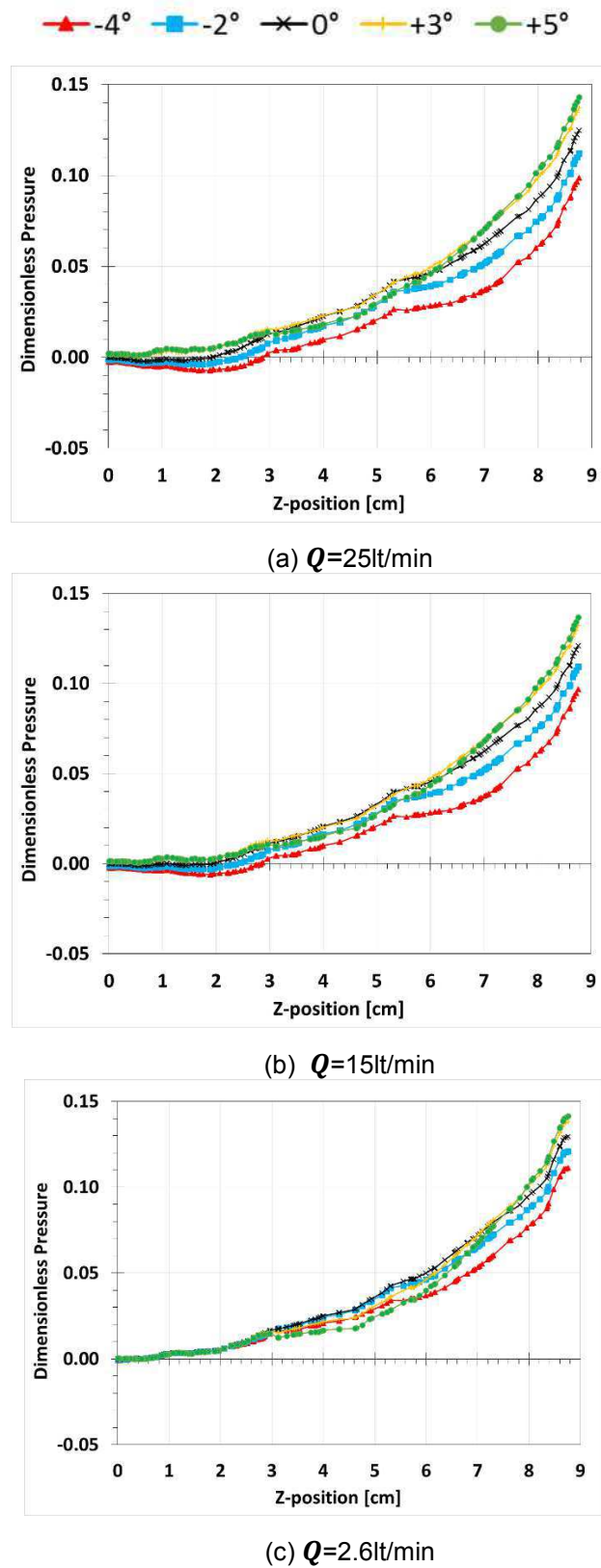


Figure 4.41 – x and y-velocities along z-axis.  $Q = 25 \text{ lt/min}$ ;  $15 \text{ lt/min}$  and  $2.6 \text{ lt/min}$ .

#### 4.4.7.2. Pressure

The profile of the dimensionless pressure, Eq. (4.1) along the central z-axis is shown in the Figures 4.42 for the selected three flow rates and five inlet angles. The pressure distribution is analogous for all cases (flow rates and inlet angles). At the impinging point at the aortic wall, the pressure is maximum; therefore, it increases along the z-axis, up to this point. Note that this increase is more

significant at positive inlet angle. The pressure variation is smaller for the  $-4^\circ$  inlet angle case, since, as shown in Fig. 4.40, for this case the z-velocity is smaller.



**Figure 4.42** – Dimensionless Pressure along z-axis.  $Q = 25 \text{ lt/min}$ ;  $15 \text{ lt/min}$  and  $2.6 \text{ lt/min}$

### 4.4.7.3. Turbulent Reynolds Stress

The turbulent Reynolds stress components distribution along the z-axis are evaluated in this section. First, the turbulent intensity is presented in the Figure 4.43.

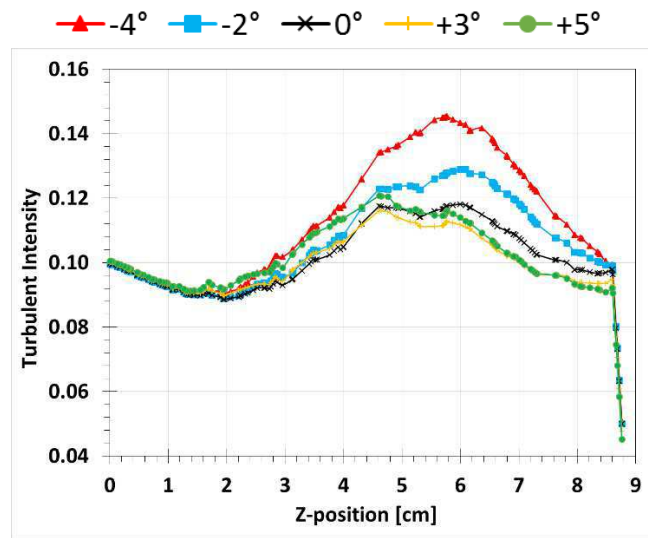
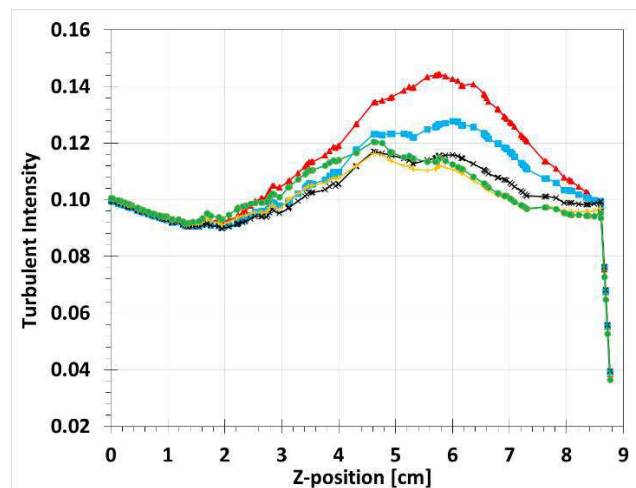
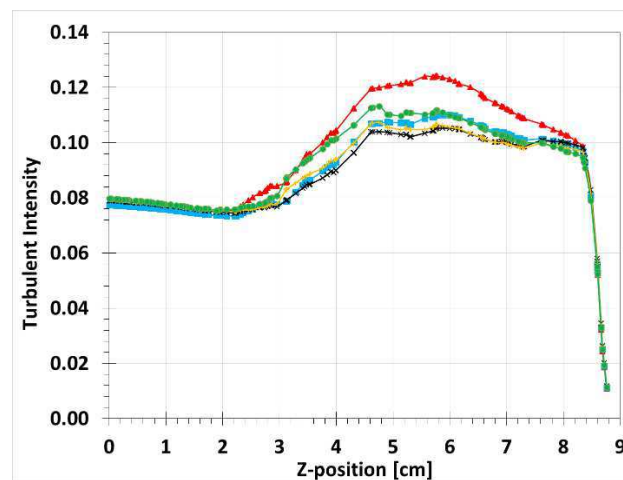
The turbulence intensity is directly proportional to the turbulent kinetic energy, Eq. 4.7, which is a measure of the turbulence characteristic velocity, and combines all three normal Reynolds stress components. Fig. 4.43 shows that the negative inlet angles have a significant influence, since they increase the values of turbulent intensity in the region between 4cm and 7cm. On the other hand, the positive angles do not present a remarkable variation with respect to the central position. This increase in negative angles is a little more pronounced as velocity increases. As expected, the turbulent intensity goes to zero at the aortic wall.

Figure 4.44 illustrates the profile along the z-axis of the dimensionless shear Reynolds stress,  $\tau_{t,yz}^*$  (Eq.4.4), for the five inlet angles and three flow rates. Near the inlet jet, the shear stress is practically null. For the negative tilt angles and aligned jet case,  $\tau_{t,yz}^*$  increases in the negative direction up to 5.2 cm (near wall region), reducing its magnitude to zero at the aortic wall. For positive tilt angles, after the initial inlet region with no shear stress, a slight increase of  $\tau_{t,yz}^*$  can be observe. At the upper aortic wall region (when the z-axis reaches the aortic wall), the Reynolds shear stress is equivalent for all cases and flow rates.

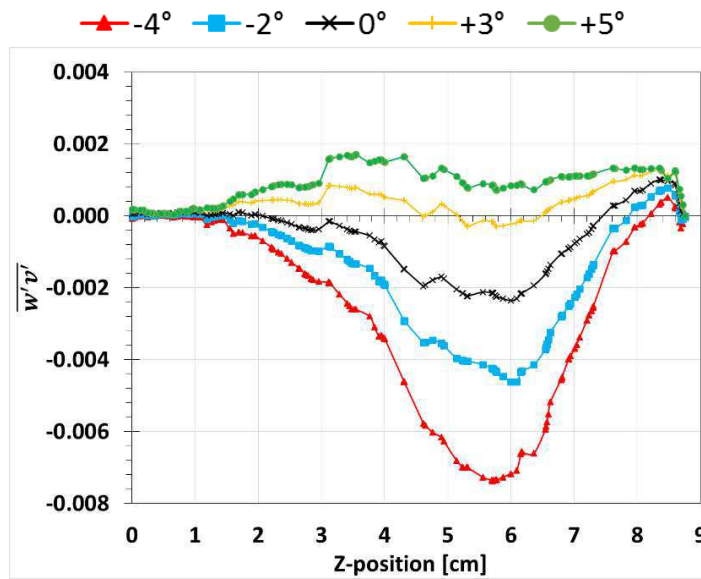
The three components of the dimensionless deviatoric part of the normal Reynolds stress  $\overline{U'U'}$ ;  $\overline{V'V'}$  and  $\overline{W'W'}$  (Eqs. 4.5 and 4.6) are presented in Fig. 4.45. Note that very low values were also obtained for the three components Reynolds stress near the inlet jet, characterizing the region where the jet behaves as a potential flow. The large differences observed in the normal Reynolds stress components are a clear indication of the strong anisotropy of the flow. As already observed, the influence of the flow rate is very small and all normal Reynolds stress are similar.

Analyzing Figure 4.45, one can see that  $\overline{U'U'}$  presents a similar profile along the z-axis for all inlet tilt angles. From the positive to the negative, the variations

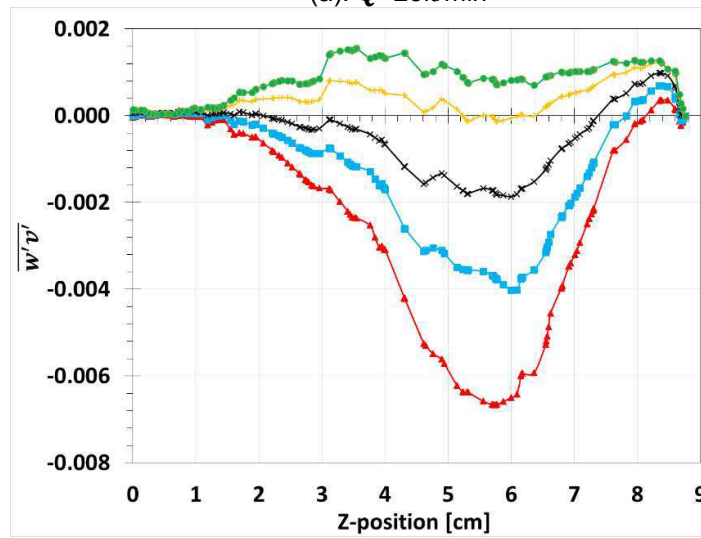
are more accentuated. This occurs, due to the curvature of the aortic wall, i.e., a positive inlet tilt angle, tends to align the jet with the geometry.

(a).  $Q=25\text{lt/min}$ (b)  $Q=15\text{lt/min}$ (c)  $Q=2.6\text{lt/min}$ 

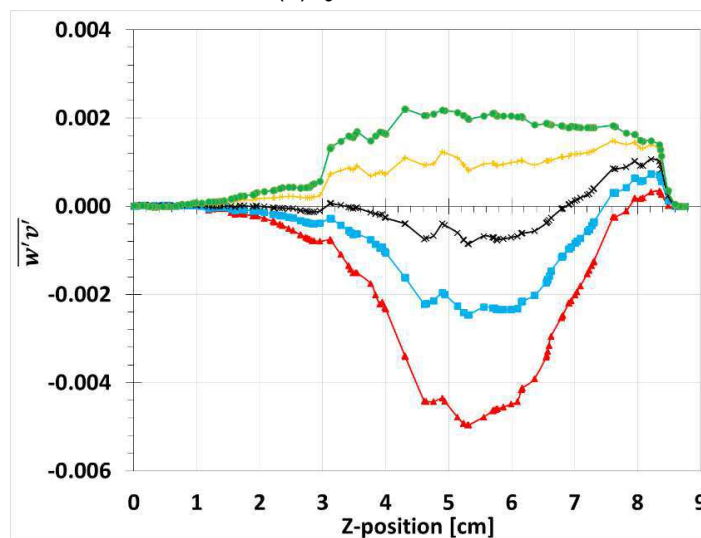
**Figure 4.43** – Turbulent intensity in the Z-axis.  $Q = 25 \text{ lt/min}$ ;  $15 \text{ lt/min}$  and  $2.6 \text{ lt/min}$



(a)  $Q=25\text{lt/min}$



(b)  $Q=15\text{lt/min}$



(c)  $Q=2.6\text{lt/min}$

**Figure 4.44** – Dimensionless shear Reynolds stress,  $\tau_{t_{yz}}^*$  in the Z-axis.  $Q = 25 \text{ lt/min}$ ;  $15 \text{ lt/min}$  and  $2.6 \text{ lt/min}$ .

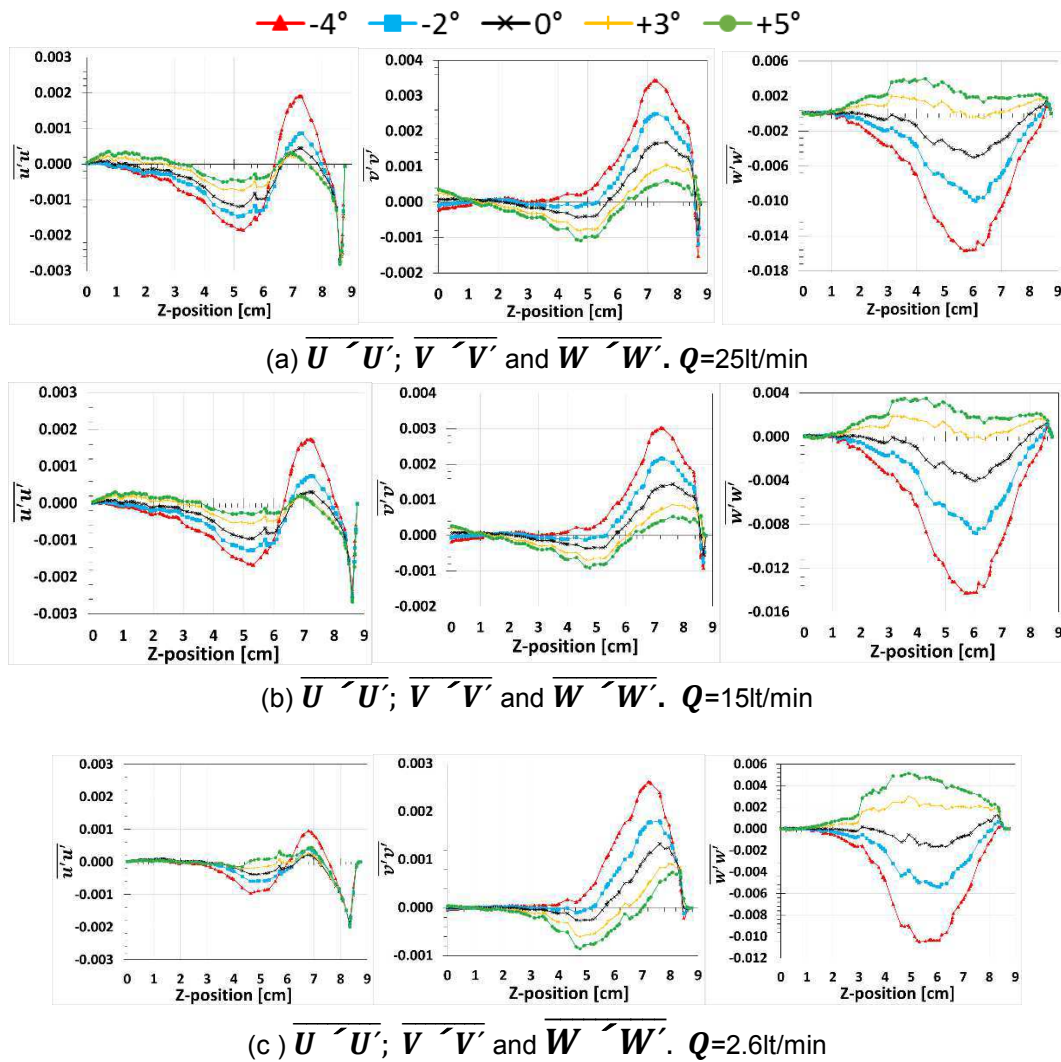


**Figure 4.45** – Profile of dimensionless deviatoric normal Reynolds stress along the Z-axis.

$Q = 25 \text{ lt/min}$ ;  $15 \text{ lt/min}$  and  $2.6 \text{ lt/min}$ .

Analyzing the profile of  $\overline{V'V'}$  along the  $z$ -axis, in Figure 4.45, it is observed that for negative inlet angle, the  $y$  component of the normal Reynolds stress starts increasing at 4 cm from the inlet, it reaches a maximum value and decreases sharply as the line approaches the aortic wall. The positive inlet angle cases and central case show a decrease on the normal component  $\overline{V'V'}$ , before also increasing its value, in a similar way as the negative angles cases, but with smaller intensity. Due to the curvature of the aorta, an increase in the normal  $y$  Reynolds stress is induced. However, this increase is reduced when the inlet jet is directed in the opposite direction as the aorta's curvature, since the flow has to adjust to the geometry. The same pattern exists between the different flow rates, although once again the phenomenon is more pronounced at higher flow rates.

The profile of  $\overline{W'W'}$  is quite different from the other two normal components.

Note that its profile is very similar to the shear stress profile, indicating that the  $z$ -fluctuation (present in both terms) is dominant. At the lowest flow rate (2.6 lt/min) there is a certain symmetry, where the negative angles adopt opposite values in relation to the positive angles, besides having a magnitude a little higher. A more significant variation of its magnitude can be observed for the higher flow rates cases. Further, the cases of negative angles have values even further away from the central position.

#### **4.4.8. Conclusions**

From the results show, it was observed that the tilt angle of the prosthetic valve induces changes in the hemodynamic patterns of the aorta. However, in all cases, the jet tends to impact the right lateral wall of the ascending aorta. Negative tilt angles incline the jet towards the anterior wall, without a substantial modification of the jet diameter with respect to the values of the central position. This change concentrates the pressure, the Reynolds stress and the WSS on this wall, increasing its mechanical stress, in addition to increasing Reynolds stress and recirculation values on the right side of the jet.

As the prosthetic valve takes positive angulation, the jet tilts toward the posterior wall, with a small widening of the jet diameter, this angle variation relieves the mechanical stress on the anterior wall of the ascending aorta, decreasing and displacing the high pressure and high WSS values. In addition, the Reynolds stress and recirculation values increase to the left of the jet.

Analyzing the variations that occurred in the central axis it was possible to quantify and analyze the influence of angulation on the different hemodynamic properties. First, it is remarkable that the variations of the properties have a certain pattern at all velocities of the pulsatile cycle; however, these variations are a little higher at high velocities.

Along the  $z$ -axis as the jet takes negative angles the axial velocity decreases after the two first centimeters of ascending aorta. Also, the  $y$ -component of the velocity starts with positive values and they decrease as the jet advances. There are a point of convergence of all cases at approximately 5.2cm when the jet impact for first time with the right wall of the aorta. For the negative angles cases, as the jet advances there are a gradual increase in pressure, which is lower as the jet is tilted

more toward the anterior wall. The negative angles have a significant influence in turbulent intensity, since they increase the values of turbulent intensity in the region between 4 and 7cm. Finally, the negative angles have a more important influence in the Reynolds stresses  $\overline{U'U'}$ ;  $\overline{V'V'}$ ;  $\overline{W'W'}$  than the positive angles.

The changes generated in the axial velocity by positive angles are much less significant. In addition, the  $y$ -component of the velocity starts with negative values and they increase as the jet advances, and converge when the jet impinges for the first time the aortic wall, at approximately 5.2 cm from the inlet. For positive inlet angles, as the jet advances there are a gradual increase in pressure, which is higher as the jet is tilted more toward the posterior wall. The positive angles do not present a remarkable variation of turbulent intensity with respect to the central position. By last, the positive angles have less influence in the Reynolds stresses  $\overline{U'U'}$ ;  $\overline{V'V'}$  and  $\overline{W'W'}$  than the negative angles, but they tend to have a certain symmetry with respect to the negative angles.

#### **4.5. Influence of Turbulent Intensity on Blood Flow**

From the previous analysis, it was observed that the inlet tilt angle has a strong influence in the turbulence intensity distribution. The results were obtained by imposing an inlet turbulent intensity of 0.1, based on the experiment performed by Azevedo (2017). This parameter is very sensitive to the aortic valve shape. Therefore, at the present section, its influence on the flow field in the interior of the aorta is examined. Four cases are compared, by imposing the inlet turbulent intensity values equal to 0.1; 0.3; 0.5 and 0.7. Two representative flow rates in the pulsatile cycle (25 lt/min and 5.3 lt/min) were considered, and the inlet jet was maintained centered (no inclination).

##### **4.5.1. Axial Velocity**

Figure 4.46 shows pathlines throughout the geometry, where it can be seen that the variation of the turbulent intensity leads to quite important changes in the aortic hemodynamics, as the jet expands considerably as the turbulent intensity increases. The initial region of impact of the jet descends and expands; and

furthermore a displacement of the vortices and recirculation zones is present.

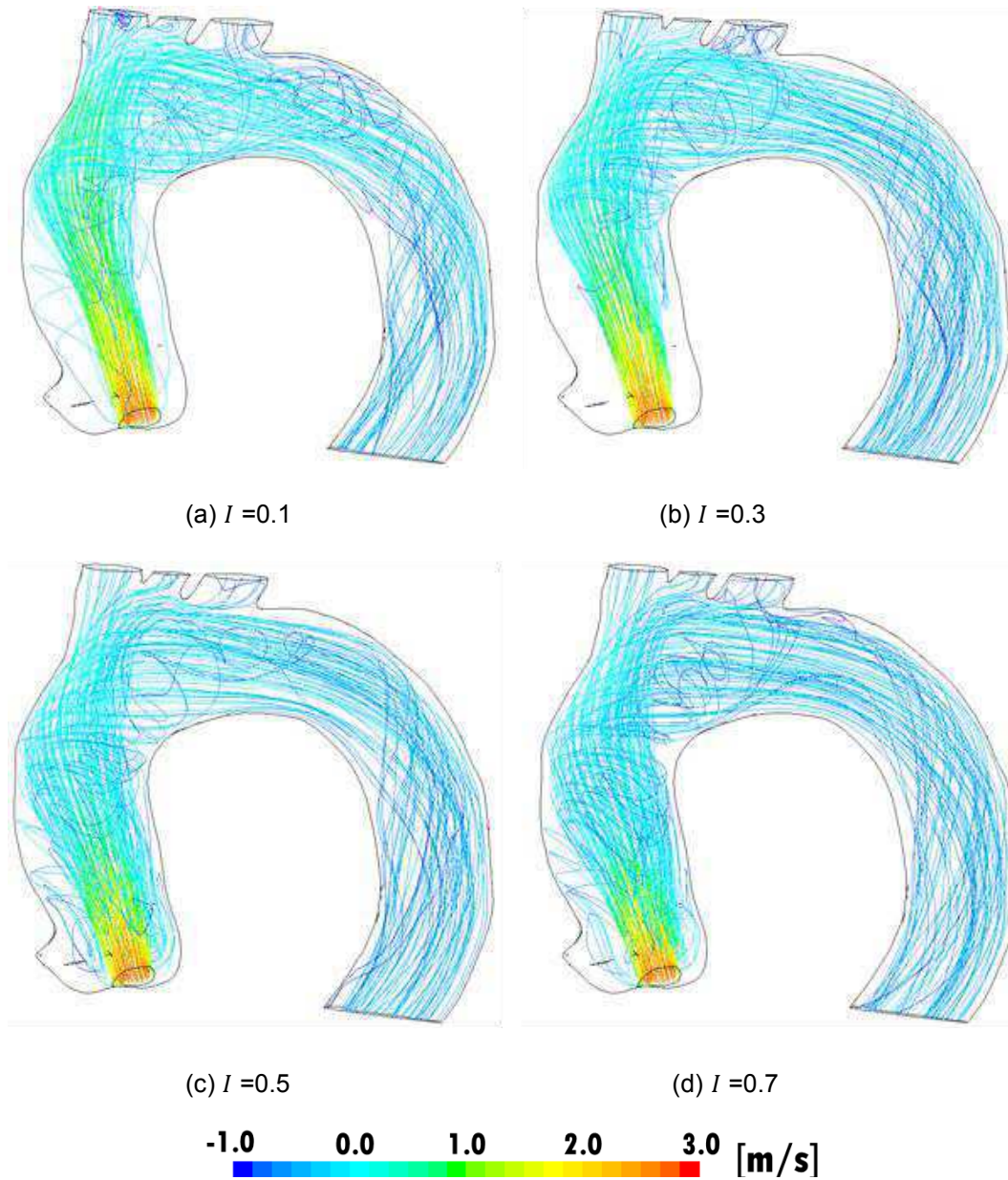


**Figure 4.46** - Pathlines varying with the turbulent intensity.  $Q=25\text{lt/min}$ .

Figures 4.47 and 4.48 present isocontours of the axial velocity in the central plane, for the high and low flow rate, respectively. The widening of the inlet jet can be clearly seen, especially for the higher flow rate ( $Q=25\text{ lt/min}$ ) case. A characteristic of turbulent flow is the enhancement of diffusion, incrementing the mixture of the flow. Therefore, as the turbulence intensity increases, the diffusion also increases leading to a wider spread of the inlet jet.

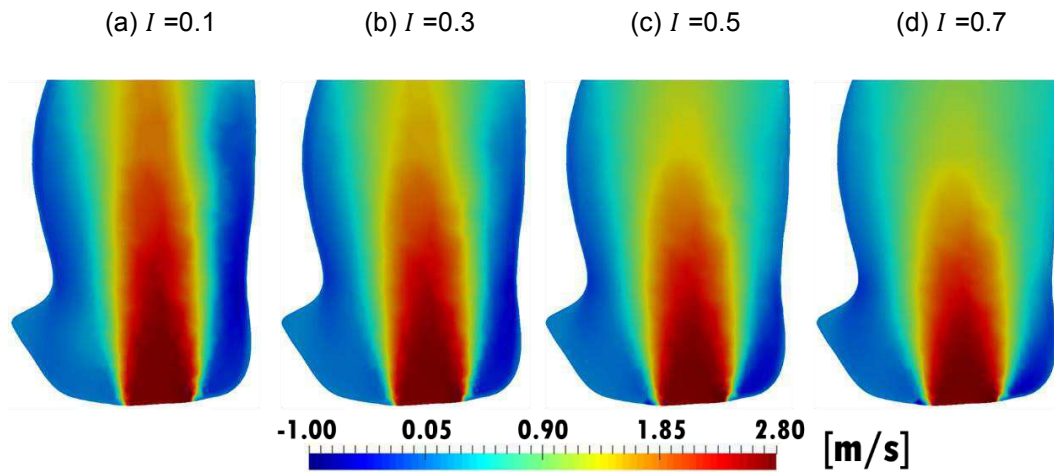


**Figure 4.47** – Influence of inlet turbulent intensity at axial velocity fields.  $Q=25\text{lt/min}$

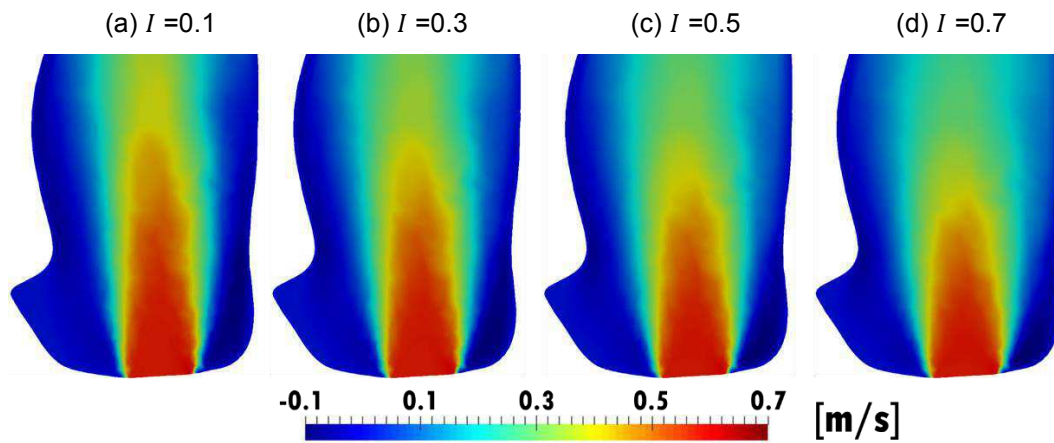


**Figure 4.48** – Influence of inlet turbulent intensity at axial velocity fields.  $Q=5.3\text{ lt/min}$

#### 4.5.2. Pressure

Figure 4.49 presents iso-contours of pressure at the central plane for  $Q=25\text{lt/min}$ . The figure shows that by increasing the turbulent intensity greater pressure variation is generated. As the inlet jet gets larger, recirculations near the inlet valve are intensified, inducing a pressure reduction in this region. Further, a small increase of the pressure at the top region is also observed.

In order to compare the results between the two velocities analyzed, the iso-contours of the dimensionless pressure is presented in Fig. 4.50. The variations found in the previous analysis remain similar, indicating that the flow rate does not have a significant impact on the pressure distribution, only on its absolute value.

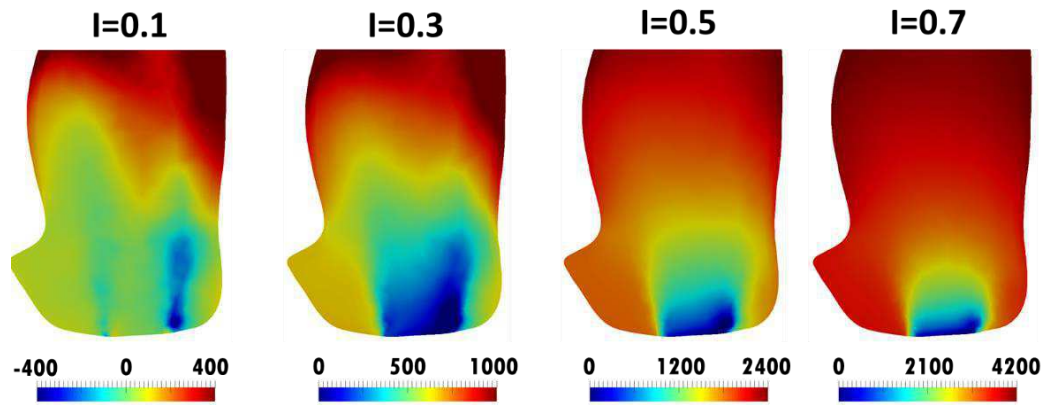


Figure 4.49 - Influence of inlet turbulent intensity on the pressure fields.  $Q=25\text{lt/min}$

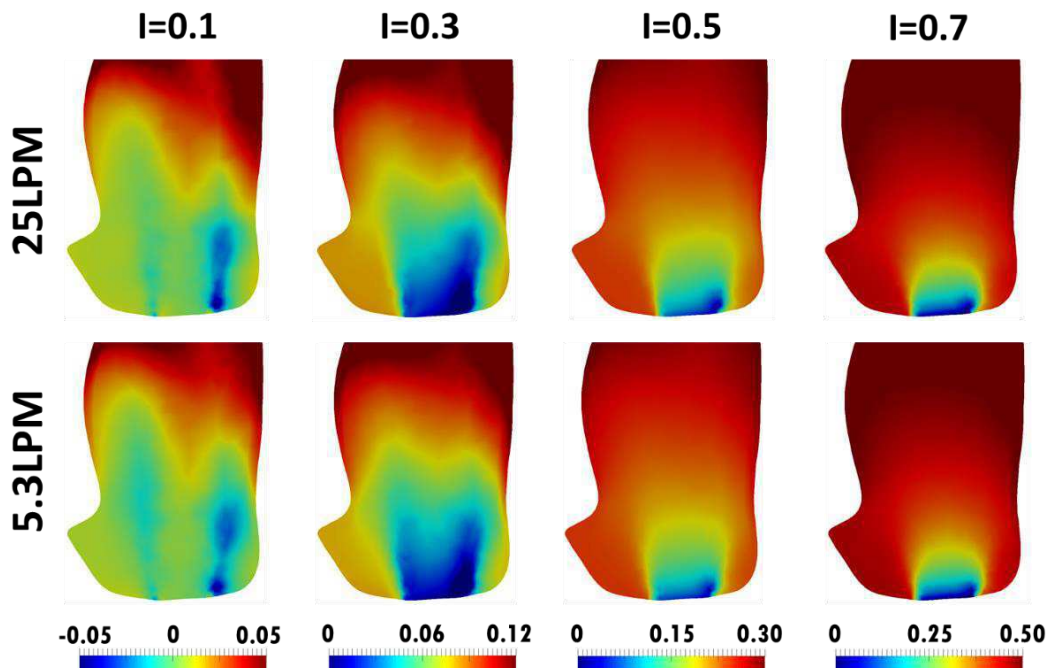
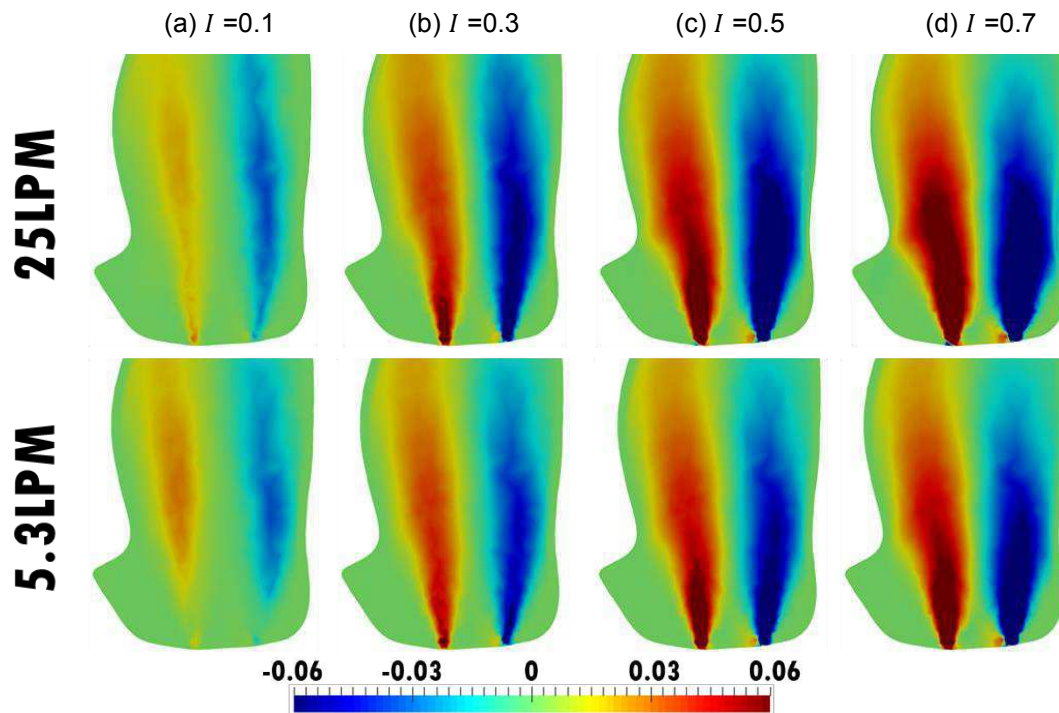


Figure 4.50 – Comparison of dimensionless pressure fields varying with turbulent intensity for two flow rates,  $Q=25\text{lt/min}$  and  $Q=5.3\text{ lt/min}$ .

#### 4.5.3. Dimensionless Shear Reynolds Stress

The dimensionless shear Reynolds stress distribution at the central plane is shown in Figure 4.51, for the four inlet turbulent intensity and two flow rates. A certain symmetry is preserved in each case and an increase in the shear Reynolds stress is observed as the turbulent intensity. This behavior is expected, since greater turbulent intensity implies in stronger turbulence and consequently larger turbulent flux (or turbulent shear). As already mentioned, an increase in the turbulence

induces more diffusion, which explains in part the widening of the diameter of the jet, previously shown.



**Figure 4.51** - Influence of inlet turbulent intensity on the dimensionless shear Reynolds stress.  $Q=25\text{lt/min}$  and  $Q=5.3\text{ lt/min}$

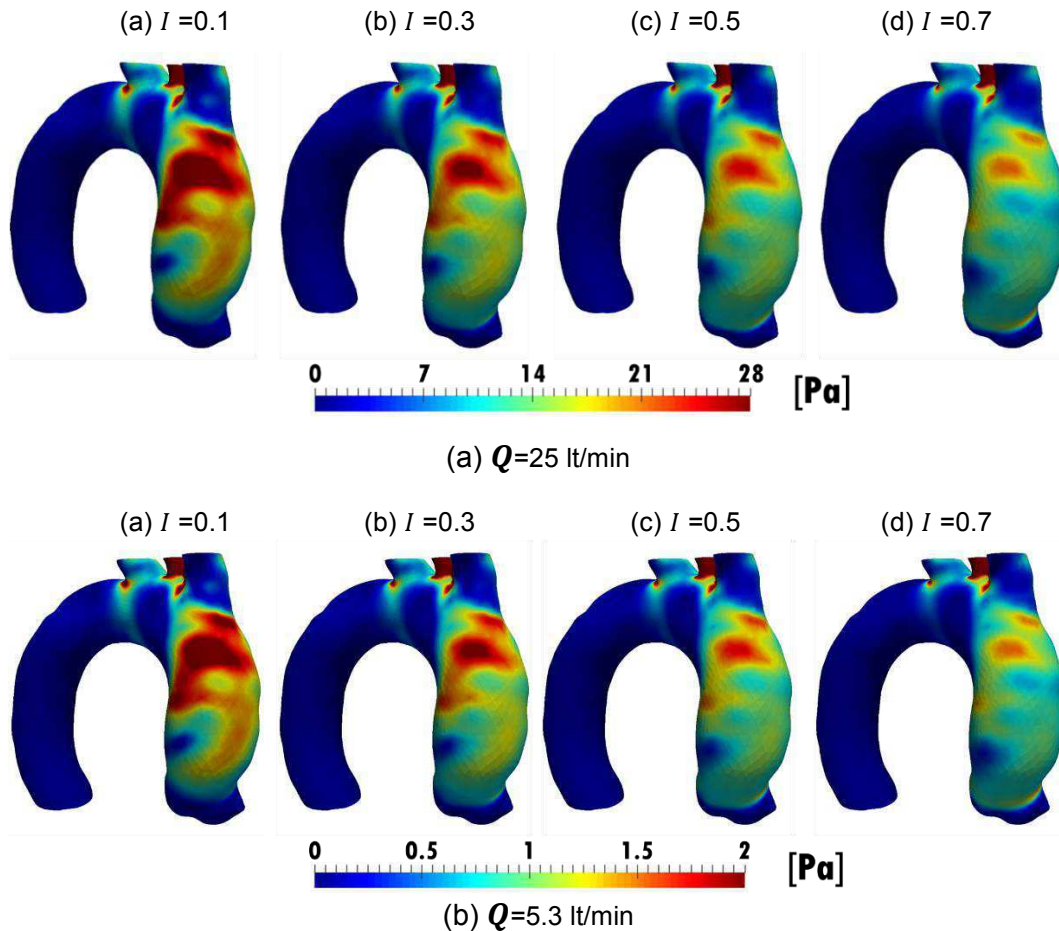
#### 4.5.4. Wall Shear Stress - WSS

Figure 4.52 illustrates the wall shear stress, WSS, distribution at the aortic wall, for both rates and all inlet turbulent intensity. Here it is remarkable a large decrease of WSS in the whole area as the turbulent intensity increases, which results in a considerable decrease of the mechanical stress on all the walls of the ascending aorta.

To quantify the percentage of area of interest subject to high shear, a quantitative analysis similar to the tilt angle case was performed for the flow rate of 25 lt/min, for the different inlet turbulent intensity and it is shown in Figure 4.53 and 4.54.

In this case, as illustrates the Figures 4.53 and 4.54, the high WSS area disappears when the inlet turbulent intensity is equal to 0.5, and a reduction of the area of intermediate values is observed. In the last case, with the highest turbulent intensity,  $I=0.7$ , the values of low WSS comprise almost the whole zone, covering up to 85.2% of it.

Figure 4.55 shows the progressive decrease of the high-WSS zone until it disappears and Figure 4.56 shows the percentage change in the area of intermediate values, with an increase when the turbulent intensity is 0.3 and then decreases as the inlet turbulent intensity increases.



**Figure 4.52** – Influence of inlet turbulence intensity at WSS.  $Q=25$ lt/min and  $Q=5.3$ lt/min

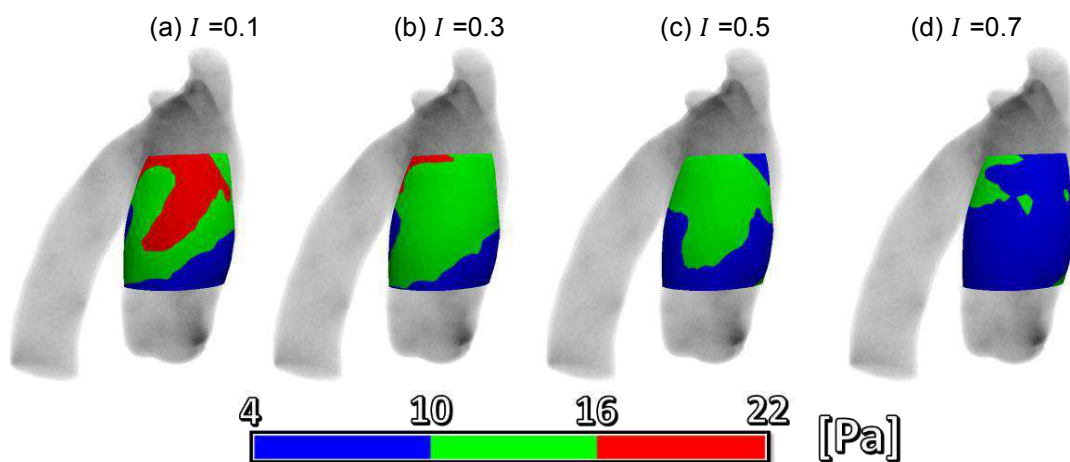


**Figure 4.53** – Identification of high WSS area at the aortic wall as a function of inlet turbulent intensity.  $Q=25$ lt/min.

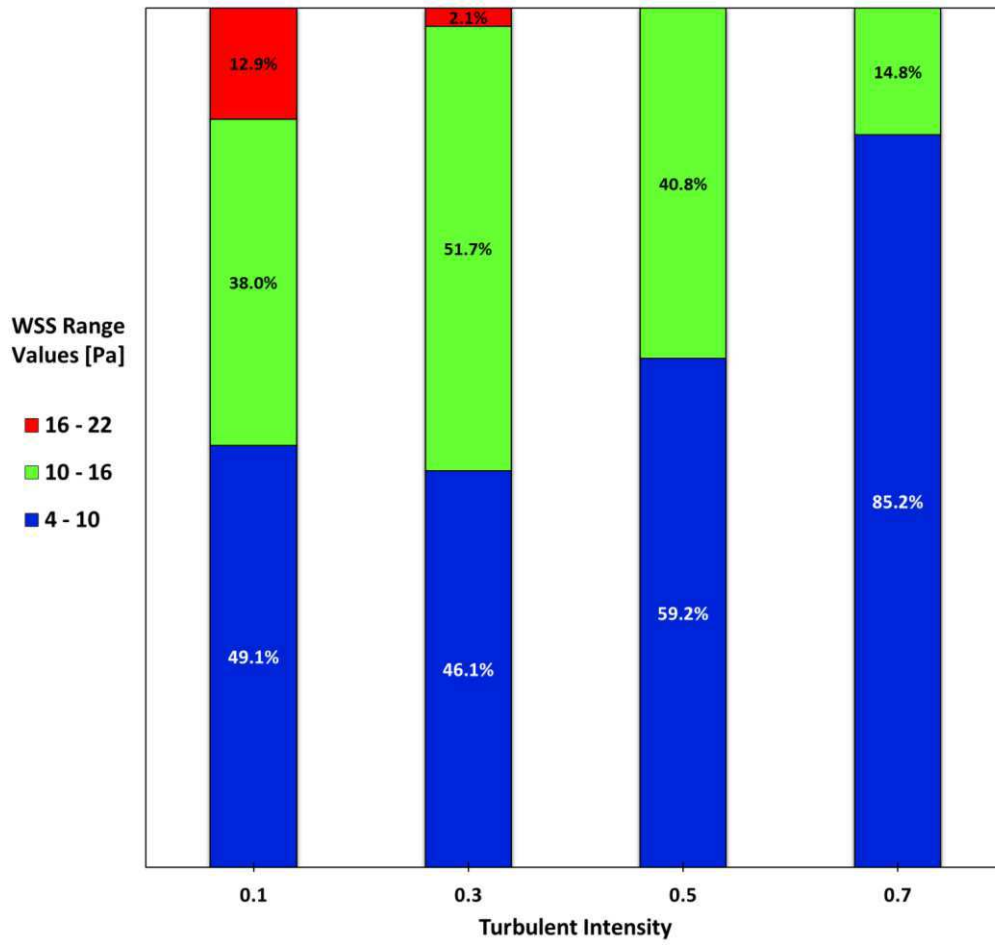


Figure 4.54 - Percent distribution of WSS on the anterior wall of the ascending aorta varying with the turbulent intensity

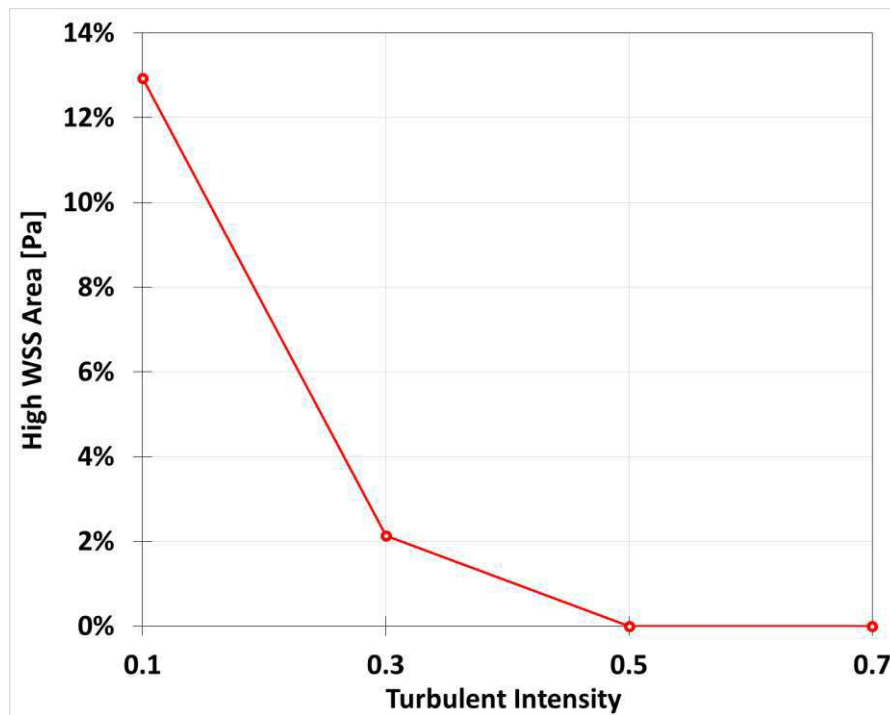
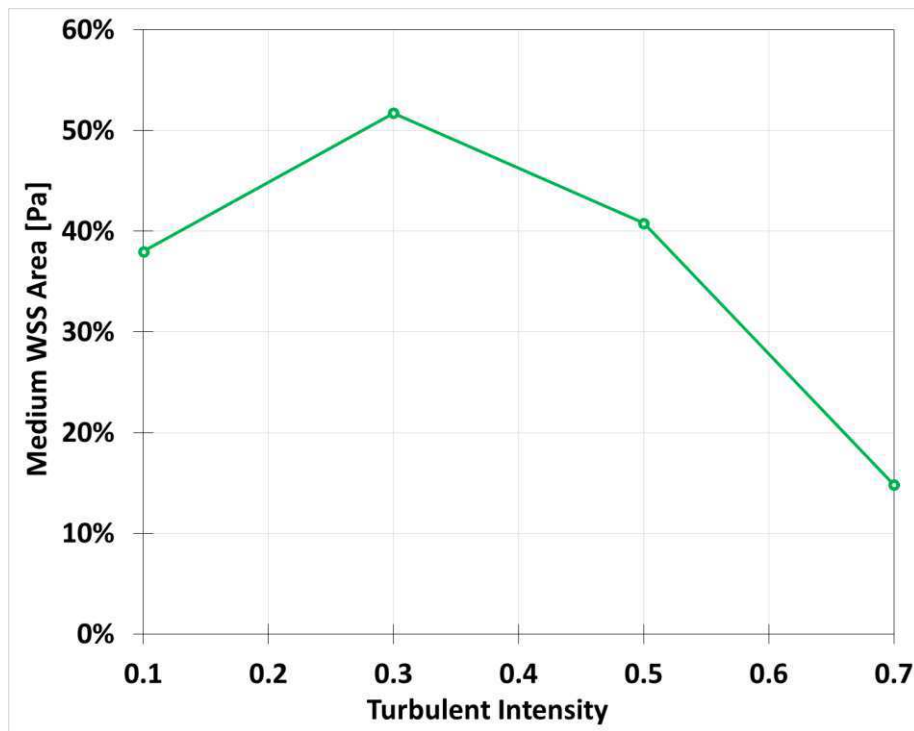


Figure 4.55 - Percentage of high WSS values on the anterior wall of the ascending aorta varying with the turbulent intensity



**Figure 4.56** - Percentage of intermediate WSS values on the anterior wall of the ascending aorta varying with the turbulent intensity

#### 4.5.5. Pressure on the Aortic Wall

The pressure distribution at the aortic wall was studied with two approaches. First, the modified pressure ( $\hat{p}$ ) is presented in Figure 4.57 (for both flow rates, and four inlet turbulent intensity). It can be seen that, as the turbulent intensity is increased, there is a considerable homogenization of the modified pressure acting on the walls, due to the spreading of the inlet jet. However, the pressure ( $p$ ), which is illustrated in the Figure 4.58, shows that although the homogenization is conserved, an increase in values is also present. This is because the pressure to be normalized in the input depends implicitly of the turbulent kinetic energy, which is a parameter that in turn is linked to the concept of the turbulent intensity as reflected by the equation 3.33.

Taking as sample the right anterolateral wall of the ascending aorta, the results presented in Figures 4.59 and 4.60 show a gradual increase of the intermediate values of modified pressure as the turbulent intensity increases, going from 21.9% to 35.2%.

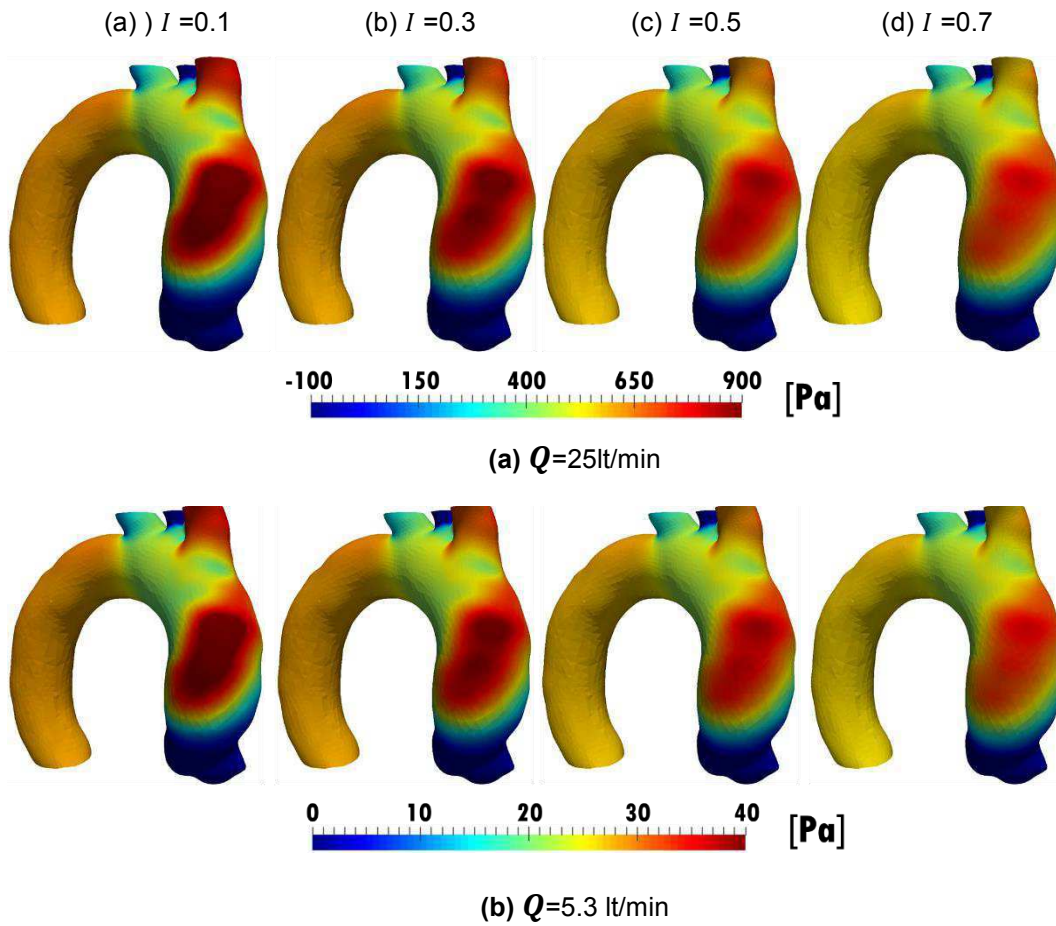


Figure 4.57 – Modified pressure ( $\hat{p}$ ) on the walls varying with the turbulent intensity.  $Q = 25 \text{ lt/min}$  and  $Q = 5.3 \text{ lt/min}$

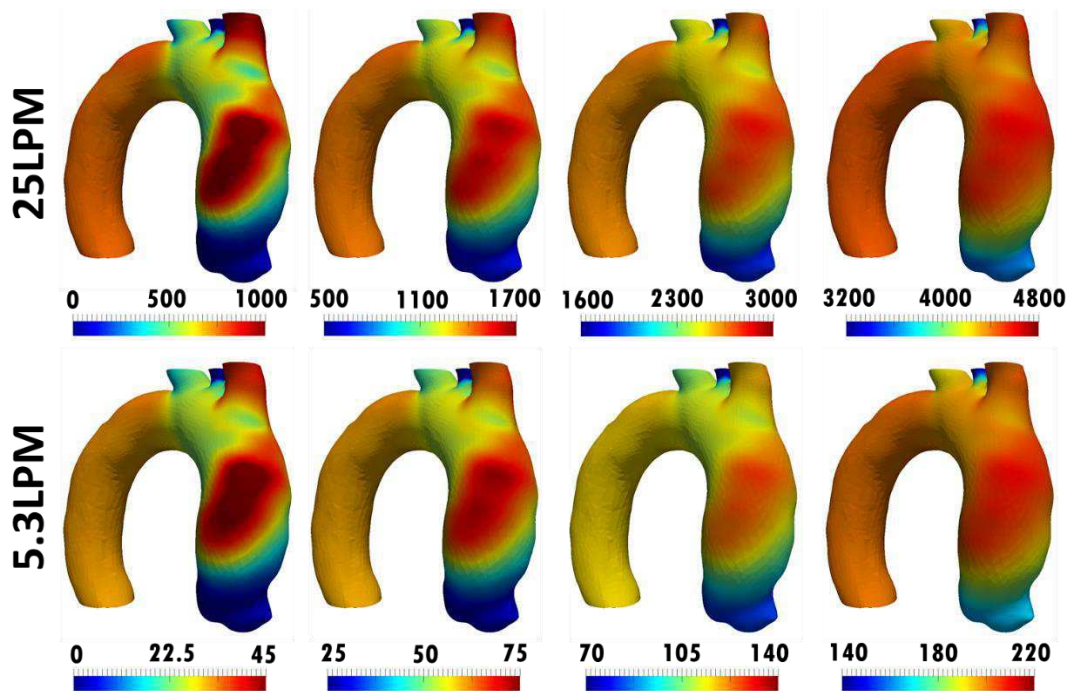
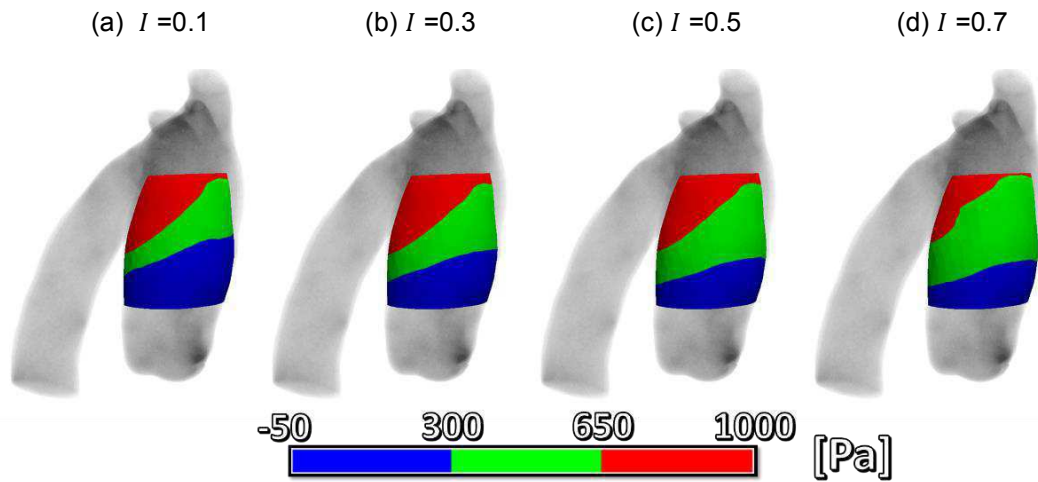
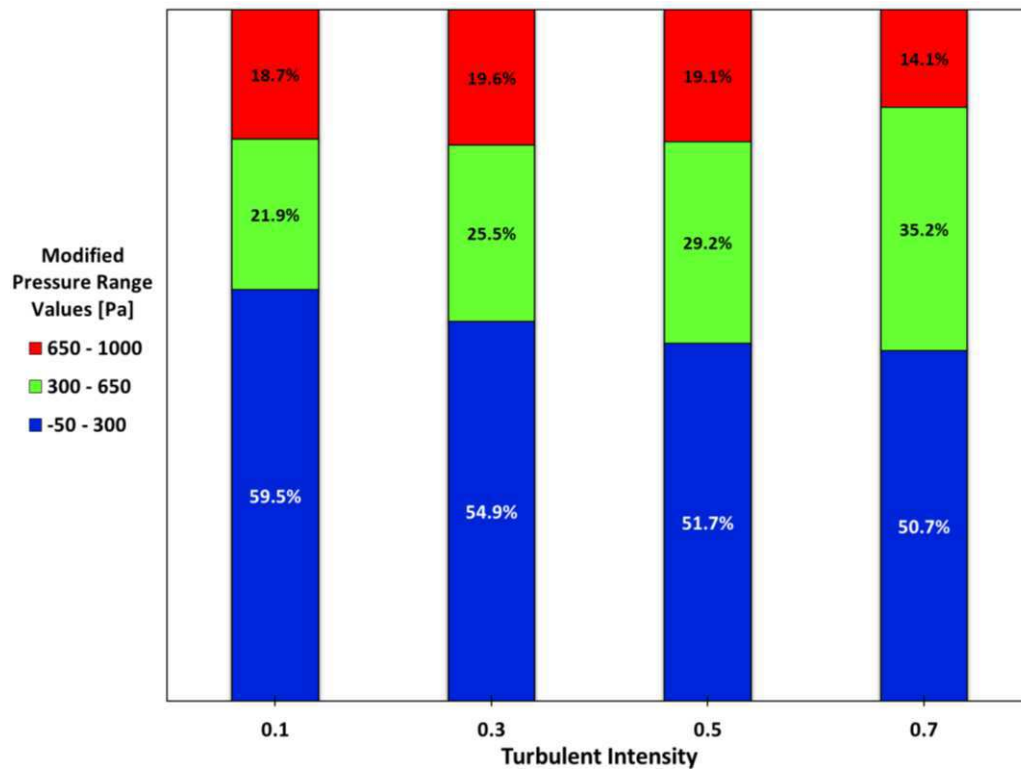


Figure 4.58 – Pressure ( $p$ ) on the walls varying with the turbulent intensity .  $Q = 25 \text{ lt/min}$  and  $Q = 5.3 \text{ lt/min}$



**Figure 4.59** – Identification of high modified pressure area at the aortic wall as a function of inlet turbulent intensity.  $Q=25\text{lt/min}$



**Figure 4.60** - Percent distribution of pressure on the anterior wall of the ascending aorta varying with the turbulent intensity

In addition, as shown in Figure 4.61, the high values of the modified pressure tend to remain constant for the three smaller inlet turbulent intensities, then decrease by 5% for the highest intensity case. Again a more uniform distribution of the modified pressure can be observed.

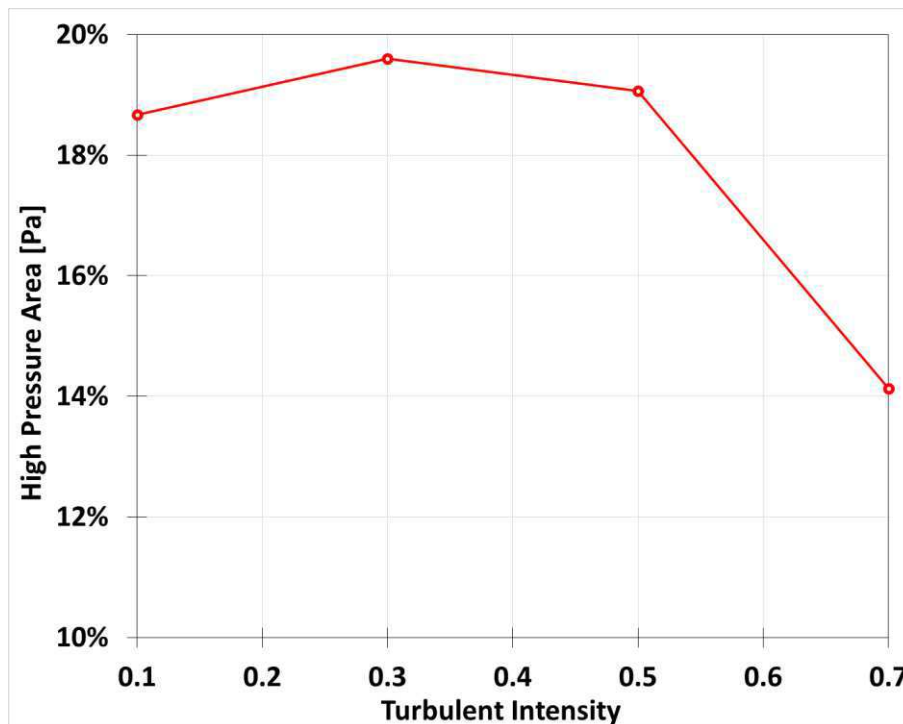


**Figure 4.61** - Percentage of high modified pressure values on the anterior wall of the ascending aorta varying with the turbulent intensity

#### 4.5.6. Profiles along the Z-axis

The variation of a few properties along the central z-axis (from the inlet until it reaches the aortic wall) is presented here, to evaluate the influence of the inlet turbulent intensity in the flow. The z-axis is oriented with respect to the jet in its central position.

The first parameter analyzed is the axial velocity, which is illustrated in the Figure 4.62. It can be noticed that as the turbulent intensity increases, a progressive decay of the values is generated, this occurs in both flow rates, each with a corresponding magnitude.

The dimensionless pressure is presented in Figure 4.63. As already discuss, the pressure increases along the z-axis, due to the high pressure at the impinging point. The effect of the higher inlet turbulent intensity is to enhance this variation, resulting in a much higher pressure variation from the impinging point of the aortic wall and the inlet valve. Note also, that higher inlet turbulent intensities (above 0.5) produce a larger increase of pressure near the entrance, changing the rate of growth, since higher turbulent imply in more momentum flux, and consequently large pressure variation. This behavior is maintained at both flows rates.

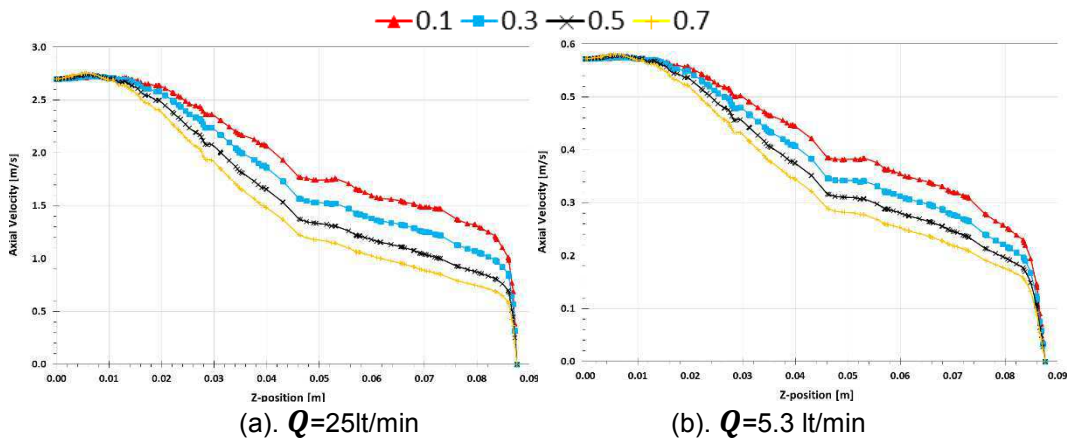


**Figure 4.62** – Influence of the inlet turbulent intensity on the axial velocity along the z-axis.  $Q=25\text{lt/min}$  and  $Q=5.3\text{lt/min}$

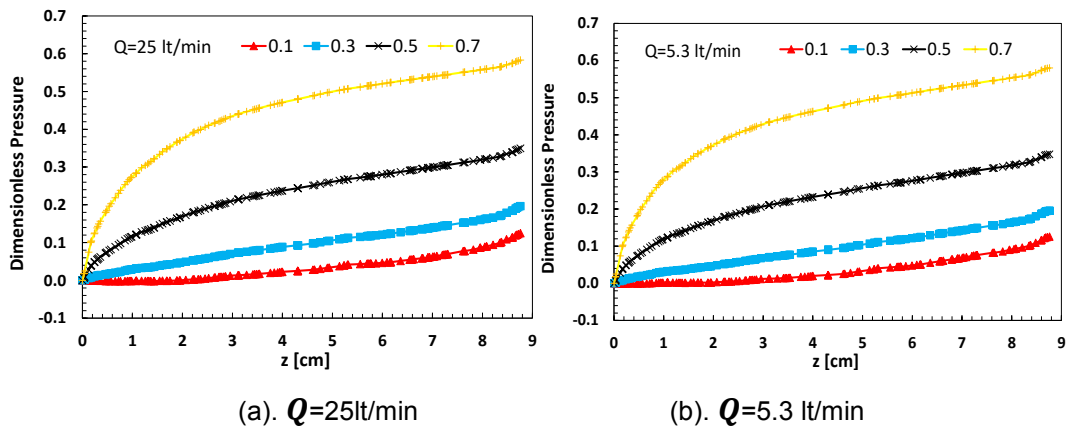


**Figure 4.63** – Influence of the inlet turbulent intensity on dimensionless pressure along the z-axis.  $Q=25\text{lt/min}$  and  $Q=5.3\text{lt/min}$

Figure 4.64 shows the variation of the turbulent intensity along the z-axis. From the prescribed value at the inlet for each case, it decays in a smooth way as the jet advances along the z-axis, until finally goes to zero at the aortic wall. Note that from approximately the position of 5.2 cm all curves are very close, indicating that the inlet condition has already diffused, and the presence of the aortic wall governs the flow. Once again, the flow rate does not present an impact in the solution.

The last parameter analyzed here is the dimensionless shear Reynolds stress  $\tau_{t_{ij}}^*$ , which is shown in Figure 4.65 for both flow rates ( $Q=25\text{lt/min}$  and  $Q=5.3\text{lt/min}$ ). Note that higher inlet turbulent intensity causes a higher shear Reynolds stress at the entrance. It decays along the jet development, until approximately 5.2 cm, when it starts increasing. Finally it decays to zero at the

aortic wall. A smaller variation and a vertical displacement of the drop in value of  $\tau_{ij}^*$  along the z-axis can be seen as the inlet turbulent intensity is reduced. Near the aortic wall, all results converge. A small dependence on the flow rate can be observed, which larger variation for the higher flow rate.

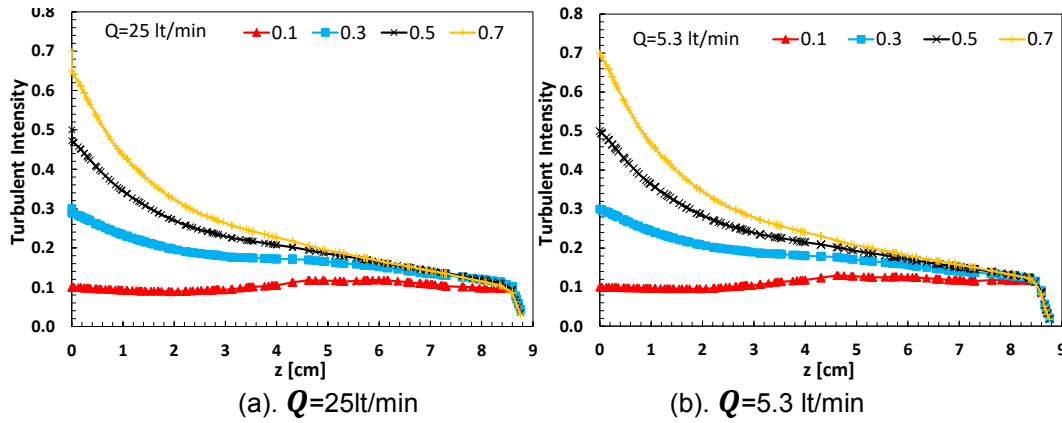


**Figure 4.64** – Influence of the inlet turbulent intensity on turbulent intensity along the z-axis.  $Q=25$ lt/min and  $Q=5.3$ lt/min

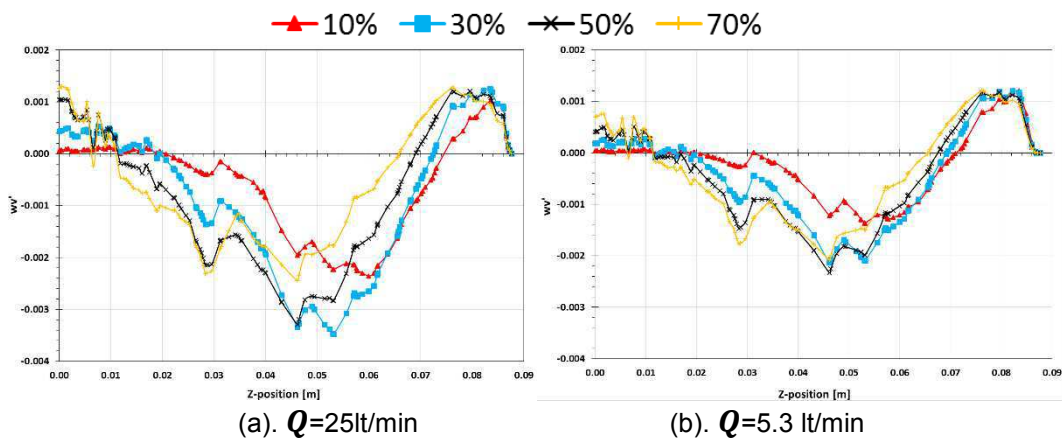


**Figure 4.65** – Influence of the inlet turbulent intensity on the dimensionless shear Reynolds stress along the z-axis.  $Q=25$ lt/min and  $Q=5.3$ lt/min

#### 4.5.7. Conclusions

The turbulent intensity has a rather significant influence on the hemodynamic properties of the aorta, greatly modifying the flow patterns. An increase in the turbulent intensity leads to a rapid spreading of the jet, which causes the impact on the walls to be distributed over a larger area, which reduces the concentration of high values of WSS and of modified pressure ( $\hat{p}$ ) in the ascending aorta wall. In

addition, the vortices and recirculation regions move to positions closer to the entrance.

Analyzing the properties in the z-axis it was possible to determine that the increase of the turbulent intensity leads to a decrease in the axial velocity, it causes an increase in the pressure at the aortic wall and intensifies the variation of the turbulent intensity. The Reynolds stresses presents a particular behavior, i.e., initially as the turbulent intensity is higher, the  $\tau_{tij}^*$  adopt higher magnitudes, however this behavior tends to be inverted from approximately 3.5cm for the cases of  $I = 0.5$  and  $0.7$  but remaining for the  $I = 0.3$  case. From this point, the highest values are adopted by the case of  $I = 0.3$  case, followed by the other 3 cases closely.

The flow rate did not present an impact in the solution, with a slightly larger influence on the dimensionless shear Reynolds stress.

## 5 FINAL REMARKS

This research work divided into three major fronts performed a numerical analysis of the blood flow in the ascending aorta. The 3D modeling of the geometry was obtained in a process that combines angiotomographic data with image segmentation of a particular patient. It should be noted that the definition of geometry in the aortic root is a complex process because it is literally continuous with the left ventricle, therefore a feedback process was performed in which this aspect of the geometry was improved twice until obtaining an appropriate result.

The present work was focus in the systole period, i.e., the flow rates investigated were intended to represent the flow at different stages of the period. Although, the transient actual flow was represented by a series of steady state, it was shown that the dimensionless flow distribution inside the aorta is weakly dependent on the flow rate.

The first study carried out was a comparison of the numerical prediction obtained in the present work with the experimental results of Azevedo (2017), who measured the velocity field in a model of the aorta of same patient geometry, based on the same 3D geometry. A qualitative good comparison was obtained for the variables considered. There were certain variations and displacements, which may be due to a slight variation in the reference system, like an inclination of the measurement planes, difficulty of defining precise angulation, the difference in the determination of the input geometry, uncertainties in the measurement and hydraulic pump vibrations.

Secondly, the main analysis of this research was carried out, in which it was sought to analyze the influence of small tilt angles of the inlet flow. The tilt angle of the prosthetic valve involves a substantial modification in the hemodynamic patterns of the aorta. It was concluded that negative tilt angles incline the jet towards the anterior wall, without a substantial modification of the jet diameter with respect to the values of the central position. This change concentrates the pressure, the Reynolds stress and the WSS on this wall, increasing its mechanical stress, in

addition to increasing Reynolds stress and recirculation values on the right side of the jet. As the prosthetic valve takes positive angulation, the jet tilts toward the posterior wall, with a small widening of the jet diameter. This angle variation relieves the mechanical stress on the anterior wall of the ascending aorta, decreasing and displacing the high pressure and high WSS values. In addition, the Reynolds stress and recirculation values increase to the left of the jet.

Along the central z-axis, it was observed that as the jet takes negative angles the axial velocity decreases after the two first centimeters of ascending aorta; the y-component of the velocity starts with positive values and they decrease as the jet advances; there are a gradual increase in pressure, which is lower as the jet is tilted toward the anterior wall. The negative angles have a significant influence in turbulent intensity, since they increase the values of turbulent intensity in the region between 4 and 7 cm. Finally, the negative angles have a more important influence in the Reynolds stresses  $wv'$ ,  $ww'$  and  $vv'$  than the positive angles.

The changes generated in the z-axis by positive angles in the axial velocity are much less significant. In addition, the y-component of the velocity starts with negative values and they increase as the jet advances. Also, there are a gradual increase in pressure, which is higher as the jet is tilted toward the posterior wall. The positive angles do not present a remarkable variation of turbulent intensity with respect to the central position and they have less influence in the Reynolds stresses  $wv'$ ,  $ww'$  and  $vv'$  than the negative angles, but they tend to have a certain symmetry with respect to the negative angles.

Since, it was observed that the inclination of the prosthetic valve has a significant impact on the hemodynamic properties of the aorta flow, it is proposed that this parameter should be carefully considered in future implementations of TAVR. One can also recommend that a customized hemodynamic study of the influence of the tilt angles of the prosthesis should be performed on each patient to be submitted to the procedure. It is known that each patient presents differences in their aortic geometry and in the aortic wall resistance, therefore such analyze should be personalized. The study could aide to promote an improvement in the implementation of TAVR, by recommending strategic adjustments in the positioning of the valve for each patient, which may reduce aortic remodeling and increase the durability of the prosthesis.

An analysis of the effect on the flow of the inlet turbulent intensity was also performed. It was found quite revealing results, i.e., it was observed that the turbulent intensity has a rather significant influence on the hemodynamic properties of the aorta, greatly modifying the flow patterns. An increase in the inlet turbulent intensity leads to a rapid spreading of the jet, which causes the impact on the walls to be distributed over a larger area, which reduces the concentration of high values of WSS. Although the wall pressure is higher with higher inlet turbulent intensities, it is slightly more uniform. In addition, the vortices and recirculation regions move to positions closer to the entrance.

Analyzing the properties in the z-axis it was possible to observe that due to the spread of the inlet jet, the axial velocity drop along the z-axis, from the inlet up to aortic wall is more pronounced. Further, high inlet turbulent intensity leads to a stronger pressure variation near the entrance, and a larger pressure difference between the inlet and aortic wall. The Reynolds stresses had a particular behavior, where it can be emphasized that in the initial centimeters these are higher when the turbulent intensity is higher

The latter results reveal that it may prove desirable to generate intentionally a turbulence at the inlet to decrease negative effects of WSS. This enhancement of the turbulent intensity can be achieved by modifying the designs of prosthetic valves, especially in the region of the cusps, where an improvement in the material and geometry can change this parameter for the benefit of patients. Care must be taken, with regard to the pressure, because although it is more uniform, it is higher at the aortic wall. It is recommended that further studies regarding the turbulent intensity must be performed, especially to identify possible side effects.

As a last comment, it can be remarked that this research has the potential in several aspects to generate subsequent works, where it will be possible to continue analyzing the influence on the flow of different additional parameters such as wall elasticity, transient flows (investigate the complete cycle of systole and diastole), blood constitutive equation, fatigue, process automation, etc. It is also recommended to evaluate the differences of the flow field before and after the TAVR procedure, as well as after a time interval of one or two years. All this in order to contribute to a research that can have a relevant impact on the future of medicine, bioengineering and human health.

## REFERENCE

BACH, D. S.; SIAO, D.; GIRARD, S. E.; DUVERNOY, C.; MCCALLISTER, B. D.; GUALANO, S. K. **Evaluation of Patients With Severe Symptomatic Aortic Stenosis Who Do Not Undergo Aortic Valve Replacement: The Potential Role of Subjectively Overestimated Operative Risk.** *Circulation: Cardiovascular Quality and Outcomes*, v. 2, n. 6, p. 533–539, 1 nov. 2009.

BAUMGARTNER, H. **What influences the outcome of valve replacement in critical aortic stenosis?** *Heart*, v. 91, n. 10, p. 1254–1256, 1 out. 2005.

BENIM, A. C.; NAHAVANDI, A.; ASSMANN, A.; SCHUBERT, D.; FEINDT, P.; SUH, S. H. **Simulation of blood flow in human aorta with emphasis on outlet boundary conditions.** *Applied Mathematical Modelling*, v. 35, n. 7, p. 3175–3188, jul. 2011.

BETTS, J. G.; DESAIX, P.; JOHNSON, E.; JOHNSON, J. E.; KOROL, O.; KRUSE, D. **Anatomy & physiology.** [s.l: s.n.].

BONOW, R. O.; CARABELLO, B. A.; CHATTERJEE, K.; DE LEON, A. C.; FAXON, D. P.; FREED, M. D.; SHANEWISE, J. S. **ACC/AHA 2006 Guidelines for the Management of Patients With Valvular Heart Disease: A Report of the American College of Cardiology/American Heart Association Task Force on Practice Guidelines (Writing Committee to Revise the 1998 Guidelines for the Management of Patients With Valvular Heart Disease): Developed in Collaboration With the Society of Cardiovascular Anesthesiologists: Endorsed by the Society for Cardiovascular Angiography and Interventions and the Society of Thoracic Surgeons.** *Circulation*, v. 114, n. 5, p. e84–e231. 2006.

BORAZJANI, I.; GE, L.; SOTIROPOULOS, F. **High-Resolution Fluid–Structure Interaction Simulations of Flow Through a Bi-Leaflet Mechanical Heart Valve in an Anatomic Aorta.** *Annals of Biomedical Engineering*, v. 38, n. 2, p. 326–344. 2010.

BOUMA, B. J.; VAN DEN BRINK, R. B. A.; VAN DER MEULEN, J. H. P.; VERHEUL, H. A.; CHERIEX, E. C.; HAMER, H. P. M.; TIJSSEN, J. G. P. **To operate or not on elderly patients with aortic stenosis: the decision and its consequences.** *Heart*, v. 82, n. 2, p. 143–148, 1999.

BÜRK, J.; BLANKE, P.; STANKOVIC, Z.; BARKER, A.; RUSSE, M.; GEIGER, J.; MARKL, M. **Evaluation of 3D blood flow patterns and wall shear stress in the normal and dilated thoracic aorta using flow-sensitive 4D CMR.** *Journal of Cardiovascular Magnetic Resonance*, v. 14, n. 1, p. 84, 2012.

CARABELLO, B. A.; PAULUS, W. J. **Aortic stenosis.** *The Lancet*, v. 373, n. 9667, p. 956–966, 2009.

CECCHI, E.; GIGLIOLI, C.; VALENTE, S.; LAZZERI, C.; GENSINI, G. F.; ABBATE, R.; MANNINI, L. **Role of hemodynamic shear stress in cardiovascular disease.** *Atherosclerosis*, v. 214, n. 2, p. 249–256. 2011.

CRIBIER, A. **Percutaneous Transcatheter Implantation of an Aortic Valve Prosthesis for Calcific Aortic Stenosis: First Human Case Description.** *Circulation*, v. 106, n. 24, p. 3006–3008. 2002.

DEWEY, T. M.; BROWN, D.; RYAN, W. H.; HERBERT, M. A.; PRINCE, S. L.; MACK, M. J. **Reliability of risk algorithms in predicting early and late operative outcomes in high-risk patients undergoing aortic valve replacement.** *The Journal of Thoracic and Cardiovascular Surgery*, v. 135, n. 1, p. 180–187. 2008.

EL-SAMANOUDY, R. T. M.; EL-BAZ, A. M. R. **Considerations of Stress Limiter for the SST Turbulence Model in Dual Throat Nozzle Predictions.** [s.d.].

FAGGIANO, E.; ANTIGA, L.; PUPPINI, G.; QUARTERONI, A.; LUCIANI, G. B.; VERGARA, C. **Helical flows and asymmetry of blood jet in dilated ascending aorta with normally functioning bicuspid valve.** *Biomechanics and Modeling in Mechanobiology*, v. 12, n. 4, p. 801–813, ago. 2013.

FEIJÓ, V. **Modelagem do fluxo sanguíneo na aorta abdominal utilizando interação fluido-estrutura.** 2007.

FEIJOO, R. A.; ZOUAIN, N. **Formulations in rates and increments for elastic-plastic analysis.** *International Journal for Numerical Methods in Engineering*, v. 26, n. 9, p. 2031–2048, 1 set. 1988.

FORSBERG, L. **Cardiac function and aortic valve intervention: echocardiographic studies of myocardial recovery in patients with severe aortic valve disease.** [s.l.: s.n.].

FRAUENFELDER, T., BOUTSIANIS, E., ALKADHI, H., MARINCEK, B., & SCHERTLER, T. **Simulation of blood flow within the abdominal aorta. Computational fluid dynamics in abdominal aortic aneurysms before and after interventions.** *Radio loge*, 47(11):1021-28. 2007.

GARCIA, R. G. **CFD simulation of flow fields associated with high speed jet impingement on deflectors.** 2007.

GOMES, B. A. de A. **Simulação IN VITRO do Fluxo Sanguíneo em Modelo Aórtico Tridimensional de Paciente Submetido a Implante Valvar Percutâneo.** Tese (Doutorado em Cardiologia) – Faculdade de Medicina, Universidade Federal do Rio de Janeiro. 2016.

GROVES, E. M.; FALAHATPISHEH, A.; SU, J. L.; KHERADVAR, A. **The Effects of Positioning of Transcatheter Aortic Valves on Fluid Dynamics of the Aortic Root.** *ASAIO Journal*, v. 60, n. 5, p. 545–552, 2014.

GUNNING, P. S.; SAIKRISHNAN, N.; MCNAMARA, L. M.; YOGANATHAN, A. P. **An In Vitro Evaluation of the Impact of Eccentric Deployment on Transcatheter Aortic Valve Hemodynamics.** *Annals of Biomedical Engineering*, v. 42, n. 6, p. 1195–1206, jun. 2014.

GUNNING, P. S.; VAUGHAN, T. J.; MCNAMARA, L. M. **Simulation of Self Expanding Transcatheter Aortic Valve in a Realistic Aortic Root: Implications of Deployment Geometry on Leaflet Deformation.** *Annals of Biomedical Engineering*, v. 42, n. 9, p. 1989–2001, set. 2014.

HA, H.; KIM, G. B.; KWEON, J.; LEE, S. J.; KIM, Y.-H.; KIM, N.; YANG, D. H. **The influence of the aortic valve angle on the hemodynamic features of the thoracic aorta.** *Scientific Reports*, v. 6, n. 1, out. 2016.

HARRIS, C.; CROCE, B.; PHAN, K. **Aortic stenosis.** *Annals of cardiothoracic surgery*, v. 4, n. 1, p. 99, 2015.

HUTCHINSON R., B., & RAITHBY D., G. **The Additive Correction Multigrid strategy.** *Numerical Heat Transfer*, 9(5):511–37. 1986

HELLSTEN, A. **Some improvements in Menter's k-omega SST turbulence model.** *American Institute of Aeronautics and Astronautics*, 15 jun. 1998. Available in: <<http://arc.aiaa.org/doi/10.2514/6.1998-2554>>

IUNG, B. **Decision-making in elderly patients with severe aortic stenosis: why are so many denied surgery?** *European Heart Journal*, v. 26, n. 24, p. 2714–2720, 25 out. 2005.

KAGADIS, G. C.; SKOURAS, E. D.; BOURANTAS, G. C.; PARASKEVA, C. A.; KATSANOS, K.; KARNABATIDIS, D.; NIKIFORIDIS, G. C. **Computational representation and hemodynamic characterization of in vivo acquired severe stenotic renal artery geometries using turbulence modeling.** *Medical Engineering & Physics*, v. 30, n. 5, p. 647–660, jun. 2008.

LEE, S. Y.; DIMENNA, R. A. **Validation Analysis for the Calculation of a Turbulent Free Jet in water Using CFDS-FLOW3D and FLUENT (U).** No. WSRC-TR-95-0170, Savannah River National Laboratory, Aiken, SC, 1995.

LEON, M. B.; SMITH, R.; MAKKAR, R. R.; BROWN, D. L.; BLOCK, P. C.; GUYTON, R. A.; DOUGLAS, P. C. **The NEW ENGLAND JOURNAL of MEDICINE.** 2010.

LIU, H.; WINOTO, S. H.; SHAH, D. A. **Velocity measurements within confined turbulent jets: Application to cardiovalvular regurgitation.** *Annals of biomedical engineering*, v. 25, n. 6, p. 939–948, 1997.

MALVINDI, P. G.; PASTA, S.; RAFFA, G. M.; LIVESEY, S. **Computational fluid dynamics of the ascending aorta before the onset of type A aortic dissection.** *European Journal of Cardio-Thoracic Surgery*, p. ezw306, 15 set. 2016.

MENTER, F. R. **Improved two-equation k-omega turbulence models for aerodynamic flows.** 1992.

MENTER, F. R. **Zonal Two Equation Kappa-Omega Turbulence Models for Aerodynamic Flows.** In: *AIAA FLUID DYNAMICS CONFERENCE*. 6-9 Jul. 1993, United States: 1 jan. 1993. Available in: <<https://ntrs.nasa.gov/search.jsp?R=19960044572>>

MENTER, F. R. **Two-equation eddy-viscosity turbulence models for engineering applications.** *AIAA Journal*, v. 32, n. 8, p. 1598–1605, ago. 1994.

NISHIMURA, R. A.; OTTO, C. M.; BONOW, R. O.; CARABELLO, B. A.; ERWIN, J. P.; FLEISHER, L. A.; THOMPSON, A. **Guideline for the Management of Patients With Valvular Heart Disease: A Report of the American College of Cardiology/American Heart Association Task Force on Clinical Practice Guidelines**. *Circulation*, v. 135, n. 25, p. e1159–e1195, 20 jun. 2017.

O'BRIEN, S. M.; SHAHIAN, D. M.; FILARDO, G.; FERRARIS, V. A.; HAAN, C. K.; RICH, J. B.; ANDERSON, R. P. **The Society of Thoracic Surgeons 2008 Cardiac Surgery Risk Models: Part 2—Isolated Valve Surgery**. *The Annals of Thoracic Surgery*, v. 88, n. 1, p. S23–S42. 2009.

PINHO, H. A. **Análise numérica do escoamento em aorta ascendente**. Rio de Janeiro, 2016. 46p. Projeto Final de Graduação - Departamento de Engenharia Mecânica, Pontifícia Universidade Católica do Rio de Janeiro.

POPE, STEPHEN B. **Turbulent Flows**. Cambridge, Cambridge University Press, 2000.

RAHIMTOOLA, S. H. **Valvular heart disease: a perspective**. *Journal of the American College of Cardiology*, v. 1, n. 1, p. 199–215. 1983.

RAHIMTOOLA, S. H. **Valvular heart disease: a perspective on the asymptomatic patient with severe valvular aortic stenosis**. *European Heart Journal*, v. 29, n. 14, p. 1783–1790. 2008.

RUMSEY, C. 2015. **Turbulence Modeling Resource**. Langley Research Center - NASA. <https://turbmodels.larc.nasa.gov/sst.html>. [Online]. Access in: July 28. 2017.

SCHUELER, R.; HAMMERSTINGL, C.; SINNING, J.-M.; NICKENIG, G.; OMRAN, H. **Prognosis of octogenarians with severe aortic valve stenosis at high risk for cardiovascular surgery**. *Heart*, v. 96, n. 22, p. 1831–1836. 2010.

SCHWARZ, F.; BAUMANN, P.; MANTHEY, J.; HOFFMANN, M.; SCHULER, G.; MEHMEL, H. C.; KÜBLER, W. **The effect of aortic valve replacement on survival**. *Circulation*, v. 66, n. 5, p. 1105–1110. 1982.

STANDRING, S.; GRAY, H. (EDS.). **Gray's anatomy: the anatomical basis of clinical practice**. 40. ed., reprinted ed. Edinburgh: Churchill Livingstone Elsevier. 2009.

SUN, Z.; CHAICHANA, T. **A systematic review of computational fluid dynamics in type B aortic dissection**. *International Journal of Cardiology*, v. 210, p. 28–31. 2016.

SUN, Z.; XU, L. **Computational fluid dynamics in coronary artery disease**. *Computerized Medical Imaging and Graphics*, v. 38, n. 8, p. 651–663. 2014.

TRAUZEDDEL, R. F.; LÖBE, U.; BARKER, A. J.; GELSINGER, C.; BUTTER, C.; MARKL, M.; VON KNOBELSDORFF-BRENKENHOFF, F. **Blood flow characteristics in the ascending aorta after TAVI compared to surgical aortic valve replacement**. *The International Journal of Cardiovascular Imaging*, v. 32, n. 3, p. 461–467. 2016.

VAQUETTE, B. **Valve replacement in patients with critical aortic stenosis and depressed left ventricular function: predictors of operative risk, left**

**ventricular function recovery, and long term outcome.** *Heart*, v. 91, n. 10, p. 1324–1329. 2005.

VERSTEEG, H.K.; MALALASEKERA, W. (2007). **An introduction to computational fluid dynamics: the finite volume method.** 2nd ed. Harlow: Prentice Hall. 2007.

WAN AB NAIM, W. N.; GANESAN, P. B.; SUN, Z.; CHEE, K. H.; HASHIM, S. A.; LIM, E. **A Perspective Review on Numerical Simulations of Hemodynamics in Aortic Dissection.** *The Scientific World Journal*, v. 2014, p. 1–12. 2014.

WANG, Y.; DONG, Q.; WANG, P. **Numerical Investigation on Fluid Flow in a 90-Degree Curved Pipe with Large Curvature Ratio.** *Mathematical Problems in Engineering*, v. 2015, p. 1–12. 2015.

WEBB, J.; CRIBIER, A. **Percutaneous transarterial aortic valve implantation: what do we know?** *European Heart Journal*, v. 32, n. 2, p. 140–147. 2011.

YOGANATHAN, A. P.; CAPE, E. G.; SUNG, H.-W.; WILLIAMS, F. P.; JIMOH, A. **Review of hydrodynamic principles for the cardiologist: applications to the study of blood flow and jets by imaging techniques.** *Journal of the American College of Cardiology*, v. 12, n. 5, p. 1344–1353. 1988.

ZHANG, Q.; GAO, B.; CHANG, Y. **The study on hemodynamic effect of series type LVAD on aortic blood flow pattern: a primary numerical study.** *BioMedical Engineering OnLine*, v. 15, n. S2. 2016.

## A1. Grid Test

To obtain a mesh independent solution a grid test was performed. To this end, three meshes with different levels of refinement ( $2 \times 10^6$ ,  $4 \times 10^6$  and  $8 \times 10^6$  nodes) were created employing the tool ANSYS Meshing. The mesh was defined employing the tetrahedron method, and it was refined near the aorta's surface, to better capture the derivatives of the flow in the boundary layer region (Fig. 3.5). A first mesh was defined and the subsequent meshes were created by dividing and multiplying the control volumes by two, imposing restrictions of maximum and minimum control volume size.

Two different inlet flow rates were employed to define the mesh. These values were selected based on the values encountered in the pulsatile cycle, during the systole period. The first flow rate was 2.6 lt/min, corresponding to the beginning of the cycle, and the second one, equal to 25 lt/min, correspond to the ending of the cycle. In each case, the convergence was analyzed employing the variation of various parameters. In both cases, the k- $\omega$  SST with low Reynolds corrections Model was employed to represent the turbulent characteristics of the flow.

The first two parameters considered to verify mesh convergence were global parameters, significantly important for the present study, which are the difference of modified pressure between the input plane and a plane displaced from 6cm from it; and the maximum value of dimensionless wall distance ( $y^+$ ) on the walls.

Table A1.1 illustrates the results obtained with both volumetric flow rates for these two variables. It can be clearly seen that, the mesh with  $4 \times 10^6$  presented results very close to those obtained with the finest mesh. It can also be observed that the maximum wall distance  $y^+$  for the coarse is slightly greater than 5, and it is smaller than 5, for the other two finer. This limit is a requirement of the k- $\omega$  SST turbulence model. Therefore, it can be said that all meshes presented the necessary refinement to capture the boundary layer near the wall, with the model selected.

The axial velocity profile along the z axis, centerline of the jet, is shown in Figure A1.1 for the three meshes and two flow rates. The y-component of the

velocity is illustrated in Figure A1.2, while the pressure profiles are shown in Figure A1.3. An excellent agreement was obtained with the two finer meshes, and a small deviation can be seen with the coarse mesh.

**Table A1.1** – Variation  $\Delta\hat{p}$  and  $y^+$ (max) for three mesh sizes and two flow rates

NUMBER OF NODES	2.6 lt/min		25 lt/min	
	$\Delta\hat{p}$	$y^+$ (max)	$\Delta\hat{p}$	$y^+$ (max)
200.000	5.23	1.07	433.46	5.87
400.000	4.48	0.89	431.29	4.45
800.000	4.47	0.89	431.12	4.43

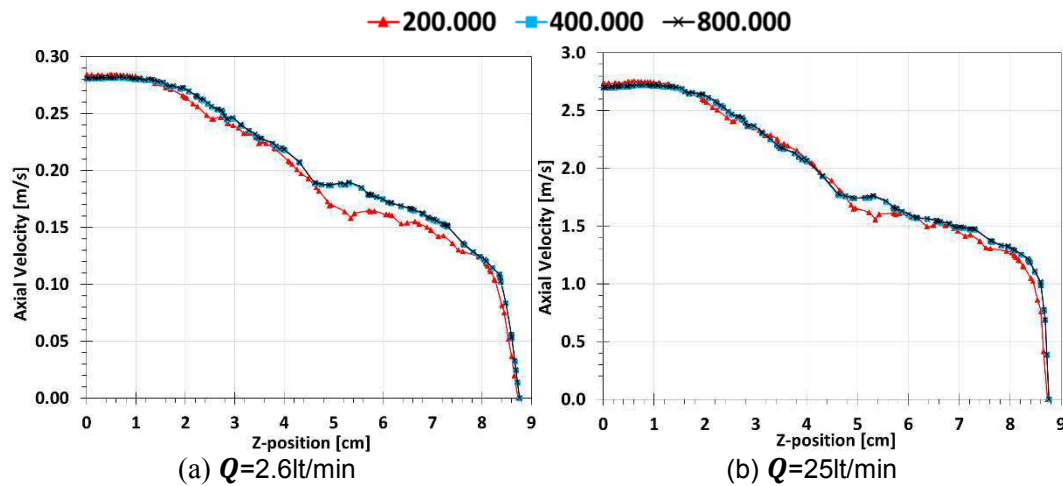


**Figure A1.1** – Grid test. Axial Velocity in the z-axis.  $Q = 2.6 \text{ lt/min}$  and  $25 \text{ lt/min}$

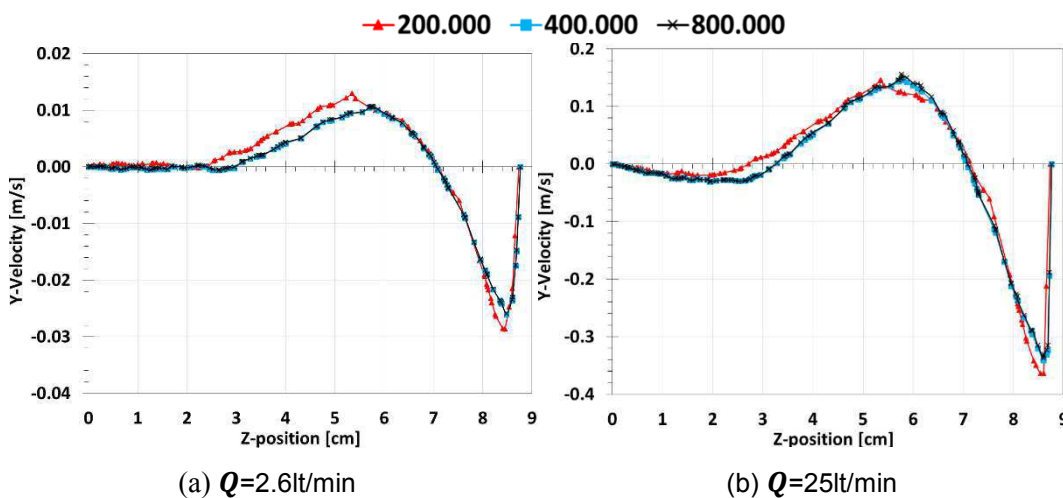
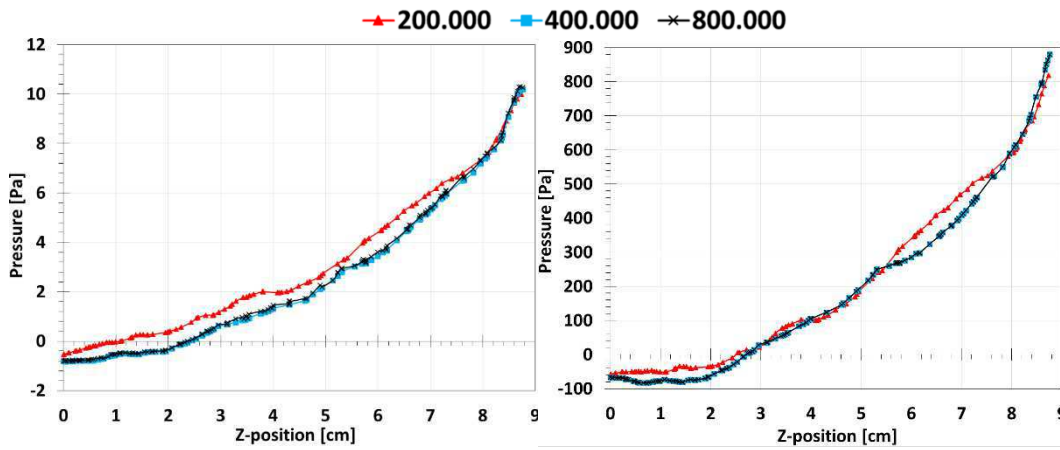


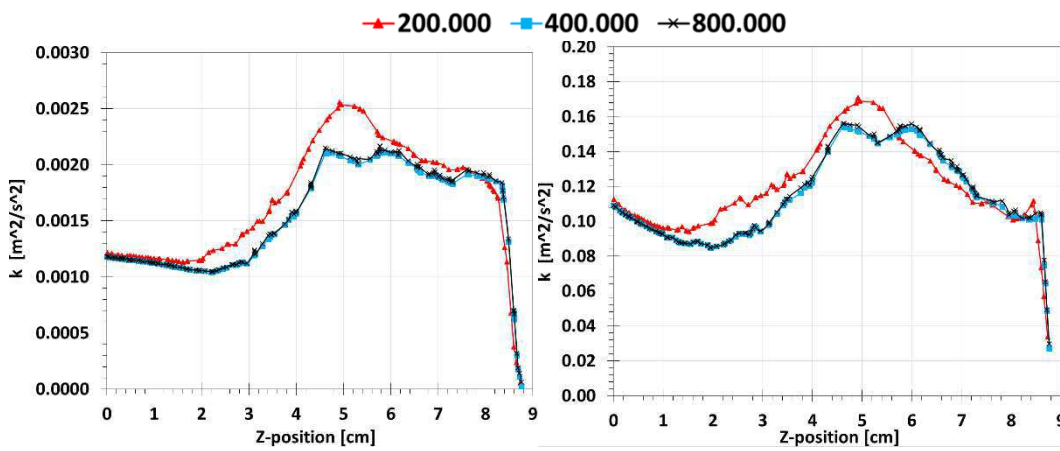
**Figure A1.2** – Grid test. Y-velocity in the z-axis.  $Q = 2.6 \text{ lt/min}$  and  $25 \text{ lt/min}$



(a)  $Q=2.6\text{lt/min}$  (b)  $Q=25\text{lt/min}$   
**Figure A1.3** – Grid test. Pressure in the z-axis.  $Q = 2.6 \text{ lt/min}$  and  $25 \text{ lt/min}$

The profiles along the z-axis for turbulent kinetic energy is presented in Figure A1.4. The dimensionless Reynolds stress ( $\overline{w'v'}$ ;  $\overline{v'v'}$  and  $\overline{w'w'}$ ) are illustrated in Figures A1.5 through Figure A1.7, respectively. In all figures, for all turbulent variables, the solutions with the finer and intermediate mesh are equivalent. In all figures, for all turbulent variables, the solutions with the finer and intermediate mesh are equivalent.

By examining all figures, it is observed that for the coarse mesh of  $200 \times 10^3$  nodes, all variables present profiles a little different from those obtained with the finer meshes. Also, the meshes of  $400 \times 10^3$  and  $800 \times 10^3$  nodes present practically the same results. Since the finer mesh requires a significant larger computing effort and does not improve the solution, the most efficient choice is the Mesh of  $400 \times 10^3$  nodes. This mesh configuration was employed in all analysis presented here.



(a)  $Q=2.6\text{lt/min}$  (b)  $Q=25\text{lt/min}$

**Figure A1.4** – Grid test. Turbulent kinetic energy in the z-axis.

$Q = 2.6 \text{ lt/min}$  and  $25 \text{ lt/min}$

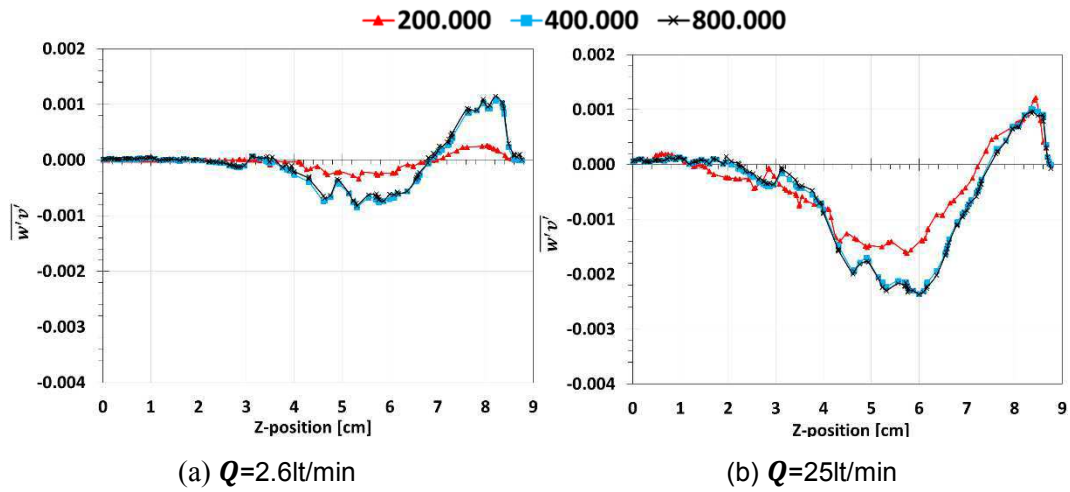


Figure A1.5 – Grid test  $\overline{w'v'}$  in the z-axis.  $Q = 2.6 \text{ lt/min}$  and  $25 \text{ lt/min}$

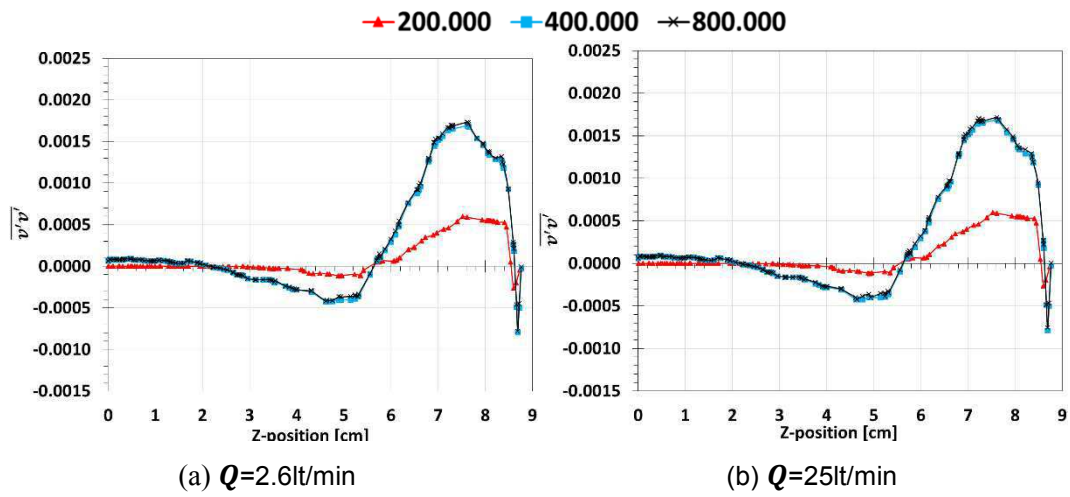


Figure A1.6 – Grid test  $\overline{v'v'}$  in the z-axis.  $Q = 2.6 \text{ lt/min}$  and  $25 \text{ lt/min}$

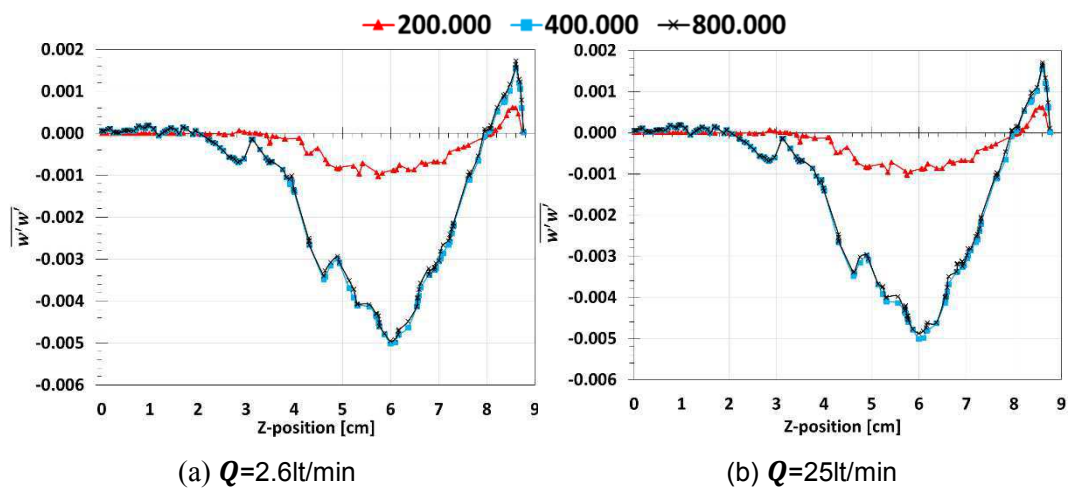


Figure A1.7 – Grid test  $\overline{w'w'}$  in the z-axis.  $Q = 2.6 \text{ lt/min}$  and  $25 \text{ lt/min}$

## A2 Comparison of Turbulence Models

Turbulence models are not universal, and present several empirical constants. Therefore, the right choice of a turbulent model is always a great challenge. Thus, the impact of five different turbulence models in the flow field was examined. To perform the present test, the inlet volumetric flow rate of 5.3 lt/min was defined with 10% of turbulence intensity. The characteristic inlet dimension was maintain constant for cases.

The turbulence models selected to be examined were:

- Standard  $\kappa$ - $\omega$  SST model
- Low Reynolds  $\kappa$ - $\omega$  SST model
- Standard  $\kappa$ - $\epsilon$  realizable model
- $\kappa$ - $\epsilon$  realizable model, with non-equilibrium law at the walls
- $\kappa$ - $\epsilon$  realizable model, with enhanced wall treatment.

Figure A2.1 illustrates the isocontours of the axial velocity at the central plane (coincident with the origin of the coordinate system, at the center of the inlet jet, passing by the right coronary) obtained with all turbulence models. Both SST  $\kappa$ - $\omega$  models present very similar fields, with no significant difference between the velocity contours. However, the velocity field predicted by the model  $\kappa$ - $\epsilon$  realizable with enhanced wall treatment is far from the expected for a free jet, therefore it should be discarded. The  $\kappa$ - $\epsilon$  standard and non-equilibrium wall cases presented an acceptable configuration, although a certain inclination towards the posterior wall of the aorta is noticeable, which should not occur.

Figure A2.2 presents a comparison of the five turbulent models, for the modified pressure  $\hat{p}$ , Eq. (3.9), which is the driving force for the flow. Examining Figure A2.2, it is also remarkable that the values obtained with the  $\kappa$ - $\epsilon$  realizable with enhanced wall treatment were far from the average values of the other four cases. Again, the values obtained with  $k$ - $\omega$  with and without Low Reynolds corrections were similar to each other. The  $\kappa$ - $\epsilon$  standard case presented a higher pressure increase as the jet advances, than the  $\kappa$ - $\omega$  cases. This increase in pressure is even higher in the case of non-equilibrium wall.

However, qualitative results were obtained for all cases, i.e, the level of modified pressure increase at the center of the region is equivalent, and the region with higher pressures is also the same. Greater differences are observed with the  $\kappa-\epsilon$  with non-equilibrium wall.

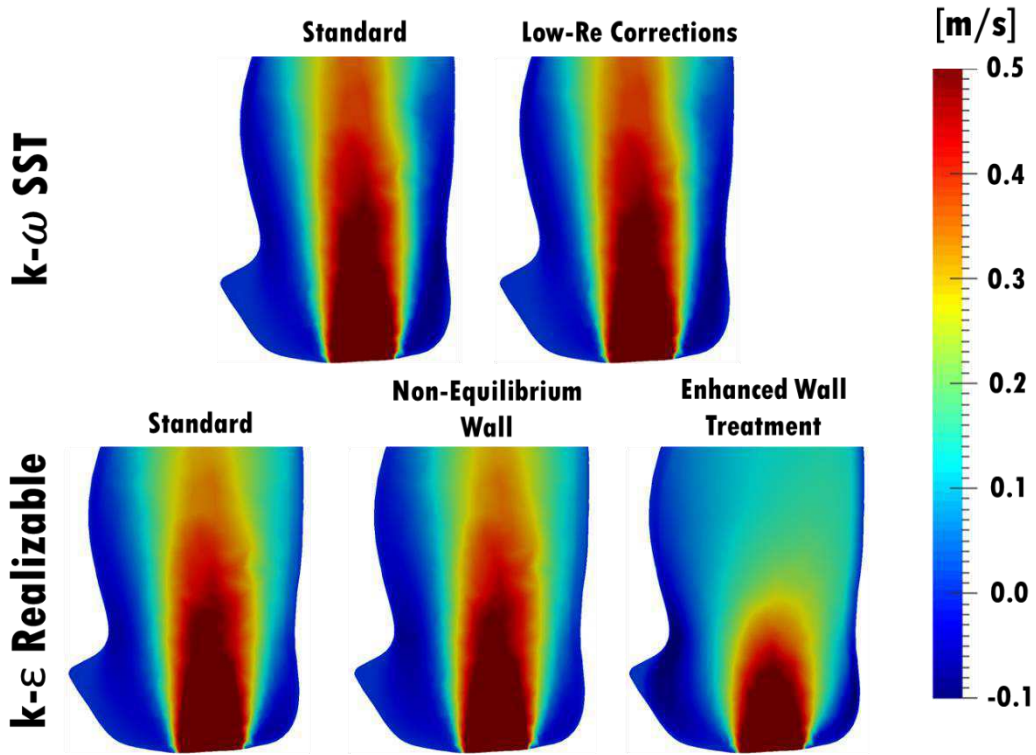


Figure A2.1 - Comparison of turbulence models (Axial Velocity)

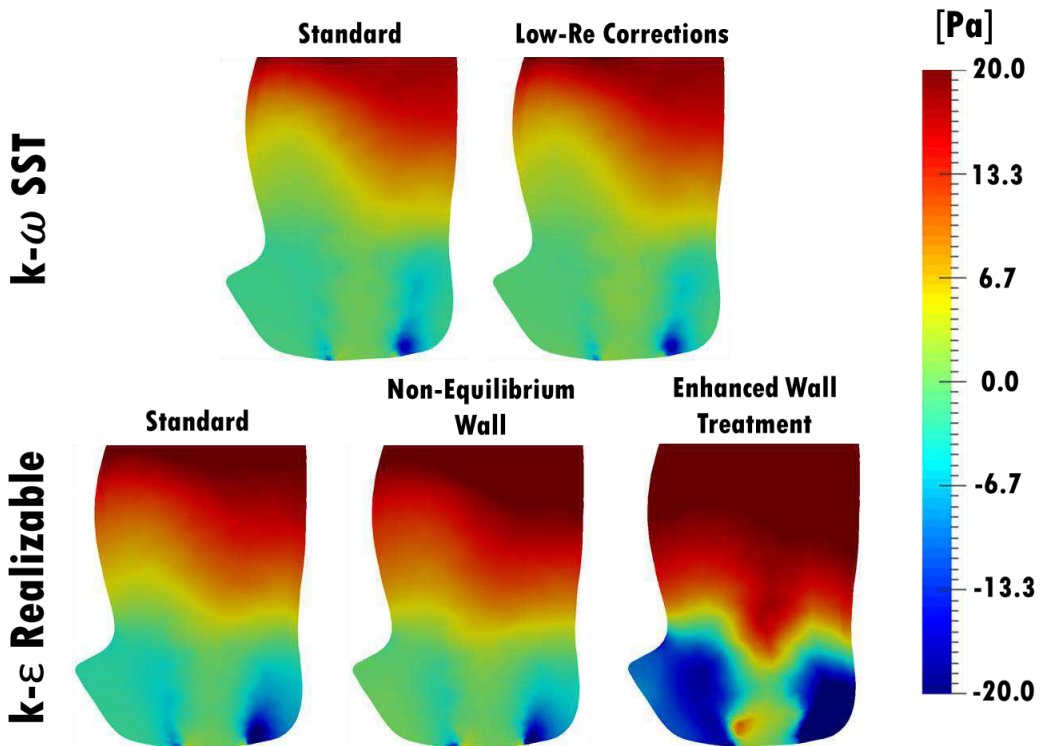
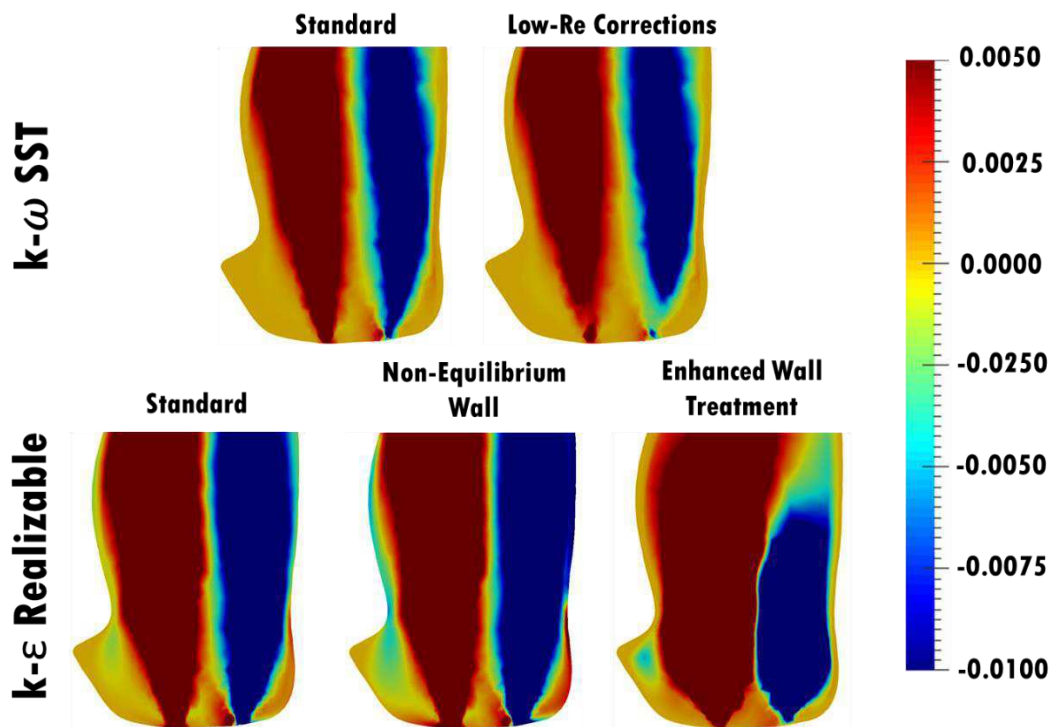


Figure A2.2 - Comparison of turbulence models (Pressure)

The next comparison was performed by analyzing the iso-contour of the dimensionless shear Reynolds tensor  $\tau_t^* = -\overline{v'w'}/w_{in}^2$  in Figure A2.3. It can be seen that variants of the  $\kappa$ - $\varepsilon$  model predicts very high turbulent shear Reynolds stress at the aortic walls, when this values should go to zero. The  $\kappa$ - $\omega$  models yielded equivalent results and showed a good response on the walls and in the inner layers, i.e., with opposite sign in each side of the main inlet jet, indicating a tendency of a spread of the jet.

Figure A2.4 presents the contours of the wall shear stress at the surface of the aorta, obtained with the five turbulence models. Analyzing Figure A2.4, once again, similar results were obtained with both  $\kappa$ - $\omega$  models, and the differences between the  $\kappa$ - $\omega$  and  $\kappa$ - $\varepsilon$  models are more evident. The  $\kappa$ - $\varepsilon$  non-equilibrium wall presents very high shear stresses, while the non-equilibrium case shows the opposite. Similar results were obtained with the standard case.



**Figure A2.3** - Comparison of turbulence models (Dimensionless Reynolds Stress).

The main reason for the differences in the results obtained with the SST  $\kappa$ - $\omega$  and  $\kappa$ - $\varepsilon$  realizable is due to the treatment of the wall region. It is well known that the  $\kappa$ - $\varepsilon$  model is not adequate at the wall region especially for low Reynolds number (as in the present study). Even with more sophisticated wall treatment, this region was not adequately modelled. Therefore, the  $\kappa$ - $\omega$  SST, which combined the  $\kappa$ - $\varepsilon$  for the region away from

the wall, with the  $\kappa\text{-}\omega$  at the wall region is more adequate. Further, although there were not significant differences between the results of the standard SST  $\kappa\text{-}\omega$  and with low Reynolds version, the latter was selected, since the present Reynolds range of interest is quite low.

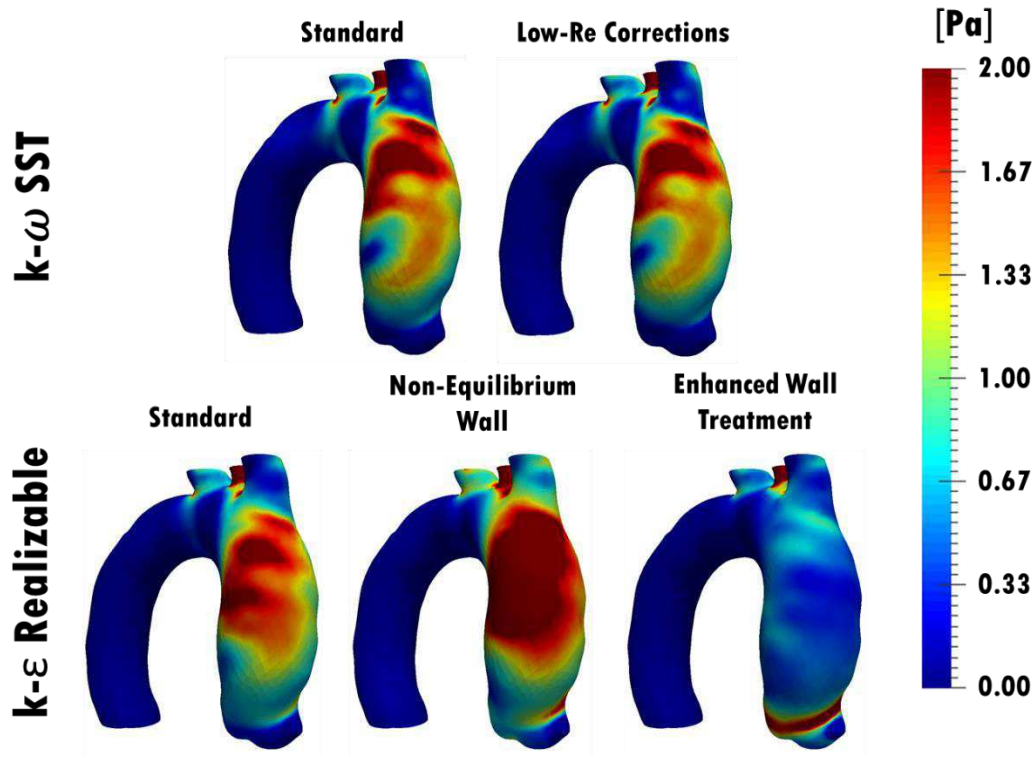


**Figure A2.4** - Comparison of turbulence models (WSS)

An important parameter to be examined is the dimensionless wall distance ( $y^+ = u^* y/\nu$ ), being  $u^* \equiv \sqrt{\tau_{\omega wall}/\rho}$ , and  $y$  is the distance from the first inner node to the wall. For the  $\kappa\text{-}\omega$  models, the mesh should be defined with this value inferior to 5. The maximum values for all the turbulence models are represented in Table A2.1, for all cases,  $y^+$  varied between 1 and 2. Usually  $\kappa\text{-}\epsilon$  models require larger values of  $y^+$ , since this family is more appropriated for very high Reynolds number. The special wall treatment of the  $\kappa\text{-}\epsilon$  models was aimed to improve the predictions, without coarsening the mesh, which is undesirable.

The results shown indicate that  $\kappa\text{-}\omega$  models are more adequate to solve this type of flow problem. Between the two variants of  $\kappa\text{-}\omega$  SST, the one with low Reynolds number was selected, since its flow distributions were reasonable, i.e., qualitatively as expected. Further, it presented a faster convergence rate. Therefore, it was the model selected to be employed in the present work.

**Table A2.1** - Variation of  $y^+$ (max) for the five turbulence models

TURBULENCE MODEL	$y^+$ (max)
k- $\omega$ SST Standard	1.61
k- $\omega$ SST with Low-Re corrections	1.58
k- $\epsilon$ Realizable Standard	1.62
k- $\epsilon$ Realizable Non-equilibrium wall	1.82
k- $\epsilon$ Realizable Enhanced Wall Treatment	1.09